Ludwig-Maximilians-Universität

Sigillum Universitatis Ludovici Maximiliani

MHD numerical simulations in a cosmological context

Dissertation der Fakultät für Physik

Dissertation of the Faculty of Physics

der Ludwig-Maximilians-Universität München

at the Ludwig Maximilian University of Munich

für den Grad des

for the degree of

Doctor rerum naturalium

vorgelegt von Federico Andrés Stasyszyn

presented by

aus Córdoba, Argentina

from

München, 15.03.2011

Sigillum Universitatis Ludovici Maximiliani

1. Gutachter: Prof. Dr. Simon D. M. White

REFEREE:

2. Gutachter: Prof. Dr. Harald Lesch

REFEREE:

Tag der mündlichen Prüfung: 27.05.2011

DATE OF THE ORAL EXAM:

Contents

List of Figures

Zusammenfassung

Magnetfelder sind in fast überall im beobachtbaren Universums zu finden. Ihre Präsenz im intergalaktischen Medium und innerhalb von Galaxienhaufen (intra-cluster medium, ICM) wurde durch Beobachtungen von diffuser Radioemission und Faraday-Rotation polarisierten Lichts von Radio-Quellen, die innerhalb oder hinter dem magnetisierten Medium liegen, bestätigt. Trotz dieser Beobachtungen ist die dynamische Bedeutung von Magnetfeldern in astrophysikalischen Systemen nach wie vor nicht verstanden, und es gibt viele Prozesse bei denen der Einfluss von Magnetfeldern weitere Untersuchungen benötigt. Astrophysikalische Systeme sind komplex und in hohem Maße nichtlinear, weswegen numerische Simulationen eine gute Möglichkeit darstellen um diese Systeme zu studieren. Die Berücksichtigung von Magnetfeldern in solchen Simulationen ist jedoch nicht einfach, da es oft nicht trivial ist die Bedingung $\nabla \cdot \mathbf{B} = 0$ und die Stabilität des Verfahrens in verschiedenen Anwendungen zu gewährleisten.

Während meiner Doktorarbeit habe ich die MHD Implementierung innerhalb des N-body/SPH Programms GADGET betrachtet und weiterentwickelt. Ich habe verschiedene Methoden zur Regulierung des Magnetfeldes und zur Vermeidung von Instabilitäten untersucht. Diese Methoden beinhalten die Verwendung von *Euler* Potentialen zur Beschreibung des Magnetfeldes als auch Verfahren zur Verminderung des numerischen $\nabla \cdot \mathbf{B}$ Fehlers. Mit Hilfe des GADGET Programms habe ich die Entwicklung des Magnetfeldes während der kosmologischen Entstehung von Galaxienhaufen untersucht. Der Vergleich zwischen den verschiedenen numerischen Methoden zeigt, dass die numerischen $\nabla \cdot \mathbf{B}$ Fehler nicht zu einer unphysikalischen Verstärkung des Magnetfeldes führen.

Der Vergleich synthetischer Karten der Faraday-Rotation-Verteilung unserer simulierten Galaxienhaufen mit Beobachtungen zeigt, dass die relevante Physik nur durch ein Turbulenzmodell beschrieben werden kann, das viele Längenskalen abdeckt. Das bedeutet, dass der vom kosmologischen Entstehungsprozess getriebene turbulente Dynamo effizient arbeitet. Dabei werden die grundlegenden Beobachtungsmerkmale als auch Details wie Struktur-Funktionen (die bei steigender Auflösung gegen die Beobachtungen konvergieren) gut wiedergegeben. Damit wird deutlich, dass moderne numerische Verfahren zusammen mit einer hohen Auflösung sehr gut dafür geeignet sind, die Eigenschaften des ICM zu studieren.

Darüber hinaus habe ich den Zusammenhang zwischen der großräumigen kosmologischen Struktur und dem Magnetfeld untersucht. Im Allgemeinen ist das beobachtete Rotations-Signal von dichten Regionen (d.h. Galaxienhaufen und -gruppen) dominiert, weshalb es unklar bleibt, wie sich das Magnetfeld in weniger dichten Bereichen des Universums verhält. Deshalb müssen statistische Methoden wie Korrelationsfunktionen verwendet werden. Auf diese Weise habe ich mit Hilfe kosmologischer Simulationen die möglichen Beobachtungsfehler untersucht. Es zeigt sich, dass die Form der Korrelationsfunktion bei Verwendung eines normalisieren Schätzwertes der Rotation die zugrundeliegende Verteilung des Magnetfeldes innerhalb der kosmischen Struktur gut wiederspiegelt. Derzeitige Beobachtungsfehler unterdrücken das Rotationssignal jedoch in einer Art, die es leider unmöglich macht, die Amplitude der Korrelationsfunktion mit der Magnetisierung der großräumigen Struktur in Zusammenhang zu bringen (Stasyszyn et al., 2010).

Abstract

Magnetic fields in the Universe are found in almost all studied environments. In particular, their presence in the inter-galactic medium and in the intra-cluster medium is confirmed by diffuse radio emission as well as by observations of Faraday Rotation Measures towards polarized radio sources within or behind the magnetized medium.

Besides the observations, their dynamical importance in astrophysical systems is poorly constrained, therefore there are still plenty of processes in which the role of magnetic fields are not fully understood.

Astrophysical systems are complex and highly nonlinear. Therefore, numerical simulations have demonstrated to be a useful tool to study those problems. However, the inclusion of magnetic fields in numerical implementations is not easy to achieve. Mainly because of the difficulties to keep the $\nabla \cdot \mathbf{B}$ constraint low, and to have a stable implementation in different circumstances.

We study and developed a cosmological MHD code in SPH. We study different possible schemes to regularize the magnetic field, and avoid instabilities. Those schemes included the use of *Euler* potentials to build the magnetic field, as well as cleaning schemes for the numerical $\nabla \cdot \mathbf{B}$ errors.

We studied the magnetic field evolution in the context of cosmological structure formation of galaxy clusters. We compare different numerical schemes leading us to the conclusion that the $\nabla \cdot \mathbf{B}$ terms do not drive the evolution and growth of the magnetic field in galaxy clusters. We made synthetic rotation measure maps and study the reversals of the magnetic field in comparison with observations. The comparison between observations and high resolution simulations, suggests that the physics may be described by a multi scale turbulence model. This means that the turbulent dynamo driven by the cosmological cluster formation process works effectively, reproducing basic properties from observations, even to details shown in structure functions and converging to the observation when we increase the resolution. We clearly demonstrates that using advanced schemes together with very high resolution allow to probe the properties of the ICM.

Additionally, we investigate the magnetic fields and their relation with the cosmic structure in which they are embedded. In general, the observed rotation measure signal is strongly dominated by denser regions (e.g. those populated by galaxy clusters and groups), and in unclear how is their transition to low density regions, because there is difficult to acquire direct magnetic field information of those regions.

Therefore statistical tools, such as correlation functions have to be used. To do so, we use cosmological simulations and try to mimic all the possible observation biases to constrain actual measurements. We find that the shape of the cross-correlation function using a normalized estimator (in absence of any noise or foreground signal) nicely reflects the underlying distribution of magnetic field within the large scale structure.

However, current measurement errors suppress the signal in such a way that it is impossible to relate the amplitude of the cross-correlation function to the underlying magnetization of the large scale structure (Stasyszyn et al., 2010).

Part I

Introduction

Chapter 1

Astrophysics and Magnetic Fields

Truth is always strange, stranger than fiction.

Lord Byron (1788-1824)

Since early in history, humans were attracted to magnetic fields due to their 'magical' nature. Aristotle was the first who scientifically approached magnetism in a discussion with Thales around 625 BC in Greece.

"The lodestone makes iron come or it attracts it" is one of the earliest references of magnetism in literature is in a book from the 4th century BC, titled *Book of The Devil Valley Master*. 14 centuries later, the Chinese scientist Shen Kuo (1031-1095) described the concept of magnetic needle and how it can improve the navigation accuracy. By the XII century the Chinese were known to have huge exploration and merchant fleets using the lodestone compass to orientate.

In 1187, Alexander Neckham was the first in Europe to describe the compass and its use for navigation. Later on, in 1269, Peter Peregrinus De Maricourt wrote the *Epistola de magnete*, the first extant treatise describing the properties of magnets. The properties of magnets and the dry compass were discussed by Al-Ashraf, a Yemeni physicist, astronomer and geographer, in 1282.

In 1600, William Gilbert published *De Magnete, Magneticisque Corporibus, et de Magno Magnete Tellure* (On the Magnet and Magnetic Bodies, and on the Great Magnet the Earth), in which he describes many of his experiments with an earth model called *the terrella*. From his experiments, he concluded that the Earth is magnetic itself and that this is the reason compasses point north (previously, some believed that it was the pole star, Polaris, or a large magnetic island on the north pole that attracted the compass).

The discovery of the relationship between electricity and magnetism began in 1819 with work by Hans Christian Oersted, professor at the University of Copenhagen, when by accident he observed that an electric current could influence a compass needle (nowadays this is called Oersted's experiment). After that, scientists from that epoch put effort in discovering new properties from these interactions. In 1865, James Clerk Maxwell was able to compile all the phenomenological insights found to the epoch, into the so-called Maxwell's equations, unifying electricity, magnetism and optics in the theory of electromagnetism. He compiled a set of 14 integral equations, which are not easy to use. Oliver Heaviside, 20 years later, re-formulated these equations in the vectorial form and using partial derivatives, and which we nowadays use. In 1905, Albert Einstein used these

laws of electromagnetism in motivating his theory of special relativity, requiring that the laws held true in all inertial reference frames.

While humankind was discovering this 'new' phenomena, in nature several living beings already made use of it. Animals like sharks and rays are able to feel the field lines propagating in salty water by indirectly feeling the field's force using particular receptors. Birds are also known to sense magnetic fields, it helps them to orient themselves in their seasonal trips. Another example is the *Chiton*, a primitive marine mollusc, that has teeth coated with magnetite. It is believed that this aids them in their homing behaviour, perceiving magnetic fields for orientation. In other biological kingdoms, some bacteria are capable of synthesizing magnetite and using it to find out at which level from the surface of the water they are, as to stay at the correct depth where there is less oxygen, allowing them to survive easily. Also there are plenty of insects and other species which have tracers for magnetite and it is believed that they use them for orientation. However, it is still unclear how these senses work in the majority of the cases.

The understanding of the role of magnetic fields in nature contrasts with the open enigma that remains regarding magnetic fields in astrophysics. The way magnetic fields sustain or generate themselves in astrophysics is an open issue. As an example, most theories explaining Earth magnetic field agree that it should be imprinted from the proto-planetary stages of the solar system, but how it survived afterwards given the proper timescales of this system is still unknown. Additionally, the primordial magnetic field in the proto-planetary disc is linked to the star formation process that created the Sun, which supports the existence of magnetic field in such processes and scales. We have good measurements of the magnetic field on earth, in laboratories and even from the Sun. In general we rely on indirect methods to infer them (see section 1.2), this makes it difficult to observe them in large scales. Besides the observations, their dynamical importance for many astrophysical systems is poorly constrained, therefore there are still plenty of processes in which the role of magnetic fields are not fully understood.

In the next sections we will first describe briefly the astrophysical background of the objects that we plan to study. Then, how galactic and extragalactic magnetic fields can be estimated and briefly summarize how they are embedded in those objects and on the largest scales of the Universe. We will also spent some time on numerical simulations that have shown to be useful to study this astrophysical problems. Finally, we summarize the discussion on magnetic fields which we address in more detail within the next chapters. For a detailed discussion on extra-galactic magnetic field, dynamo effects and observations we refer the reader to Kronberg (1994), Beck et al. (1996), Moss and Shukurov (1996) and Widrow (2002). A detailed review on numerical simulations and clusters within a cosmological context can be found in Borgani and Kravtsov (2009).

1.1 Extragalactic physics basics

The most common state of ordinary matter in the Universe is plasma, i.e. atoms are separated and free protons, electrons and other particles fill the space. Outer space is the best vacuum environment that we are aware of, it is filled with approximately one *Hydrogen* atom per cubic meter on cosmological scales, and about 5 particles per cubic meter in Earth neighborhood. Therefore, in general astrophysical plasmas in the Universe can be characterized as dilute plasmas, except to the small fraction present inside stars

and other compact objects. There is no net charge of these plasma and charges can move almost freely, justifying an "Ideal" treatment of the Magnetohydrodynamical regime (see appendix A where we derive the corresponding equations). Hence, electric fields are negligible and matter and magnetic fields are strongly coupled.

A consequence from the laws of Magnetohydrodynamics (see appendix A) is that magnetic fields need a source of any kind to sustain themselves. Space is permeated with magnetic fields, and is electrically neutral given the high conductivity of the plasma, not allowing to have large dynamos from electric currents.

The way magnetic fields evolve in time, coupled with the dynamics of baryons, growing or vanishing (never completely) in some regions is an open issue. It is unclear whether complex mechanisms are needed, such as galactic dynamos, super-nova explosions, or just a gentle baryon flow to recover the magnetic flux to the measured values (see section 1.2).

Magnetic fields are tightly coupled with baryons, and thus to the structures that build the Universe. But, how those structures assembled? The current knowledge in cosmology is based on the so-called standard cosmological model. In this scenario, soon after the "big bang", the main constituents of the Universe were radiation and matter that, during the early stages, were in thermodynamical equilibrium yielding to emission of energy with black-body spectrum that we still observe today [1]. The presence of density and energy disomogeneities capable of growing under gravitational instabilities is fundamental for the structure formation process. Nowadays the presence of primordial fluctuations of the order of 10^{-5} the mean density is well established from the CMB experiment. In more quantitative terms, one can define a density contrast $\delta(\mathbf{x}, t)$, as a function of the cosmic time and spatial position

$$\delta(\mathbf{x}, t) \equiv \frac{\rho(\mathbf{x}, t) - \rho_b(t)}{\rho_b(t)}, \tag{1.1}$$

being $\rho(\mathbf{x}, t)$ the density at point $\mathbf{x}$ and instant t and $\rho_b(t)$ the background mean density as function of time. Probably these fluctuation originated in the very early phases of the Universe undergoing an exponential expansion ("inflation"), becoming the actual seeds of structure formation. When these small over-densities are present, they can grow only if the gravitational forces are stronger than the pressure or dispersion forces.

A simple linear evolution would predict present-day structures with density contrasts $\delta \sim 10^{-2}$ (Peebles, 1980). Nevertheless, we observe over-densities (i.e. galaxies) with $\delta \gg 1$, meaning that their evolution must have been strongly nonlinear. Additionally, once structure growth proceeds and enters an advanced stage, the different accretion process and histories particular of each halo make the whole picture more complex, even possibly implying that baryons physics can modify the pure gravitational interaction (Pedrosa et al., 2010).

Most of those structures reached an equilibrium between gravitational energy and other energies (i.e. kinetic, thermal) stopping their collapse, when objects reach that point in the evolution are called "viralized". However, even if they are in a dynamical equilibrium inside , they still are prompt to interact with surrounding objects. Given their sizes and the age of the Universe, galaxy clusters are young objects, therefore we can find some of them not virialized yet, as well as structures at scales beyond them.

Still, galaxy clusters are the largest bound structures of which we are aware. Theses

[1] Actually this is the best measurement from black body spectrum at the present-day, it is known as cosmic microwave background (CMB), with an effective temperature of about 2.725 °K.

structures are one of the busiest places in the Universe. Their formation process leads to an accretion of a huge amount of matter, which heats up the plasma to levels where *X-ray* emission occurs. The intra-cluster medium has typically temperatures of $T \simeq 10^7 - 10^8$ °K and a typical particle number density of $10^5 - 10^2$ m^{-3}, compared with the $T \simeq 10^5 - 10^7$ °K and $10 - 100$ m^{-3} in the solar neighborhood. The ICM is characterized by an emission of about 10^{43}–10^{45} erg s^{-1} The main contributions to this emission are the free-free interactions of electrons and ions and emission lines by ions of heavy elements (i.e. iron). From *X-ray* observations we can trace the hot plasma while from radio emission and Faraday rotation measurements reveal the presence of magnetic fields (see section 1.2). The cross information from the different observation methods in galaxy clusters make them ideal laboratories to test theories of the origin and evolution of extragalactic magnetic fields.

Dynamical constrains from measurements of the velocities of galaxies in clusters have provided the first determination of the mass involved in such structures, which typically falls in the range[2] 10^{14}–$10^{15} M_\odot$. Baryons constitute only a small fraction of this mass, however galaxy clusters are charaterize to have almost the same baryon fraction of the Universe independent of their total mass (Gonzalez et al., 2007). Rich clusters appear to be in hydrostatic equilibrium with velocities ~ 1000 km s^{-1} (see, for example, Sarazin, 1986). In those cases, the temperature of the ICM is consistent with velocities of galaxies and indicates that both galaxies and gas are in equilibrium within a common gravitational potential well. The mass inferred from the galaxies and ICM are not sufficient to explain the depth of the gravitational potential well, which implies that most of the mass in clusters is in a form of dark matter.

Fig. (1.1) shows an overlay of the optical and *X-ray* images of the massive cluster Abell 1689. We can recognize the main components of the clusters of galaxies: stars in galaxies, the hot ICM via its *X-ray* emission, and the presence of the unseen dark matter through the distorted shapes of background galaxies because of gravitational lensing effects. Bright elliptical galaxies are typically located at the cluster center. Such central galaxies show little evidence of ongoing star formation, despite their extremely large masses and being in the center of a crowded environment.

Form the mass range of galaxy clusters, we can infer that they are the result of the collapse of primordial density fluctuations of comoving scales of the order of $\sim$ 10Mpc. On scales roughly above 10Mpc, the main acting force is gravity and therefore is the main driver of the evolution of the structure. These scales can be studied analytically, and tested by cosmological N-body simulations. We can follow the evolution and growth, due to gravitational instabilities, of the fluctuations that we seed in the denisty field as initial conditions defined at an early epoch of the Universe.

Since gravity is a force scale-free, we can try to build up a galaxy cluster model being *self-similar*, meaning that clusters of different mass are scaled versions of each other, and their mass is the only parameter that determines their properties(see Kaiser, 1986, for a review on this model).

To define such model we take into account the cosmic evolution, defining M_{δ_c} as the mass contained within the radius r_{δ_c} at redshift z, enclosing a mean over-density δ_c, similar as defined in Eq. (1.1). Then M_{δ_c} is proportional to $\rho_c(z)\delta_c r_{\delta_c}^3$ [3]. The critical density of

[2] $M_\odot \approx 1.99 \times 10^{33}$g is the mass of the Sun.

[3] Note that $\rho_c(z)$ is the critical density of the Universe defined by the *Friedmann* equations which governs the expansion of the Universe. $\rho_c(z) = 3\ H(z)/8\ G\ \pi$

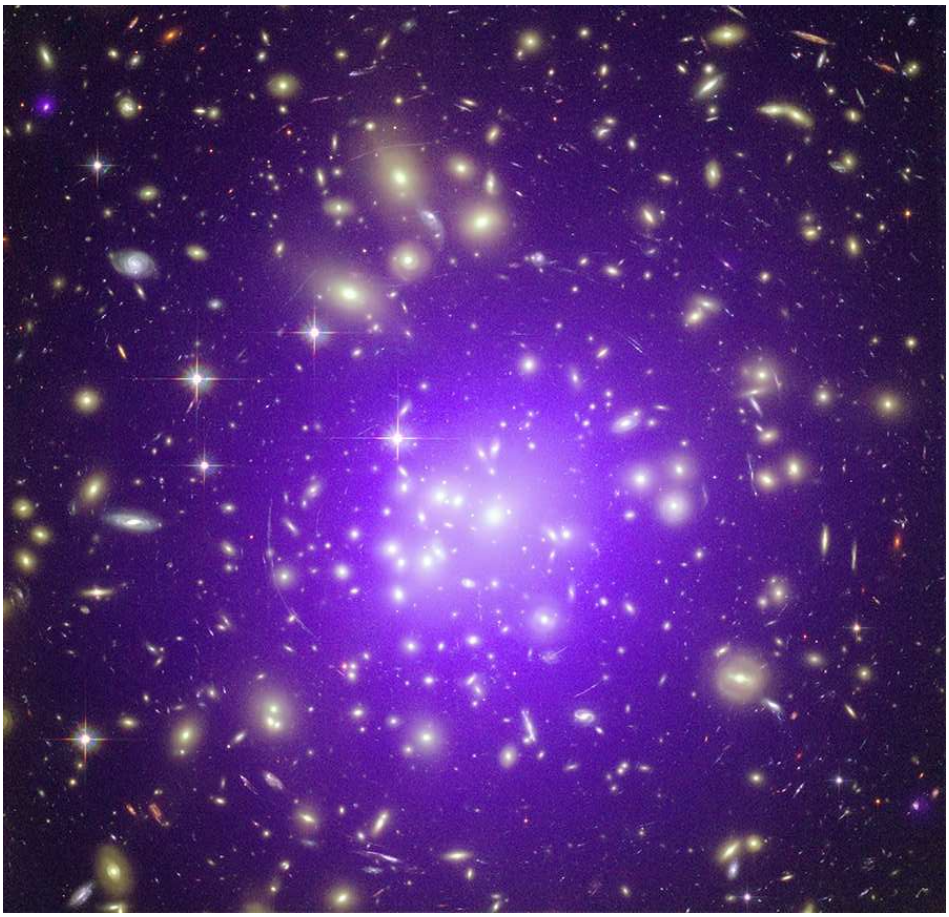

Figure 1.1: Composite X–ray/optical image of the galaxy cluster Abell 1689, located at redshift $z = 0.18$. The map shows an area of 556 Kpc on a side. The purple diffuse halo shows the distribution of gas at a temperature of about 10^8 °K, as revealed by the Chandra X-ray Observatory. Images of galaxies in the optical band, colored in yellow, are from observations performed with the Hubble Space Telescope. (Credits:X-ray: NASA/CXC/MIT; Optical: NASA/STScI; Composite:Borgani and Kravtsov (2009)).

the universe scales with redshift as $\rho_c(z) = \rho_{c0}E^2(z)$, where

$$E(z) \;=\; H(z)/H_0 \;=\; \left[(1+z)^3\Omega_m + (1+z)^2\Omega_k + \Omega_\Lambda\right]^{1/2} \tag{1.2}$$

gives the evolution of the Hubble parameter $H(z)$, taking into account the expansion of the Universe. $\Omega_k = 1 - \Omega_m - \Omega_\Lambda$ is the contribution from curvature of the Universe, Ω_m is the baryon density ratio needed to stop the expansion of the Universe only by matter and Ω_Λ is the so called cosmological constant that interacts as a repulsive force in the expantion. Therefore, the cluster size r_{δ_c} is only function of time by z and mass by M_{δ_c}.

If we assume that the gas heated during the infall is in equilibrium within the gravitational potential Φ of the cluster, the temperature should follow $k_BT \propto \Phi \propto M_{\delta_c}/r_{\delta_c}$. Therefore the above relation between radius and mass can be linked to the temperature

$$M_{\delta_c} \propto T^{3/2}E^{-1}(z) \tag{1.3}$$

This relation between mass and temperature can be used as a scaling relation when analyzing observations.

The *X-ray* luminosity, as an example, scales with the effective emissivity times the volume that is emitting inside the cluster. Therefore, assuming a thermal bremsstrahlung process (see section 1.2) dominating the emission of a given electron number density n_e (e.g., Peterson and Fabian, 2006), we have $L_X \propto n_e^2 T^{1/2} r_{\delta_c}^3$. Then, n_e scales as $\propto M/r_{\delta_c}^3 = \text{const}$ and $T \propto M_{\delta_c}/r_{\delta_c}$, which (using the $M - T$ relation Eq. (1.3) above) gives $L_X \propto T^2 E(z)$.

At small scales (i.e. $<$ 1 Mpc), baryon physics begin to play an important role besides gravity. The structure formation via sequencial mergers and accretion of smaller systems, implies that the intergalactic gas is heated and disturbed by compression and shocks. Once this gas cools and is dense enough, it can be transformed into stars or accreted onto super massive black holes inside the cluster galaxies. The process as a whole implies different baryon physics as cooling, star formation and super massive black holes activity, which produces an energetic feedback, injecting and mixing the baryons throughout the cluster. The complex star formation process, includes the generation and spread of heavy elements by the end of the life cycle of stars, in super nova events.

As an example of the intriguing physics happening in cluster cores, we should mention that some of them show an *X-ray* emission extremely high. This emission should finish when the system reaches a thermal equilibrium. However, this cooling time is shorter than the dynamical time of the system (by size, mass, etc.). Additionally, when the cool gas is compressed, flow towards the center, following the gravitational force and the pressure from the surrounding hot environment (Fabian et al., 1984). These "cooling flows" are also found elliptical galaxies and groups of galaxies. In particular in some galaxy clusters a sharp peak in the *X-ray* surface brightness distribution is observed, implying the density rise towards the cluster center, therefore confirming the presence of cooling events (see, Fabian, 1994).

Accretion flows and the motions of groups and galaxies, which perturb their medium by gravitational and hydrodynamical interactions, can generate substantial stochastic motions in the ICM. Those phenomena are substantially more important than gravity in the central regions of the clusters, breaking the *self–similarity* in these regions and interacting with the "cool flow" event. Energy of the large-scale turbulent eddies can cascade down to smaller scales resulting in power law turbulent energy and velocity spectra. In fact, numerical simulations of cluster formation generally show that subsonic random flows are ubiquitous even in apparently relaxed clusters This turbulence can have several important effects on the ICM. It can facilitate mixing of gas at different radii and correspondingly exchange of thermal energy, diffusion of heavy elements which would tend to broaden the centrally peaked abundance profile (Rebusco et al., 2005). Turbulence is also believed to maintain and amplify cluster magnetic fields via dynamo processes (Subramanian et al., 2006), and to contribute to the acceleration of cosmic-rays [4] in the ICM (e.g., Brunetti and Lazarian, 2007).

Galaxy clusters are objects where astrophysics and cosmology exists side by side. The overall dynamics is dominated by gravity with cosmological properties, given by their formation history and size. Astrophysical processes at the galactic scale are highly related with the surrounding environment and interactions with other galaxies. Given that we can probe each of their components separately with observations, clusters are powerful laboratories where to study the processes operating during galaxy formation and their

[4] Cosmic-rays are charged sub atomic particles originated in astrophysical processes.

effects on the surrounding intergalactic medium.

1.2 Observation of Magnetic Fields

The presence of magnetic fields in the Universe is confirmed by diffuse radio emission in the inter-galactic medium (see Beck, 2009, for a recent review) and in the intra-cluster medium, and by observations of *Faraday* rotation measures towards polarized radio sources within or behind the magnetized medium (e.g. Govoni, 2006). When studying magnetic fields in astrophysics, we face the problem of the physical complexity of those systems and the uncertainties inherent in the observations. In order to understand these limitations, we first introduce some observational techniques that are used to infer magnetics fields on astrophysical scales.

A more thorough discussion of observational techniques can be found in various references including Ruzmaikin, A. A. and Sokolov, D. D. and Shukurov A.M. (1988), we will briefly summarize in the same way as done by Widrow (2002)

1.2.1 Synchrotron Emission

When relativistic particles are in the presence of a magnetic field they change their energy states while spiraling in the field lines, therefore release photons in the so called form of "synchrotron" emission. Given this emission, it can be used to study magnetic fields in astrophysical sources ranging from pulsars to clusters of galaxies. The total synchrotron luminosity from a source give us a primary estimates for the strength of magnetic fields in galaxies and clusters. To be able to study synchrotron sources, we rely on a basic assumptions on the energy distributions between magnetic and electrons, which commonly we assumed to be in equipartition. The first studies commenting on the possibility to use this emission and their polarization degree of this emission as an indicator of the structure the field, were carried out by (Ginzburg and Syrovatskii, 1969).

For a single electron in a magnetic field $\mathbf{B}$, the emissivity as a function of frequency ν and electron energy E is

$$J(\nu, E) \;\propto\; B_\perp \left(\frac{mc^2\nu}{\nu_L}\right)^{1/3} f\left(\frac{mc^2\nu}{E\nu_L}\right) \tag{1.4}$$

where $B_\perp$ is the component of the magnetic field perpendicular to the line of sight, $\nu_L = (eB_\perp/2\pi mc)$ is the Larmor frequency [5] , and $f(x)$ is a cut-off function which approaches unity for $x \to 0$ and vanishes rapidly for $x \gg 1$.

The total synchrotron emission from a given source depends on the energy distribution of electrons, $n_e(E)$. A commonly used class of models is based on a power-law distribution

$$n_e(E)dE = n_{e0}\left(\frac{E}{E_0}\right)^{-\gamma} dE \tag{1.5}$$

assumed to be valid over several ranges in energy. The exponent γ is called the spectral index while the constant $n_{e0} \equiv n_e(E_0)$ sets the normalization of the distribution.

[5] This frequency given the precession of the particle by the torque between the magnetic field and the magnetic momentum of particle

The synchrotron emissivity is $j_\nu \equiv \int J(\nu, E) n_e(E) dE$. Eq. (1.4) shows that the synchrotron emission at a frequency ν is dominated by electrons with energy $E \simeq m_e c^2 (\nu/\nu_L)^{1/2}$, i.e., $\nu \simeq \nu_c$, so that to a good approximation, we can write $J(\nu, E) \propto B_\perp \nu_c \delta(\nu - \nu_c)$. Giving us a power-law distribution of Eq. (1.5)

$$j_\nu \propto n_{e0} \nu^{(1-\gamma)/2} B_\perp^{(1+\gamma)/2} . \tag{1.6}$$

Assuming equipartition of the magnetic field with relativistic electron density ϵ_{re} one can use Eq. (1.6) to have an estimate from the synchrotron emission of the magnetic field. As a consequence, $B/B_{\rm eq}$ sets the scale for the thickness of radio synchrotron halos. A field as small as $0.1 B_{\rm eq}$ requires higher particle energies to explain the synchrotron emission data. However, high energies imply large propagation lengths and hence an extended radio halo (scale height ~ 30 Kpc) in conflict with observations of typical spiral galaxies. Conversely, a field as large as $10 B_{\rm eq}$ would confine particles to a thin disk ($\sim 300\,$pc) again in conflict with galaxy observations.

In our Galaxy, the validity of the equipartition assumption can be tested because we have direct measurements of the local cosmic-ray electron energy density and estimates of the local cosmic-ray proton density. A combination of the radio synchrotron emission measurements with these results yields a field strength in excellent agreement with results derived from equipartition arguments (Beck et al., 2002).

While synchrotron radiation from a single electron is elliptically polarized, the emission from an ensemble of electrons is partially polarized because of the stochasticity of the emission. For a regular magnetic field and power-law electron distribution, the polarization will be constrained by the spectral index γ, giving more steep distributions high polarizations. In the same line of thought, one can imagine that as much polarized the source much stronger the magnetic field. However, if the field is highly tangled, the polarization also will be low.

On the largest scales, like those of filaments, magnetic fields are notoriously difficult to measure by this method, because we require either a high density of electrons and the presence of relativistic particles, which is not necessary the case in low density regions.

1.2.2 Faraday rotation

Electromagnetic waves, propagating through a region with magnetic field, experience Faraday rotation because circular polarized states travel with different phase velocities. Polarized light propagating through an astrophysical medium will be affected, particularly inside galaxy clusters or galaxies. This effect is similar to the birefringence of polarized light transmitted through some media, but in this case is caused by the magnetic field component in the propagation direction. For linearly polarized radiation, this results in a rotation of the electric field vector along the path length by an angle

$$\varphi = \frac{e^3 \lambda^2}{2\pi m_e^2 c^4} \int_0^{l_s} n_e(l) B_\parallel(l) dl + \varphi_0 \tag{1.7}$$

where m_e is the mass of the electron, λ the wavelength of the radiation, φ_0 the initial polarization angle, and $B_\parallel$ the line-of-sight component of the magnetic field. Here, $n_e(l)$ is the density of thermal electrons along the line of sight from the source ($l = l_s$) to the observer ($l = 0$). φ is usually written in terms of the rotation measure, RM:

$$\varphi = (RM)\,\lambda^2 + \varphi_0 \tag{1.8}$$

where

$$\begin{aligned} RM &\equiv \tfrac{e^3}{2\pi m_e^2 c^4} \int_0^{l_s} n_e(l) B_\parallel(l) dl \\ &\simeq 810 \int_0^{l_s} n_e B_\parallel dl \end{aligned} \tag{1.9}$$

being in the last equation the RM in $\mathrm{rad\,m^{-2}}$, n_e in $\mathrm{cm^{-3}}$, the magnetic field in μG and the distances in Kpc. In general, the polarization change has to be measured at three or more wavelengths in order to determine RM accurately and remove the $\varphi \equiv \varphi \pm n\pi$ degeneracy.

By convention, RM is positive for a magnetic field directed towards the observer. The Faraday rotation angle includes contributions from all magnetized regions along the line-of-sight. Following Kronberg and Perry (1982) we decompose RM into three basic components:

$$RM = RM_g + RM_s + RM_{ig} \tag{1.10}$$

where RM_g, RM_s, and RM_{ig} are the contributions to the rotation measure due to the Galaxy, the source itself, and the intergalactic medium respectively. When we mention RM_s we refer as the effect in the local environment of the source, because the source itself emits polarized independent on the wavelength, without any Faraday effect. From magnetic field observation in other galaxies and from radio sources inside our Galaxies we are able to build simplified magnetic field models of our Galaxy (Spergel et al., 2007; Sun et al., 2008). Using those models, Waelkens et al. (2009) developed mock observations of Faraday rotation measurements and other observables, helping us to distinguish between the different components of the total signal.

Note that in the case of studies of objects with a small angular size compared with the typical 3 degree reversal scales found in our Galaxy, it is usually assumed to have a constant or smooth contribution. Therefore, in the cases of galaxy clusters as RM_s, the variations have a small angular size and studies focus en relative values, the contribution of the effects from our Galaxy and the RM_{ig} are neglected.

Measurements of the magnetic field strength have been successful mainly in high density regions (e.g. galaxies and galaxy clusters), and fields significantly below the μG level can hardly be detected, because of the low electron densities of such environments. In order to study such low magnetic field strengths, even more indirect methods have to be used. Thereby, statistical approaches are a valuable tool, as they allow to measure very weak signals, otherwise not be detectable. Such statistical approaches (like correlation functions) measure the integrated signal over the whole sample of available RMs, see section 1.4.

1.2.3 Zeeman Splitting

In vacuum, the energy levels of the electrons of an atom are independent of the direction of its angular momentum vector. A magnetic field lifts this degeneracy by defining a particular spatial direction. If the total angular momentum of an atom is $\mathbf{J}$ = spin $\mathbf{S}$ plus

orbital angular momentum **L** there will be $2j+1$ levels where j is the quantum number associated with **J**. The splitting between neighboring levels is $\Delta E = g\mu_B$ where g is the Lande factor which relates the angular momentum of an atom to its magnetic moment and μ_B is the Bohr magneton [6]. This effect, known as Zeeman splitting, is of historical importance as it was used by Hale (1908) to discover magnetic fields in sunspots, providing the first evidence for extraterrestrial magnetic fields.

Zeeman splitting is the most direct method to observe astrophysical magnetic fields. Once ΔE is measured, $\overline{B}$ can be determined without additional assumptions. Moreover, Zeeman splitting is sensitive to the magnetic field at location of the emission, without any integrated or projection effects, besides the contribution from all the emitters in that particular place.

Unfortunately, the Zeeman effect is extremely difficult to observe. The line shift associated with the energy splitting is

$$\frac{\Delta\nu}{\nu} = 1.4g\frac{B}{\nu} \tag{1.11}$$

This effect compete with the Doppler broadening due thermal movements, being frequently observed as an abnormal[7] broadening of the line. Therefore, positive detections have to be constraint to regions of low temperature and high magnetic field.

Within our Galaxy, Zeeman effect measurements have provided information on the magnetic field in star forming regions and near the Galactic center. Of particular interest are studies of Zeeman splitting in water and OH masers performed by Reid and Silverstein (1990). Their results are consistent with those found in radio observations and, as they stress, provide *in situ* measurements of the magnetic field contrary to the integrated field along the line-of-sight of radio observations.

Robishaw et al. (2008) studied a set of ultra-luminous infrared galaxies and found significant Zeeman splitting and line-of-sight magnetic field strengths ranging from $\sim 0.5 - 18\mu$G. This detections are consistent with synchrotron observations and the field strengths are similar to those measured in Galactic OH masers. This suggest that the local process of massive star formation is similar, despite the variety of conditions.

1.2.4 Polarization of Optical Starlight

Polarized light from stars can reveal the presence of large-scale magnetic fields in our Galaxy and those nearby. Hiltner (1949) attempted to observe polarized radiation produced in the atmosphere of stars by studying eclipsing binary systems. He expected to find time-variable polarization levels of $1-2\%$. Instead, he found polarization levels as high as 10% for some of the stars but not all. While the polarization degree for individual stars did not show the expected time-variability, polarization levels appeared to correlate with position in the sky. This observation led to the conjecture that a new property of the interstellar medium (ISM) had been discovered. Coincidentally, it was just at this time that Alfvén (1949) proposed the existence of a galactic magnetic field to confine the cosmic rays propagation. The connection between polarized starlight and a galactic magnetic field was made by Davis and Greenstein (1951). They suggested that elongated dust grains would have a preferred orientation in a magnetic field: for prolate grains, one

[6] Which is defined by $\mu_B = e\hbar/2m_ec = 9.3\times10^{-21}\,\mathrm{erg\,G^{-1}}$, and represent the magnetic moment of an electron.
[7] From the thermally broadened line

of the short axes would coincide with the direction of the magnetic field. The grains, in turn, preferentially absorb light polarized along their long axis, i.e., perpendicular to the field. The net result is that the transmitted radiation has a polarization direction parallel to the magnetic field.

Polarization of optical starlight has limited value as a probe of extragalactic magnetic fields, for several reasons. There is at least one other effect that can lead to polarization of starlight, namely anisotropic scattering in the ISM. Also, the starlight polarization effect is self-obscuring since it depends on extinction. There is approximately one magnitude of visual extinction for each 3% of polarization. In other words, a 10% polarization effect must go hand in hand with a factor of 20 reduction in luminosity, making this method extremely difficult to use. Still, the precise mechanism by which dust grains are oriented in a magnetic field is not well understood.

1.3 Magnetic field in galaxy clusters

Cluster magnetic fields have been treated as secondary topics in reviews of cluster atmospheres (Sarazin, 1988; Fabian, 1994), and in general reviews of cosmic magnetic fields (Kronberg, 1996; Ruzmaikin, A. A. and Sokolov, D. D. and Shukurov A.M., 1988). The only dedicated review on cluster magnetic fields is Carilli and Taylor (2002).

We will attempt to synthesize various of these works, showing the develop of a general picture for cluster magnetic fields, having in mind that there is a significant differences between clusters, and even within a given cluster atmosphere.

Radio halos

A fraction ($\sim, 30\%$) of rich clusters have observable radio halos. These radio-halo clusters share a number of properties, such as a large homogeneous hot intra-cluster medium and the absence of a central dominant galaxy (the so called cD galaxy).

Large et al. (1959) discovered a radio source in the Coma cluster that was extended even when observed with large beam size (a 45 arcmin resolution). Later, this source (Coma C) was studied by Willson (1970) who found that it had a steep spectral index and meaning that this emissions could not be made up of individual sources, but instead was a smooth "radio halo" with no structure on scales less than 30 arcmin. Furthermore, if there is equipartition between the energy stored in particles and magnetic fields, Burbidge (1959), inferred that the emission mechanism was likely to be synchrotron with a magnetic field strength of 2 μG, The equations for deriving minimum energy fields from radio observations are given in Miley (1980). Estimates for minimum energy magnetic field strengths in cluster halos range from 0.1 to 1 μG (Feretti et al., 1999a). One of the best studied halos is in Coma, for which Giovannini et al. (1993); Bonafede et al. (2010) report a minimum energy magnetic field of 0.4 μG. In Fig. (1.2) we show an image obtained of the radio halo in the Coma cluster, taken from Feretti et al. (1995). Easily we observe the extended emission (gray area), compared with the radio sources (back areas).

Using the Northern VLA Sky Survey and X-ray selected samples as starting points Giovannini and Feretti (2000) have performed moderately deep VLA observations (integrations of a few hours) which have more than doubled the number of known radio halo sources. Several new radio halos have also been identified since then. These radio halos typically have sizes $\sim$ 1Mpc, steep spectral indices, low polarizations, low surface

brightnesses, and centroids close to the cluster center defined by the *X-ray* emission. A strong correlation between cluster *X-ray* and radio halo luminosity has been found, as well as a correlation between radio and *X-ray* surface brightnesses in clusters (Govoni et al., 2001).

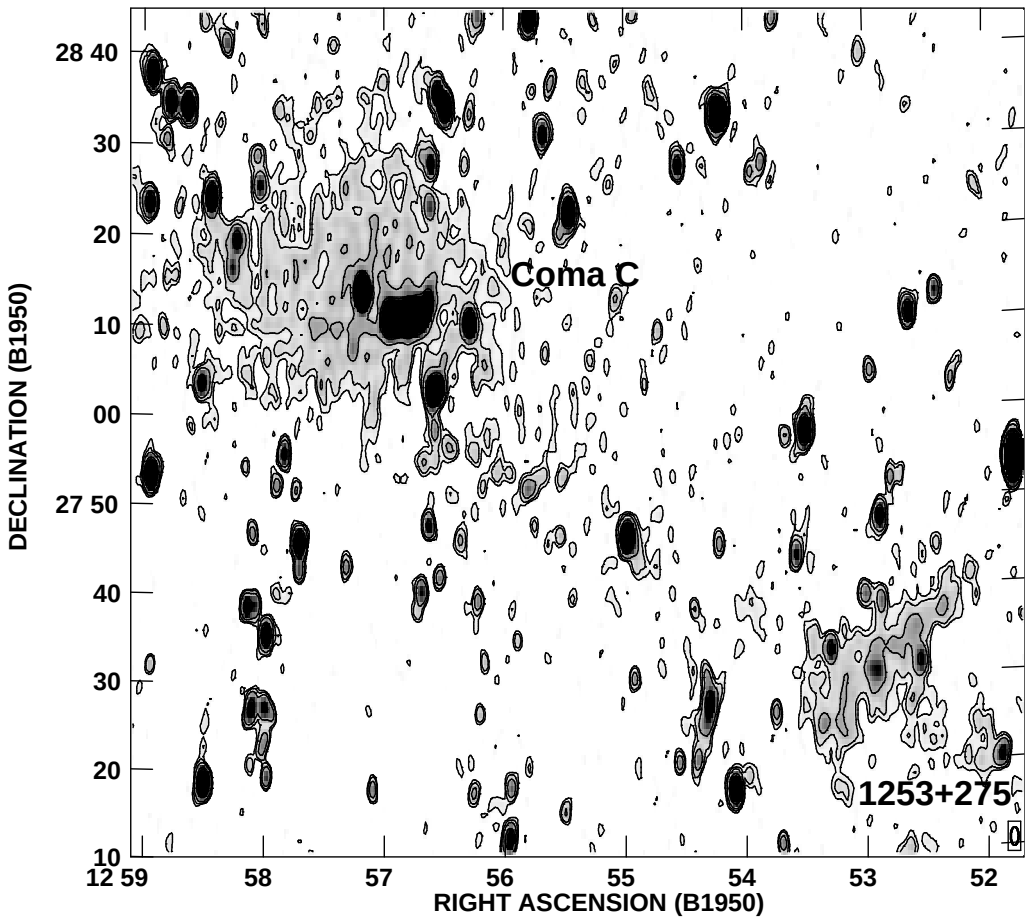

Figure 1.2: WSRT radio image of the Coma cluster region at 90 cm, with angular resolution of $55'' \times 125''$ (HPBW, RA $\times$ DEC) from Feretti et al. (1995) Labels refer to the halo source Coma C and the relic source 1253+275. The grey scale range displays total intensity emission from 2 to 30 mJy/beam while contour levels are drawn at 3, 5, 10, 30, and 50 mJy/beam. The bridge of radio emission connecting Coma C to 1253+275 is resolved and visible only as a region with an apparent higher positive noise. The Coma cluster is at a redshift of 0.023, such that $1' = 27$ Kpc.

Brunetti et al. (2001) present a method for estimating magnetic fields in the Coma cluster radio halo independent of minimum energy assumptions. They base their analysis on considerations of the observed radio and X-ray spectra, the electron inverse Compton and synchrotron radiative lifetimes, and reasonable mechanisms for particle re-acceleration. They conclude that the fields vary smoothly from 2 ± 1 μG in the cluster center, to 0.3 ± 0.1 μG at radius of 1 Mpc. Recently, Donnert et al. (2010) constraint these conclusions with numerical simulations, finding agreement with current observations.

Radio relics

A possibly related phenomena to radio halos is a class of sources found in the outskirts of clusters known as radio relics. Like the radio halos, these are very extended sources without an identifiable host galaxy. Radio relics are often elongated or irregular in shape and are strongly polarized. One of the first explanations to explain these objects was that these are the remnants of a radio jet associated with an active galactic nucleus (therefore the name), that since stop its activity the jet continue traveling in the ICM. A problem with this idea is that, once the energy source is removed, the radio source is expected to fade on a timescale $\ll 10^8$ years due to adiabatic expansion, inverse Compton, and synchrotron losses. This short timescale precludes significant motion of the host galaxy from the vicinity of the radio source.

Another explanation is that the relics are the result of relativistic particles accelerated in shocks produced during cluster mergers (Ensslin et al., 1998), or are radio sources revived by compression associated with those mergers (Enßlin and Gopal-Krishna, 2001). In these cases equipartition field strengths for relics range from $0.4-2.7\mu$G (Ensslin et al., 1998).

Cluster center sources

Rotation measures in cluster centers can be derived, as we already mentioned, from multi-frequency polarimetric observations of sources by measuring the position angle of the polarized radiation as a function of frequency. However thought these effect, only the magnetic field component along the line-of-sight is measured, so the results depend on the assumed magnetic field topology.

The Cygnus A observations were the first to show that the large RM must arise in an external screen of magnetized, ionized plasma, but cannot be Galactic in origin. Dreher et al. (1987) considered a number of options for the Faraday screen toward Cygnus A, and concluded that the most likely site was the X-ray emitting cluster atmosphere enveloping the radio source. They infer values for magnetic fields around $2 \sim 10$ μG to explain the observed RMs.

Since those observations, RM studies of cluster center radio sources have become a standard tool to measure cluster core magnetic fields. RM studies of radio galaxies in clusters can be divided into studies of cooling-flow and non-cooling-flow clusters. Typical mass cooling flow rates are 100 $M_\odot$ yr^{-1}. Cooling-flow clusters are more dynamically relaxed than non-cooling flow clusters which often show evidence of cluster mergers (Markevitch et al., 2002).

Radio galaxies in cooling flow clusters attracted some of the first detailed RM studies by virtue of their anomalously high RMs. Out of a sample of 14 cooling-flow clusters with strong embedded radio sources Taylor et al. (2002), found that 10 of 14 sources display RMs in excess of 800 rad m^{-2}. Current data are consistent with all radio galaxies at the center of cooling flow clusters having extreme RMs, with the magnitude of the RMs roughly proportional to the cooling flow rate (see Fig. 1.3).

From the shapes of the RM distributions is found that the magnetic fields are not regularly ordered on cluster scales, however they have characteristic coherence lengths of scales up to several Kpc (one example is shown in chapter 3). The RM distributions at the centers of cooling flow clusters tend to have reversals with coherence lengths of

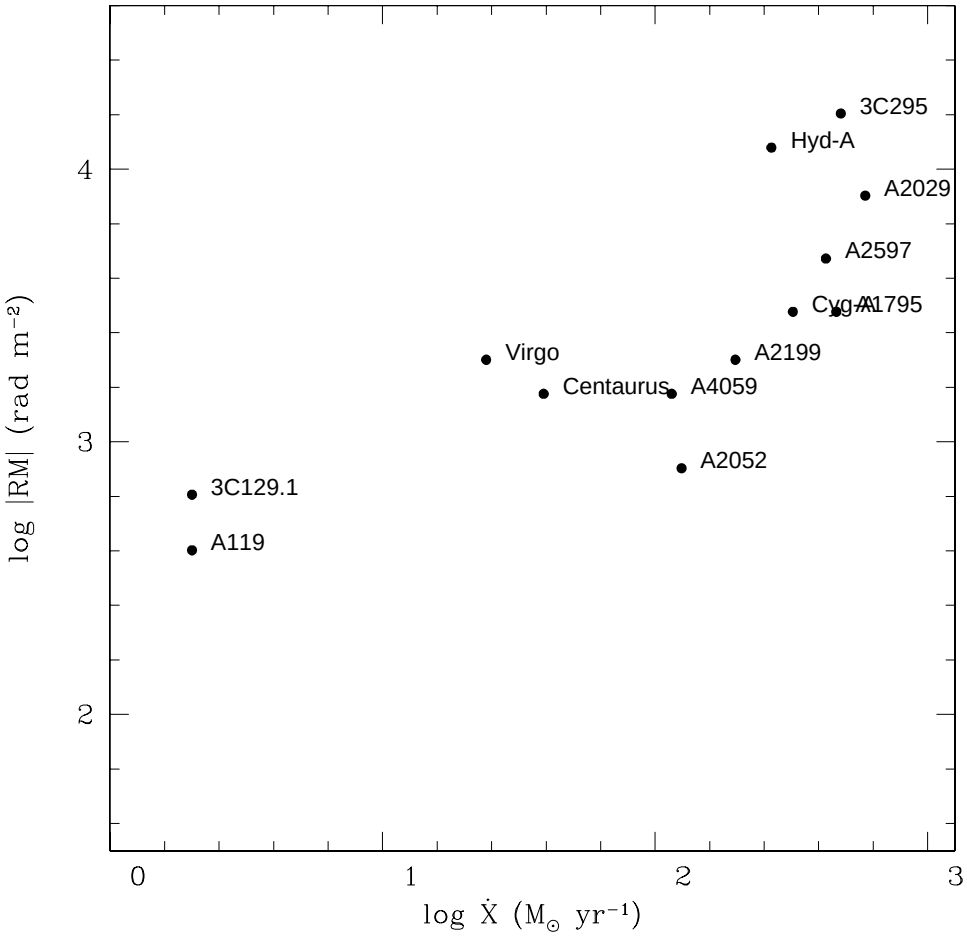

Figure 1.3: The maximum absolute RM plotted as a function of the estimated cooling flow rate, $\dot{X}$, for a sample of X-ray luminous clusters with measured RMs from Taylor et al. (2002). Both RM and $\dot{X}$ are expected to depend on density to a positive power, in that sense the correlation is expected.

$5 \sim 10$Kpc. Larger "patches" up to 30 Kpc are seen for example in Cygnus A. In both Cygnus A and Hydra A one can find stripes of alternating high and low RM. Such bands are also found in the non-cooling flow cluster sources (Eilek and Owen, 2002), along with slightly larger coherence lengths of $15 \sim 30$Kpc. In Hydra A there is a strong trend for all the RMs to the north of the nucleus to be positive and to the south negative. To explain this requires a field reversal and implies a large-scale (100Kpc) ordered component to the cluster magnetic fields in Hydra A.

Minimum cluster magnetic field strengths can be estimated by assuming a constant magnetic field along the line-of-sight through the cluster and, form to the *X-ray* observations, is fitted a radial electron density distribution, commonly using a modified King sphere model (Cavaliere and Fusco-Femiano, 1976). Such estimates usually lead to magnetic field strengths of $5--10$ μG in cooling flow clusters, and the half in non-cooling flow clusters.

In a reanalysis of the Abell 119 measurements, Dolag et al. (2001b) found that the field scales as $n_e^{0.9}$. This dependence is marginally steeper than that expected assuming flux conservation, for which the tangled field scales as $n_e^{2/3}$, and significantly steeper than that expected assuming a constant ratio between magnetic and thermal energy density,

for which the tangled field scales as $n_e^{1/2}$ for an isothermal atmosphere. This can lead us to weight different the inner from the outer regions in the cluster, if the density scales up steeply, and should be taken in consideration.

Extreme rotation measurements have been observed in a variety of different morphologies. This means that high rotation measurements are not a particular phenomena from strong interactions between galaxies and its environment, but are more likely to be linked to cluster scales characteristic of the inter cluster medium.

1.4 Large scale magnetic fields in the Universe

Spatially coherent magnetic fields are ubiquitous in galaxies and galaxies clusters. From the theoretical side, it is not well understood whether these fields are flux-frozen primordial fields or they originated by the dynamo amplification from other phenomena. If those large scale ($\ll 1$ Mpc) fields exist unambiguously, they can flavor one of those scenarios, depending on their strength. Nevertheless, their existence might be of great importance to understand the way galaxies and clusters formed and accreted their baryons.

There is evidence of magnetic fields in galaxies at early times, setting up a serious challenge for the galactic dynamo hypothesis, since it would imply that there was a short amount of time for an effective field amplification. At present, the most convincing observations of galactic magnetic fields at intermediate redshifts come from rotation measurement studies of radio galaxies and quasars. However, as we already mentioned, Wolfe et al. (2008) estimated a magnetic field strength of 86μG at redshift $z \sim 0.7$, using the Zeeman splitting technique and obtaining one of the highest values for high redshift galaxies.

Athreya et al. (1998) studied 15 high redshift ($z > 2$) radio galaxies at multiple frequencies in polarized radio emission, founding significant rotation measurements in almost all of the sample, and even with several of the sources having $RM > 1000$ rad m^{-2}. The highest RM in the sample is 6000 rad m^{-2} for the $z \simeq 2.17$. Rotation measurements of this magnitude require micro-gauss fields that are coherent over several Kpc.

Faraday rotation of radio emission from high redshift sources can be used to study cosmological magnetic fields. For a source at a cosmological distance l_s, the rotation measure is given by the generalization of Eq. (1.9) appropriate to an expanding Universe:

$$RM \simeq 8.1 \times 10^5 \int_0^{l_s} n_e(l) B_{\parallel}(l) (1+z)^{-2} dl \tag{1.12}$$

The factor of $(1+z)^{-2}$ accounts for the redshift dilution of the electromagnetic fluxes as they propagate to the observer. We consider the contribution to this integral from cosmological magnetic fields. If the magnetic field and electron density are homogeneous across our observable volume, an all-sky rotation measurement map will result in a dipole distribution, with the amplitude depending on the evolution of B and n_e. The simplest assumption is that the co-moving magnetic flux and electron density are constant, i.e., $B(z) = B_0 (1+z)^2$ and $n_e(z) = n_0 (1+z)^3$. The cosmological component of the RM is then

$$RM_{ig} \sim \times 10^4 h^{-1} \cos(\theta) n_0 B_0, F_{\Omega_m, \Omega_\Lambda}(z) \tag{1.13}$$

where θ is the amplitude angle between the source and the magnetic field orientation, $F_{\Omega_m,\Omega_\Lambda}(z)$ concentrates all the cosmological factors and the integration in the line of sight

$$F(z) = \frac{H_0}{c} \int_0^{z_s} dz\,(1+z)^3\,\frac{dl}{dz} \tag{1.14}$$

Chosen a cosmological model and taking into the account of the expansion of the universe Eq. (1.2) the $\frac{dl}{dz}$ takes the form

$$\frac{dl}{dz} = \frac{c}{H_0(1+z)\ E(z)} \tag{1.15}$$

In Fig. (1.4), we plot F and RM_{ig} as a function of z_s for selected cosmological models. The path length to a source and hence the cosmological contribution to the RM are increasing functions of z_s, as is evident in Fig. (1.4). We can see that the nowadays flavored cosmological model (the solid line in the plot) show an increase of the order of 20 just for cosmological effects.

Combining Eq. (1.13) and Eq. (1.15), with rotation measurement data from high-redshift galaxies and quasars, we can constrain the strength of Hubble-scale magnetic fields. The difficulty is that the source and the Galaxy contributions to the RM are not completely known. However, it can be modeled as done by Waelkens et al. (2009) or one can try to suppress the Galaxy contribution. Kronberg and Simard-Normandin (1976) found that even at high galactic latitude, some objects have $RM > 200\,\mathrm{rad\,m^{-2}}$. In particular, the high Galactic latitude subsample that they considered was evidently composed of two populations, one with $\langle RM^2\rangle^{1/2} \simeq 50\,\mathrm{rad\,m^{-2}}$ and another with $\langle RM^2\rangle^{1/2} \simeq 200\,\mathrm{rad\,m^{-2}}$. The High-RM subsample is more likely to be saturated by the source phenomena and not from the inter galactic contribution, and given that we ensure low galactic contamination at high latitudes, they conclude that the best chances to constrain Hubble-scale magnetic fields are studying the galactic polar sectors and low-RM subsample. The galaxies in this work extended to $z \simeq 3.6$ though most of the objects were at $z < 2$.

In an not so ideal case, the pattern of the cosmological contribution across the sky will be more complicated than a simple dipole, because the electron density or/and magnetic field can vary. However, still the average cosmological rotation measurement over the sky will be zero and the variance σ^2_{RM} will increase with redshift. Kronberg and Perry (1982) considered a simple model in which clouds of uniform electron density and magnetic field are scattered at random throughout the Universe.

The Kronberg-Perry model was motivated by spectroscopic observations of QSOs which reveal countless hydrogen absorption lines spread out in frequency by the expansion of the Universe. This dense series of lines, known as the lyman-α forest, are thought to be a large number of neutral hydrogen clouds at cosmological distances. Clearly, the limits derived from rotation measurement data will depend on the model one assumes for the lyman-α clouds. (Blasi et al., 1999) suggested another model for the intergalactic medium in which the Universe is divided into cells of uniform electron density following some particular distribution and the magnetic field is parametrized by its coherence length and mean field strength. Random lines of sight are simulated for various model universes. The results suggest that a detectable variance in RM is possible for magnetic fields as low as $B_0 \simeq 6\ \mu$G. The enhanced sensitivity relative to the Kronberg and Perry (1982)

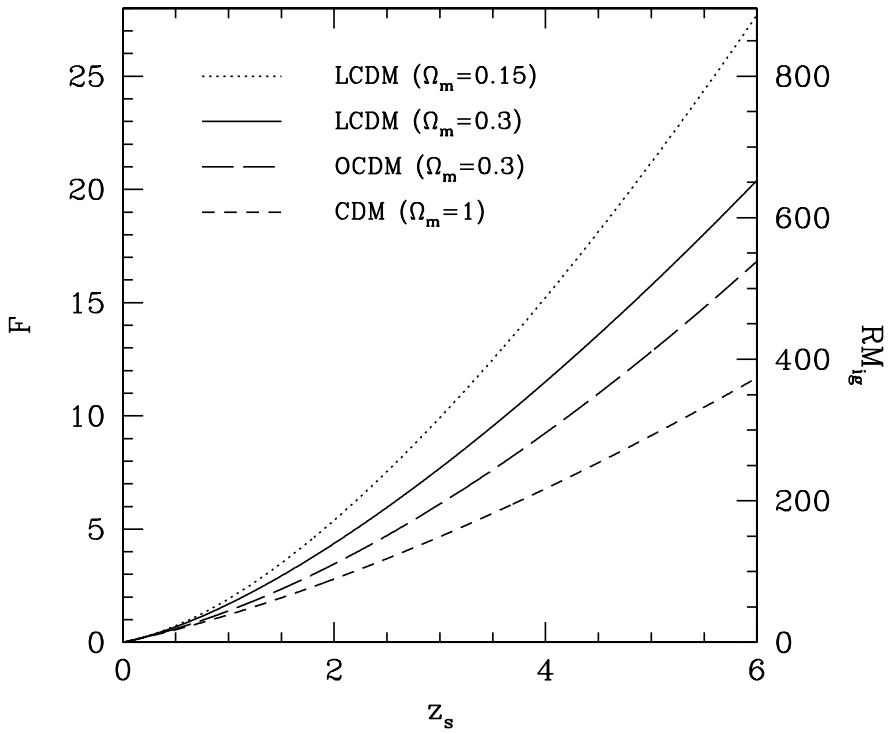

Figure 1.4: Intergalactic contribution to the rotation measure (RM_{ig}) as a function of source redshift z_s. The left-hand vertical axis gives the function $F(z_s)$ as defined in Eq. (1.14). The right-hand axis gives RM_{ig} assuming a $1\,\mu$G field, $h_{75} = 1$, $n_{e0} = 10^{-5}\,\mathrm{cm}^{-3}$, and $\theta = 0$. Curves shown are for the standard cold dark matter (CDM) model ($\Omega_m = 1$), two LCDM models (CDM with a cosmological constant) ($\Omega_m = 0.15; \Omega_\Lambda = 0.85$ and and $\Omega_m = 0.3; \Omega_\Lambda = 0.7$) and an open CDM model ($\Omega_m = 0.3; \Omega_\Lambda = 0$). Taken from Widrow (2002)

observations is primarily due to the large filling factor assumed for the clouds. Recently, Dolag et al. (2010) found that maybe this is the case. However, Stasyszyn et al. (2010) showed that given the current instrumentation, we are still unable to identify this signal (see chapter 4).

Further improvements in the use of Faraday rotation to probe cosmological magnetic fields may be achieved by looking for correlations between them (Kolatt, 1998). The correlation function of the position of the sources and its RM strength increases as N_c^2 where N_c is the average number of clouds along the line of sight. By contrast, σ^2_{RM} increases linearly with N_c, meaning that the signal in a correlation map can be enhanced by an order of magnitude or more, depending on the number of clouds that we are considering. However this methods can be affected by other issues that we study in chapter 4.

1.5 Numerical simulations of cluster formation

The first simulations of cluster formation have been performed in the 1970s (White, 1976) and were focused in testing the idea of gravitational instability. The first simulations of galaxy clusters which followed the dynamics of both baryons and dark matter where performed in the 90s (Katz and White, 1993a). The predictions of the *self–similar* model have been tested by a number of authors against hydrodynamical simulations, which include only the effect of gravitational heating of baryons(e.g., Navarro et al., 1995; Nagai et al., 2007). These simulations generally confirmed the scaling relations, as defined by Eq. (1.3), for the average quantities in radial profiles, as well as their evolution with redshift. However, the *self–similar* model is far too simple to capture all of the complexities of cluster formation and the detailed observations. Numerical cosmological simulations carried out on parallel supercomputers represent the modern tool to describe these complexities. Such simulations begins at a sufficiently early epoch of the Universe when density fluctuations were small and can be specified using analytical theories of primordial perturbations. Those initial conditions are usually generated as realizations of a density field with statistical properties of the adopted cosmological model. The simulations co-evolve the collisionless dark matter and normal baryonic components from the initial conditions, by integrating numerically the equations governing the dynamics of those components represented by density and velocity fields.

Observational probes, such as the Cosmic Microwave Background, the statistics of the population of galaxies and galaxy clusters, and the properties of absorption systems in the spectra of distant quasars, have provided tight constraints on the cosmological model (e.g., Komatsu et al., 2009, and references therein). The main challenge for actual simulations is to follow the dynamics driven by gravitational instability and the gas-dynamical processes that contributes in different forms to the correct evolution of the cosmic baryons, when this evolutions becomes highly non linear.

In simulations we are able to only treat a subset of equations that will characterize the system, by solving them discretizing and sampling the initial phase space and then integrating their equations of motion. The dynamics of diffuse baryonic matter is expected to be highly collisional and therefore we are able to use hydrodynamics techniques to model them.

The addition of baryons in the simulations allow to predict properties of clusters in *X-rays*. Those simulations confirmed that gas is heated up to emitting temperatures during cluster formation, only due to the adiabatic compression and shocks. Early simulations are successful in reproduce general morphological characteristics of the *X-ray* observations. The simulations also demonstrated that gas in the inner regions of clusters is close to be in hydrostatic equilibrium, confirming the predictions of simple models from *X-ray* observations and *self–similar* models. Further progress in simulations show that while the outer regions of clusters are quite regular, nearly *self–similar*, the inner regions do not converge to a simple solution and show evidence of galaxy formation effects and energy injection.

As for the numerical schemes behind the hydrodynamics simulations the two most commonly used approaches are grid-less smoothed particle hydrodynamics (SPH) and grid-based *Eulerian* schemes. In the SPH, fluid elements describing the system are sampled and represented by particles discretizing the mass, and the dynamic equations are obtained from the Lagrangian form of the hydrodynamic conservation laws (see

Monaghan, 2005, for a recent review, and chapter 2). The main advantage of SPH lies in its Lagrangian nature as there is no grid to constrain the dynamic range in spatial resolution or the global geometry of the modeled systems.

Eulerian methods, sample the space of our physical system into grid cells, and thus follow the exchange of different properties between them. These scheme perform well for flows with shocks, contact discontinuities and for moderately subsonic and turbulent flows. Additionally the adoption of adaptive mesh refinement (AMR) techniques in cosmological simulations has changed the situation in the last ten years (e.g., Kravtsov et al., 2002; Teyssier, 2002; Loken et al., 2002), opening new frontiers for *Eulerian* schemes. The AMR is used to increase the spatial and temporal resolution of numerical simulations beyond the limits imposed by the available hardware and dynamically to adapt to the astrophysical system. This is done by using fine mesh only in regions of interest (as high-density regions or regions of steep gradients in gas properties) and coarse meshes in other regions (low-density regions or smooth flows).

It is important to keep in mind that although different numerical schemes aim to solve the same sets of equations, the actual discretized versions solved are not the same. This does lead to differences in the numerical solution (Agertz et al., 2007). However, the use of both techniques is useful and complementary in highlighting possible systematic errors associated to a given technique. Such systematics errors can only be identified in comparisons of simulations performed with different techniques.

In the case of MHD simulations, *Eulerian* approaches leaded the development from many years. Their flux constrain and shock capturing capabilities, make more easy to deal with MHD instabilities. Early tries in SPH (Phillips and Monaghan, 1985) had only good results for low β_{plasma}[8] and low Mach number shocks. However, the adaptive characteristics made the studies to continue (Balsara and Spicer, 1999; Omang et al., 2006; Dolag et al., 1999; Price and Monaghan, 2005), and nowadays there are plenty of schemes to reduce magnetic tensile instabilities in SPH. Particularly, in our case we take the advantage of the improvements in cosmological simulations given by SPH (Springel, 2005).

As we already discussed, magnetic fields are indeed observed in galaxy cluster cores (e.g., Eilek and Owen, 2002; Carilli and Taylor, 2002) and there is evidence towards their existence in whole cluster volume (e.g., Govoni and Feretti, 2004; Eilek et al., 2006), therefore can contribute as a non-thermal component. By the use of simulations, magnetic fields are also predicted to be effectively amplified from the primordial values in mergers during cluster formation (Dolag et al., 1999, 2002; Brüggen and Hoeft, 2006; Subramanian et al., 2006; Dolag and Stasyszyn, 2009). The questions that then arise are: how dynamically important the magnetic fields actually are?, how they affect the turbulent motions? and which magneto-hydrodynamic effects are important in the ICM?

MHD cosmological simulations suggests that magnetic fields generally provide a minor contribution to the total pressure (Dolag et al., 2001a), while they can become dynamically non-negligible in peculiar cases involving strong mergers (Dolag and Schindler, 2000) or in strong cooling flows (Dubois and Teyssier, 2008). Xu et al. (2009) feed the magnetic fields from AGNs, being further amplified by the ICM turbulence through small-scale dynamo processes, showing that can be the origin of cluster-wide magnetic fields. The strong link between turbulence processes and magnetic

[8] β_{plasma} is defined as the thermal over magnetic energy ratio

field modifies the spectral slope of those quantities, therefore studying them we can determine how this phenomena take place (Li et al., 2008a; Brüggen and Hoeft, 2006; Dolag et al., 2002). However, the inclusion of magnetic effects has not yet became standard in cosmological simulations.

1.6 Open questions

Magnetic fields are present everywhere, independent of the environment or related physical phenomena. As we discussed, baryons and magnetic fields in space are usually tightly coupled. However, from simulations and observations, we know that, at first approximation we do not need to follow the MHD equations or explicit baryonic evolution to understand the cosmic structure of the Universe. The overall structure, voids and groups, are reasonably well determined by gravity alone. However, baryon physics become important on small scales, which later on manifest themselves in galactic scales (i.e. by wind, AGN feedback, etc.), modifying the environment, as we are able to observe.

In the preceding sections we briefly commented the techniques which are used to carry out cosmological simulations of cluster formation. Many of the observed properties of clusters, such as scaling relations between observables and total mass, radial profiles of entropy and density of the intra-cluster gas and radial distribution of galaxies are reproduced quite well. In particular, the outer regions of clusters exhibit scaling with mass close to the scaling expected for a *self-similar* model. However, simulations generally do not reproduce the observed "cool core" structure of clusters. The amount of cooling that simulated clusters generally show in their central regions, make the temperature and energy profiles incorrect. These discrepancies point towards an important role played by additional physical processes, beyond those already included in the simulations.

The richness of observational datasets which are quickly becoming available need to be properly modeled by cosmological simulations. Although most of the processes that operate in clusters are not well understood, the comparison between observations and simulations, will be extremely useful to advance in their interpretation and to build theoretical models.

Nowadays, we reach the accuracy in studies that start to involve additional physics, such is the case of MHD. We can follow the complete structure formation (from an adiabatic collapse of the initial clouds) that in the case of magnetic fields cinch the field lines, and increases the magnetic fluxes, but how much this will affect the star formation process or baryon accretion is unknown. As we mention, there is a strong link between turbulence and magnetic fields. Current theoretical models favor the growth of magnetic fields by turbulent motions. Turbulence contributes to the chemical mixing and energy transport in the ICM, wherefore the study of magnetic field shed light on other physics where the magnetic fields are not directly linked.

Magnetic field observations of the Coma cluster (Bonafede et al., 2010) and of radio galaxies at redshift $z \simeq 2$, points towards the existence of a widespread cosmological field. The origin of this magnetic field is under debate, being the simplest hypothesis a primordial field which is amplified by the collapse of the proto-galaxy and subsequently maintained by some dynamo action, becoming the micro-gauss field observed in present-day galaxies and clusters. This simple model involves different process on different scales which should be proven, and in most of the cases can be modified by other

physical phenomena. Nowadays, observations and theory are reaching the point to make prediction.

To continue these studies we need to build an sufficiently accurate numerical scheme to compute these high non-linear systems. Even with simple models and assumptions, we can try to answer the following open questions

- How are magnetic fields distributed on scales larger than galaxy clusters? It is possible to measure them?
- Are models beyond *self-similar* capable to explain observations? Are they consistent with magnetic field profiles and Faraday rotation measurement?
- If the numerical $\nabla \cdot \mathbf{B} = 0$ constraint is not satisfied by simulations, which effects does this implies?
- Can we explain current observations with "ideal" MHD and non-radiative simulations only?
- Are magnetic field coupled to other processes happening in the inter galactic medium? How much?

Cosmological MHD simulations are already performed using finite-volume and finite-difference methods. Astrophysical fluid dynamics usually involve changes over several orders of magnitude in spacial, temporal and energetic scales. Thus, adaptivity is essential to study these problems. In that sense Smooth Particle Hydrodynamics, offers an elegant solution. However, it was not until recently that it was possible to successfully include MHD equations into a cosmological SPH formalism (Dolag and Stasyszyn, 2009). Such simulations can be used to either follow a primordial magnetic field (Li et al., 2008b) or the creation of magnetic fields in shocks through the so-called *Biermann* battery effect (Kulsrud et al., 1997; Ryu et al., 1998), on which a subsequent turbulent dynamo may operate. The latter process predicts magnetic field strengths in filaments with somewhat higher values (see Sigl et al., 2004) than predicted by simulations which start from a primordial magnetic seed field. However, they are in concordance with predictions of magnetic field values from turbulent amplification (Ryu et al., 2008).

Therefore, further investigations are needed to clarify the structure, evolution and origin of magnetic fields in the largest structures of the Universe, their observational signatures, as well as their interplay with other processes acting in galaxy clusters and the large scale structure of the Universe.

In the present work, we present the achievements done in the SPH-MHD formalism in a cosmological context, to clarify the possible effects of numerical errors done in simulations. We start in chapter 2, by briefly explaining how our numerical simulations are done and the different characteristics of different implementations. We applied these numerical schemes to galaxy clusters, showing the astrophysical differences and implications in chapter 3. In chapter 4 we show how simulations can help to estimate the values of the large scale magnetic field. Finally, we summarize our work in chapter 5.

Part II

Numerical Methods

Chapter 2

MHD - Smoothed Particle Hydrodynamics

A computer shall not waste your time or require you to do more work than is strictly necessary.

Jef Raskin (1945-2005)

One standard approach to solving the equations of fluid dynamics numerically is to discretize the space which the fluid occupies, often on a regular grid, defining the fluid properties in each cell and computing derivatives using finite volume differentiation. In astrophysical problems, the fluid dynamics usually is under changes in spatial, temporal and density scales over several orders of magnitude. Adaptivity is essential to face these problems and fix grid approaches might be too limited. Theses needs where faced with the development of procedures like adaptive mesh refinement (AMR), which gives additional space refinements in the regions where the physical processes needed to be calculated more accurately [1]. The implementation of such procedures is far from being trivial, although there are plenty codes these that offer that kind of solution. However, these methods still suffer from artifacts because astrophysical problems are frequently highly asymmetric, deriving in substantial artificial diffusion when solving derivatives or due errors in the non proper solution of Galilean invariance, independent of adaptive or fixed grids (see Springel, 2010, for instance).

An alternative to these methods is to follow the fluid not by discretizing space but matter. This means following portions of fluid defined by their masses, resulting in methods which are naturally adaptive. In this approach fluid quantities are carried by a set of interpolation tracers, so called particles, which follow the fluid motion. Each point particle is defined by a characteristic mass, the volume that represents is defined by the local spatial distribution of tracer particles, which also are used to calculate the interpolants for derivatives. [2]

The particle method is called Smoothed Particle Hydrodynamics (SPH) and was introduced by Lucy (1977) and Gingold and Monaghan (1977). It has found widespread use in astrophysics due to its ability to handle a wide range of problems involving complex, asymmetric phenomena with relative ease. SPH concepts are simple, the equations are

[1] Other approaches to this problem are to use unstructured grids (where typically the grid is reconstructed at each new time-step) or Lagrangian grid methods, where the grid shape deforms according to the flow pattern.

[2] To be precise derivatives can be evaluated either by interpolation over neighbouring particles, or via an hybrid approach by interpolation to an overlaid grid (referred to as particle-mesh methods).

self-consistently derived from physical principles, and thus the incorporation of additional physics modules is relatively straight forward. Adaptivity and scalability are natural features of the methods.

The SPH method, whose formal derivation will be given later in this chapter, ensures that changes in density and flow morphology are automatically taken into account. These properties, to some extent, allow the code to be naturally prepared to resolve high density regions as presented in many astrophysical problems, without much loss in computational effort in regions physically unimportant for the problem. A particular highlight of SPH is the natural coupling with N-Body techniques, that makes a big advantage in the calculation of gravity interactions and enables the use of well known procedures used in astrophysics.

In particular in N-Body techniques (namely via tree-codes) already construct the neighbour list to calculate the gravitational force. So this techniques offers a natural skeleton for SPH without any extra load. SPH has not reached a mainstream status as finite volume technique. In SPH the vector nature of magnetic fields, in comparisons with other scalar fields (i.e. temperature), can involve anisotropic stresses and lead to instabilities. The reason for this is that the magnetic stress can become negative depending on the morphology of the magnetic field lines and the numerical errors in the evolution, leading to the clumping of particles, and thus spurious forces arise. That was a mayor issue in the development of magnetohydrodynamics in SPH that resulted in instabilities that were not possible to solve properly until recent years. However, progress has been done in the treatment of those instabilities (Morris and Monaghan, 1997; Børve et al., 2001; Price and Monaghan, 2005). In particular non-radiative simulations of galaxy clusters within a cosmological environment which follow the evolution of a primordial magnetic seed field have been performed using SPH codes (Dolag et al., 1999, 2002, 2005a). We also gained insight in the field of galaxies studying their isolated evolution (Kotarba et al., 2009) and in interacting environments (Kotarba et al., 2010a,b). The difficulty here was again the dynamical ranges involved. Other works (i.e. Elstner et al., 2000) were done using finite boxes to focus on a small section, and then extrapolate that into the whole galaxy. All simulations have in common that instabilities that come from MHD dynamics. We are able now to handle them properly and we learnt were they came from.

In this chapter we provide an overview of the MHD-SPH method, including several improvements to regularize the field from instabilities. The chapter is organised as follows: In section 2.1 and 2.1.1 we will try to introduce some basic numerical concepts of SPH-MHD, in section 2.3 we focus on the changes needed to stabilize the code, later we will show some test cases in section 2.4 that help us to understand the code behavior and grade of success of our implementation, that finally we discuss in section 2.5.

2.1 Introduction to SPH

Cosmological investigations demand an enormous dynamic range in space and time. For example in studies of galaxy clustering, one would like to resolve until scales of 10 Kpc for individual galaxies in regions of hundreds of Mpc. System with crossing times of less than 10^6 years must be followed for 10^{10} years. The strength of *TreeSPH* in these kind of numerical simulations lies in its dynamical range and balance between accuracy and

resources like memory and time.

We have implemented the MHD equations in the cosmological SPH code GADGET (Springel et al., 2001; Springel, 2005), allowing us to explore the full size and dynamical range of state of the art cosmological simulations. Note that the implementation therefore is fully parallelized and benefits from many optimizations within the general parts of the code, especially the calculation of self gravity and optimization in data structures as well as work-load balancing. Therefore, this implementation is an ideal tool to follow the evolution of magnetic fields in astrophysics. GADGET also allows us to turn on the treatment of many additional physical processes which are of interest for structure formation and make interesting links with the treatment of magnetic fields for future studies. This includes thermal conduction (Jubelgas et al., 2004; Dolag et al., 2004b), physical viscosity (Sijacki and Springel, 2006), cooling and star-formation (Springel and Hernquist, 2003), detailed modelling of the stellar population and chemical enrichment (Tornatore et al., 2004, 2007) and a self consistent treatment of cosmic rays (Enßlin et al., 2007; Pfrommer et al., 2007). The MHD implementation at first approximation should be fully compatible with all these extensions but we are aware that the need of additional astrophysics and proper modifications of the algorithms to take into account the effects of the magnetic fields. All such processes are expected to increase the complexity and lead to a complicated interplay with the evolution of the magnetic field and would make it impossible to critically check the numerical effects caused by the different SPH-MHD implementations or the astrophysics itself. As a first step we want to investigate the numerical behavior of the different schemes implemented. Therefore, our work is mainly focused on non-radiative simulations, to emphasize the effects of the methods and exhaustively analyze their behavior.

2.1.1 Interpolants

The basis of the SPH approach is given by Monaghan (1992); Lucy (1977); Gingold and Monaghan (1977). For a recent review one can see Monaghan (2005) but we will try to briefly summarize the basics in this section. If we start with the trivial identity

$$A(\mathbf{r}_a) = \int A(\mathbf{r}_a)\delta(|\mathbf{r}_a - \mathbf{r}_b|)d\mathbf{r}_b, \tag{2.1}$$

where A is any variable defined on the spatial co-ordinates vector $\mathbf{r}$ [3] and δ refers to the Dirac delta function. This integral is then approximated by replacing the delta function with a smoothing kernel W with characteristic width h [4], such that

$$\lim_{h_a \to 0} W(\mathbf{r}_a - \mathbf{r}_b, h_a) = \delta(\mathbf{r}_a - \mathbf{r}_b), \tag{2.2}$$

thus

$$A(\mathbf{r}_a) = \int A(\mathbf{r}_b)W(|\mathbf{r}_a - \mathbf{r}_b|, h_a)d\mathbf{r}_b \ + O({h_a}^2). \tag{2.3}$$

The kernel function is normalised to unity as

$$\int W(\mathbf{r}_a - \mathbf{r}_b, h_a)d\mathbf{r}_j = 1. \tag{2.4}$$

[3] The indexes a,b represent different spatial positions, later on will this will be identified as the particles itself

[4] This variable is called smoothing length - Hsml.

Finally the integral (2.3) is discretized onto a finite set of interpolation points (the particles) by replacing the integral by a summation and the mass element ρdV with the particle mass m, i.e.

$$\begin{aligned} A(\mathbf{r}_a) &= \int \frac{A(\mathbf{r}_b)}{\rho(\mathbf{r}_b)} W(|\mathbf{r}_a - \mathbf{r}_b|, h)\rho(\mathbf{r}_b)d\mathbf{r}_b + O({h_a}^2), \\ &\approx \sum_{b=1}^{N} m_b \frac{A_b}{\rho_b} W(|\mathbf{r}_a - \mathbf{r}_b|, h_a), \end{aligned} \tag{2.5}$$

where the subscript a refers to the quantity evaluated at the position of particle a. This *summation interpolant* is the basis of all SPH schemes. Gradient terms may be easily obtained by taking the analytic derivative of (2.5),

$$\nabla A(\mathbf{r}_a) = \frac{\partial}{\partial \mathbf{r}_a} \int \frac{A(\mathbf{r}_b)}{\rho(\mathbf{r}_b)} W(|\mathbf{r}_a - r_b|, h_a)\rho(\mathbf{r}_b)d\mathbf{r}_j + O(h_a^2), \tag{2.6}$$

$$\approx \sum_b m_b \frac{A_b}{\rho_b} \nabla_a W_{ab}, \tag{2.7}$$

where we have assumed that the gradient is evaluated at another particle b, so we define $\nabla_a \equiv \frac{\partial}{\partial \mathbf{r}_a}$ and $W_{ab} \equiv W(|\mathbf{r}_a - \mathbf{r}_b|, h_a) \sim W(|\mathbf{r}_{ab}|, h_a)$. Note that given a Kernel, these derivative takes the form of $\nabla_a W_{ab} \sim \frac{\mathbf{r}}{|\mathbf{r}|}\partial W_{ab}$ that depends only in the derivatives of the Kernel and the smoothing length, and thus this is independent of any other calculation.

By doing a Taylor expansion and identifying the error terms, one can subtract the first error term, giving

$$\nabla A_a = \sum_b m_b \frac{(A_b - A_a)}{\rho_b} \nabla_a W_{ab}, \tag{2.8}$$

Since the first error term in the Taylor expansion is removed, the interpolation is exact for constant functions and indeed this is obvious from the form of (2.8). For further reading and interesting discussions about error constrains, I refer the reader to Monaghan (2005).

2.2 Building our set of Equations

To build our set of continuous fluid quantities equations, one first needs to define the smoothing kernel introduced in previous section 2.1.1. The most frequently used kernel $W(|\mathbf{r}|, h)$ is the B_2-Spline (Monaghan and Lattanzio, 1985), which can be written as

$$W(x,h) = \frac{8}{\pi h^3} \begin{cases} 1 - 6\left(\frac{x}{h}\right)^2 + 6\left(\frac{x}{h}\right)^3 & 0 \le \frac{x}{h} \le 0.5 \\ 2\left(1 - \frac{x}{h}\right)^3 & 0.5 \le \frac{x}{h} \le 1 \\ 0 & 1 \le \frac{x}{h} \end{cases} \tag{2.9}$$

It is worth stressing that, contrary to other SPH implementation, GADGET uses the notation in which the kernel $W(x,h)$ reaches zero at $x = h$ and not at $x = 2h$. The density ρ_a at each particle position $\mathbf{r}_a$ can be estimated via

$$\langle \rho_a \rangle = \sum_b m_b W(|\mathbf{r}_{ab}|, h_a), \tag{2.10}$$

where the smoothing length h_a found solving iteratively the implicit equation

$$\frac{4\pi}{3}h_a^3\rho_a = Nm_a. \tag{2.11}$$

A typical value for N is in the range of 32-64, which correspond to the number of neighbors which are traditionally chosen in SPH implementations. We need to discretize our set of physical equations in the form 2.3 As an example, we can derive the proper motion equations starting from the Lagrangian (as Price and Monaghan (2004a); Monaghan (2005) already shown)

$$L = \int \left(\frac{1}{2}\rho\mathbf{v}^2 - \rho u\right) \mathrm{dV}, \tag{2.12}$$

where u is the internal energy per unit mass. Again, in SPH form this is re-written in summation form as

$$L = \sum_a m_a \left[\frac{1}{2}\mathbf{v}_a^2 - u_a(\rho_a, s_a)\right], \tag{2.13}$$

where as before we have replaced the volume element ρdV with the mass per SPH particle m. We regard the particle co-ordinates as the canonical variables. Being able to specify all of the terms in the Lagrangian directly in terms of these variables, and taking into account the invariance of the Lagrangian to transformations, the conservation laws will be automatically satisfied. Since the equations of motion result then the Euler-Lagrange equations

$$\frac{d}{dt}\left(\frac{\partial L}{\partial \mathbf{v}_a}\right) - \frac{\partial L}{\partial \mathbf{r}_a} = 0. \tag{2.14}$$

The internal energy is regarded as a function of the particle's density, which in turn is specified as a function of the co-ordinates by (2.10). The terms in (2.14) are therefore given by

$$\frac{\partial L}{\partial \mathbf{v}_a} = m_a\mathbf{v}_a, \tag{2.15}$$

$$\frac{\partial L}{\partial \mathbf{r}_a} = \sum_b m_b \left.\frac{\partial u_b}{\partial \rho_b}\right|_s \frac{\partial \rho_b}{\partial \mathbf{r}_a}. \tag{2.16}$$

From the first law of thermodynamics in the absence of dissipation we have

$$\left.\frac{\partial u_b}{\partial \rho_b}\right|_s = \frac{P_b}{\rho_b^2}, \tag{2.17}$$

and using (2.10) we have

$$\frac{\partial \rho_a}{\partial \mathbf{r}_b} = \sum_c m_c \nabla_a W_{bc} \left(\delta_{ba} - \delta_{ca}\right), \tag{2.18}$$

such that

$$\frac{\partial L}{\partial \mathbf{r}_a} = \sum_b m_b \frac{P_b}{\rho_b^2} \sum_a m_c \nabla_a W_{bc} \left(\delta_{ba} - \delta_{ca}\right), \tag{2.19}$$

$$= m_a \sum_b m_b \left(\frac{P_a}{\rho_a^2} + \frac{P_b}{\rho_b^2}\right) \nabla_a W_{ab}, \tag{2.20}$$

where we have used the fact that the gradient of the kernel is anti-symmetric (i.e. $\nabla_a W_{ab} = -\nabla_a W_{ba}$). The SPH equation of motion in the absence of dissipation is therefore given by

$$\frac{d\mathbf{v}_a}{dt} = -\sum_b m_b \left(\frac{P_a}{\rho_a^2} + \frac{P_b}{\rho_b^2} \right) \nabla_a W_{ab}, \tag{2.21}$$

which can be seen to explicitly conserve momentum since the contribution of the summation to the momentum of particle a is equal and opposite to that given to particle b (given the antisymmetry of the kernel gradient).

In GADGET, the equation 2.21 for the SPH particles are implemented based on this derivation (Springel and Hernquist, 2002) and take the form

$$\left(\frac{\mathrm{d}\mathbf{v}_a}{\mathrm{d}t} \right)_{\mathrm{hyd}} = -\sum_b m_b \left[f_a \frac{P_a}{\rho_a^2} \nabla_a W_a + f_b \frac{P_b}{\rho_b^2} \nabla_a W_b) \right]. \tag{2.22}$$

The coefficients f_a are defined by

$$f_a = \left[1 + \frac{h_a}{3\rho_a} \frac{\partial \rho_a}{\partial h_a} \right]^{-1}, \tag{2.23}$$

and reflect the full, self-consistent correction terms arising from varying the particle smoothing length. The abbreviation stands $W_{a/b} = W(|\mathbf{r}_a - \mathbf{r}_b|, h_{a/b})$ for the two kernels of the interacting particles. The pressure of each particle is given by $P_a = A_a \rho_a^\gamma$, where the entropic function A_a stays constant for each particle in the absence of shocks or other sources of heat.

One of the most interesting aspects of SPH is the lack of any kind of numerical diffusion of the method. This as first thought is an advantage, but in the other hand does not help to regularize instabilities, or properly handle physical sharp discontinuities in the medium. For example to capture shocks properly, artificial viscosity is needed. Therefore, in GADGET the viscous force is implemented as

$$\left(\frac{\mathrm{d}\mathbf{v}_a}{\mathrm{d}t} \right)_{\mathrm{visc}} = -\sum_{b=1}^{N} m_b \Pi_{ab} \nabla_a W_{ab}, \tag{2.24}$$

where $\Pi_{ab} \geq 0$ is non-zero only when particles approach each other in physical space.

In the case of an ideal gas equation of state where

$$P = A(s)\rho^\gamma, \tag{2.25}$$

the entropic function $A(s)$ evolves according to

$$\begin{aligned} \frac{dA}{dt} &= \frac{\gamma - 1}{\rho^{\gamma-1}} \left(\frac{du}{dt} - \frac{P}{\rho^2} \frac{d\rho}{dt} \right), \\ &= \frac{\gamma - 1}{\rho^{\gamma-1}} \left(\frac{du}{dt} \right)_{diss}. \end{aligned} \tag{2.26}$$

This has the advantage of placing strict controls on sources of entropy, since A is constant in the absence of dissipative terms. The thermal energy is evaluated using

$$u = \frac{A}{\gamma - 1} \rho^{\gamma-1}. \tag{2.27}$$

This formulation of the energy equation has been advocated in an SPH context by Springel and Hernquist (2002).

The viscosity generates entropy at a rate

$$\frac{\mathrm{d}A_a}{\mathrm{d}t} = \frac{1}{2}\frac{\gamma-1}{\rho_a^{\gamma-1}}\sum_b m_b \Pi_{ab}\mathbf{v}_{ab}\cdot\nabla_a \bar{W}_{ab}, \tag{2.28}$$

Here, the symbol $\bar{W}_{ab}$ denotes the arithmetic mean of the two kernels W_a and W_b and $\mathbf{v}_{ab}$ denotes the relative velocity between the particles.

For the parametrization of the artificial viscosity we use a formulation proposed by Monaghan (1997) based on an analogy with Riemann solutions of compressible gas dynamics. The resulting viscosity term can be written as

$$\Pi_{ab} = -\frac{\alpha}{2}\frac{v_{ab}^{sig}\mu_{ab}}{\rho_{ab}} \tag{2.29}$$

for $\mathbf{r}_{ab}\cdot\mathbf{v}_{ab} \leq 0$ and $\Pi_{ab} = 0$ otherwise, i.e. the pair-wise viscosity is only non-zero if the particles are approaching each other. Here $\mu_{ab} = \mathbf{v}_{ab}\cdot\mathbf{r}_{ab}/|\mathbf{r}_{ab}|$ is the relative velocity projected onto the separation vector and the signal velocity is estimated as

$$v_{ab}^{\mathrm{sig}} = c_a + c_b - \beta\mu_{ab}, \tag{2.30}$$

with $c_a = \sqrt{\gamma P_a/\rho_a}$ denoting the sound velocity. In GADGET the values $\alpha = 1$ and $\beta = 3$ are commonly used for the dimensionless parameters within the artificial viscosity. Note that in Eq. (2.29) usually a viscosity-limiter is used. In our case this create tensile instabilities between the particles so is discarded.

This also leads naturally to a Courant-like hydrodynamical time-step

$$\Delta t_a^{\mathrm{hyd}} = \frac{C_{\mathrm{Courant}} h_a}{\max_a(v_{ab}^{\mathrm{sig}})}, \tag{2.31}$$

where C_{Courant} is a numerical constant, typically chosen to be in the range $0.15 - 0.2$.

2.2.1 Co-moving variables and units system

The equations of motion are integrated using a leap-frog integration making use of a kick-drift-kick scheme. Within this scheme, all the pre-factors due to the cosmological background expansion are taken into account within the calculation of the kick- and drift-factors (see Quinn et al., 1997; Springel, 2005). For the integration of the entropy within a cosmological simulation, a factor $H^{-1} = \frac{\mathrm{d}t}{\mathrm{d}a}$ is present in all the equations with time derivatives to take into account that the internal time variable in GADGET is the expansion parameter a. The formulation of the MHD equations within GADGET has to be adapted accordingly to this choice of variables.

In GADGET the unit system is defined by setting LENGTH, MASS and VELOCITY factors with respect to the CGS system. Thereby the internal units of ENERGY and TIME are defined. The magnetic field units are defined as GAUSS. Therefore μ_0 within the MHD equations becomes to

$$\mu_0 = \frac{[\mathrm{TIME}]^2[\mathrm{LENGTH}]}{4\pi[\mathrm{MASS}]}. \tag{2.32}$$

For cosmological simulations, the parametrization of the units for LENGTH, MASS and TIME contain the Hubble constant h and therefore μ_0 has to be modified to be

$$\mu_0 = \frac{[\mathrm{TIME}]^2[\mathrm{LENGTH}]}{4\pi[\mathrm{MASS}]h^2}. \tag{2.33}$$

Note that the magnetic field in the code is always physical for historical reasons. This means that all the evolution in cosmological simulations has to take additional the non-comoving terms and factors accordingly.

2.2.2 Magnetic signal velocity

A natural generalization of the signal velocity v_{ab}^{signal} in the framework of MHD is to replace the sound velocity c_a by the fastest magnetic wave as suggested by Price and Monaghan (2004a). Therefore the sound velocity c_a gets replaced by

$$c_a^{mag} = \frac{1}{\sqrt{2}}\sqrt{\left(c_a^2 + \frac{B_a^2}{\mu_0\rho_a}\right) \cdot \sqrt{\left(c_a^2 + \frac{B_a^2}{\mu_0\rho_a}\right)^2 - 4\frac{c_a^2(\mathbf{B}\cdot\hat{\mathbf{r}}_{ab})^2}{\mu_0\rho_a}}} \tag{2.34}$$

As this new definition of the signal velocity also enters the time step criteria (2.31), no extra time-step criteria due to the magnetic field has to be defined. If we choose more conservative settings within the Courant condition, we still see improvements in the solution of the test problems. Therefore we generally use $C_{\mathrm{Courant}} = 0.075$, which is half the value usually used in pure hydrodynamical problems. Different authors also propose to use different values for α and β within the artificial viscosity definition (2.29). Whereas typically $\alpha = 1$ is chosen, Monaghan (1997) proposed to use $\beta = 3$. Price and Monaghan (2004b) propose to use $\beta = 2$ or $\beta = 1$ respectively. We find slight improvements in our test problems when using $\alpha = 2$ and $\beta = 1.5$, which are the values that we use if not noted otherwise.

2.2.3 Induction equation

In appendix A we set the proper equations that ideal MHD should follow, in particular the evolution of the magnetic field is given by the induction equation,

$$\frac{\mathrm{d}\mathbf{B}}{\mathrm{d}t} = (\mathbf{B}\cdot\nabla)\mathbf{v} - \mathbf{B}(\nabla\cdot\mathbf{v}) \tag{2.35}$$

if *Ohmic* dissipation is neglected and the constraint $\nabla\cdot\mathbf{B} = 0$ is used. In a cosmological framework there are additional terms and factors because of the dilution of the space and the fact that magnetic fields behave like fluxes. This equation takes then the form

$$\frac{\mathrm{d}\mathbf{B}(z)}{\mathrm{d}t} = \frac{\mathrm{d}\mathbf{B}}{\mathrm{d}t}\frac{1}{a^2} - 2H(z)\mathbf{B}(z)$$

If we construct the SPH equivalent as described in section 2.1.1, the full induction equation takes the form

$$\frac{\mathrm{d}\mathbf{B}_a}{\mathrm{d}t} = \frac{1}{Ha^2}\frac{f_a}{\rho_a}\cdot\left[\sum_b m_b\left(\mathbf{B}_a(\mathbf{v}_{ab}\cdot\nabla_a W_{ab}) - \mathbf{v}_{ab}(\mathbf{B}_a\cdot\nabla_a W_{ab})\right)\right] - 2\mathbf{B}_a \tag{2.36}$$

where H^{-1} takes into account that the internal time variable in GADGET is the expansion parameter a. Note that here, by construction, only the kernel W_a and its derivative are used. All the cosmological pre factor and terms are only present in the cosmological simulations and absent in the code evaluation presented in section 2.4. In component[5] form the induction equation reads

$$\frac{\mathrm{d}B_a^i}{\mathrm{d}t} = \frac{1}{Ha^2}\frac{f_a}{\rho_a}\left[\sum_b m_b(v_{ab}^i B_a^j - B_a^i v_{ab}^j)\partial W_a \hat{\mathbf{r}}_{ab}^j\right] - 2\mathbf{B}_a^i \tag{2.37}$$

Note that, as also suggested by Price and Monaghan (2004b), we wrote down the equations including the correction factor f_a which reflects the correction terms arising from the variable particle smoothing length. Unfortunately it is not possible to directly infer the exact form of the correction factors from first principles for the induction equation. However, Price and Monaghan (2004b) showed that, if not chosen to be the same as the one used for the Lorenz force, inconsistency between the induction equation and magnetic force results. The effect of these factors in the induction equation is quite small, but nevertheless one notices improvements in test problems when they are included. Therefore, we included them for all applications presented in this work.

2.2.4 Magnetic force

The magnetic field acts on the plasma via the Lorenz force shown in equation. Eq. (A.3), which can be written in a symmetric, conservative form involving the magnetic stress tensor (Phillips and Monaghan, 1985)

$$M_a^{ij} = \left(\mathbf{B}_a^i \mathbf{B}_a^j - \frac{1}{2}|\mathbf{B}_a|^2\delta^{ij}\right). \tag{2.38}$$

The magnetic contribution to the acceleration of the a-th particle can therefore be written as

$$\left(\frac{\mathrm{d}\mathbf{v}_a}{\mathrm{d}t}\right)_{\mathrm{mag}} = \frac{a^{3\gamma}}{\mu_0}\sum_b m_b\left[f_a\frac{M_a}{\rho_a^2}\cdot\nabla_a W_a + f_b\frac{M_b}{\rho_b^2}\cdot\nabla_b W_b\right] \tag{2.39}$$

Where the factor $a^{3\gamma}$ is needed to transform to the internal variables for cosmological simulations and is set to one in all other cases. Also μ_0 has to be chosen properly as described in section 2.2.1. The factors f_a reflect the correction terms as discussed previously. In component form the equation reads

$$\left(\frac{\mathrm{d}\mathbf{v}_a^i}{\mathrm{d}t}\right)_{\mathrm{mag}} = \frac{a^{3\gamma}}{\mu_0}\sum_b m_b\left[f_a\frac{M_a^{ij}}{\rho_a^2}\partial W_a\hat{\mathbf{r}}_{ab}^j + f_b\frac{M_b^{ij}}{\rho_b^2}\partial W_b\hat{\mathbf{r}}_{ab}^j\right] \tag{2.40}$$

The main problem with this formulation is that it becomes unstable for situations in which magnetic forces are dominating (Phillips and Monaghan, 1985). The reason for this is that the magnetic stress can become negative depending on the morphology of the magnetic field lines and the numerical errors in the evolution, leading to the clumping of particles, and thus spurious forces arise. Therefore, some additional measures have to be taken to suppress the onset of this instability.

[5] We denote with i, j, k the different components

2.3 Instability corrections and regularization schemes

There are several methods proposed in the literature to suppress the onset of the clumping instability which is caused by the implementation of the magnetic force. However their performance was found to depend on the details of the simulation setup. Also the requirement to have $\nabla \cdot \mathbf{B}$ close to zero is not only physically motivated but numerical in the sense that large $\nabla \cdot \mathbf{B}$ will perturb the *Lorentz* equation with spurious force. The numerical origin of this errors is simply the coarseness, either in the integration or due to SPH operator, and those evolution is highly non linear and unstable.

Beside theses instabilities, noise (e.g. fluctuations of the magnetic field imprinted by numerical effects when integrating the induction equation) is a source of errors in SPH-MHD implementations. Therefore there are regularization schemes to obtain a magnetic field which does not show strong fluctuations below the smoothing length. This can be achieved indirectly through improvements in the underlying SPH formalism (as the instability corrections work) as well as in reformulation of the interactions to reduce the creation of small irregularities arising from numerical effects. Besides direct smoothing of the magnetic field, there is the possibility to dissipate small irregularities by introducing artificial terms in same way as the artificial viscosity is implemented.

It is important to note that the only nature of dissipation in SPH is that all the values come from the neighboring summation. This effect underlay inside the smoothing length, therefore it is useful to consider this as the "resolution" of our simulation. If one scheme uses smoothed values to infer the primitive ones, then we fall in an additional smooth or dissipative process that is larger than the smoothing length, therefore noticeable in the "resolution" given by it.

We briefly comment on only a couple of possibilities that turn out to be successful in the context of building up an implementation for cosmological simulations.

2.3.1 Improvements in the underlying SPH formalism

The entropy conserving formalism (Springel and Hernquist, 2002) of the underlying SPH implementation contributes to a significant improvement of the MHD formalism compared to previous MHD implementations in SPH by generally improving the density estimate and the calculation of derivatives. It has to be noted, that this is not only due to the $\frac{\mathrm{d}W}{\mathrm{d}h}$ terms, but in large part also from the new formalism for calculating of the smoothing length itself. As described before, the smoothing length h for each particle is no longer calculated by counting neighbors within the sphere, but by solving equation Eq. (2.11) for a predefined number N, there exists only one unambiguous value of h. This equation is solved iteratively and note that there is no restriction on the value of N beside the convergence [6]. It is usual to give some allowed range of N for the equation to converge, however in our case we choose the range smaller than 1 and typically we use $N = 64 \pm 0.1$.

2.3.2 Divergence force subtraction

Børve et al. (2001) suggested explicitly subtracting the effect of any numerically non-vanishing divergence of the magnetic field. Therefore, one can explicitly subtract the

[6] In other implementations N was usually an integer value, without iterative solution.

term as an error, that by definition shouldn't exist

$$\left(\frac{\mathrm{d}\mathbf{v}_a^i}{\mathrm{d}t}\right)_{\mathrm{mag}}^{\mathrm{corr}} = -a^{3\gamma}\frac{1}{\mu_0}\hat{\beta}\sum_b m_b\left[f_a\frac{\mathbf{B}_a}{\rho_a^2}\cdot\nabla_a W_a + f_b\frac{\mathbf{B}_b}{\rho_b^2}\cdot\nabla_b W_b\right] \tag{2.41}$$

from the momentum equation. To be consistent with the other formulations, we included the $\frac{\mathrm{d}W}{\mathrm{d}h}$ terms. The factor $\hat{\beta}$ is introduced in the original work (Børve et al., 2001), to have some control over this correction and a value of $\hat{\beta} = 1$ was chosen.

In principle, this term breaks the momentum conserving form of the MHD formulation. However, in practice, this seems to be a minor effect. In general this correction should be always small, Børve et al. (2004) argued that stability for linear waves in 2D can be safely reached even when not subtracting the full term but choosing $\hat{\beta} < 1$; e.g. they suggested $\hat{\beta} = 0.5$ to further minimizing the non-conservative contribution. However, it is not clear if this stays true for 3D setups and in the non-linear regime. Additionally, Børve et al. (2004) used a higher order kernel and therefore it is also not clear if that is still true in our case.

We noticed, that under certain circumstances, the correction itself can drive instabilities, specially when the amplitude of the correction is not longer small compared with the acting *Lorentz* force.

These problems can be overcome by introducing a numerical limiter. Basically we redefine $\hat{\beta}$ to be particle dependent (i.e. $\hat{\beta}_a$), and constrained by the ratio between the magnitudes of the *Lorentz* force and the correction by the following threshold

$$\hat{\gamma}_a = \frac{\left|\frac{\mathrm{d}\mathbf{v}_a^i}{\mathrm{d}t}_{\mathrm{mag}}\right|}{\left|\frac{\mathrm{d}\mathbf{v}_a^i}{\mathrm{d}t}^{\mathrm{corr}}_{\mathrm{mag}}\right|} \geq 2 \tag{2.42}$$

therefore, if the *Lorentz* force is not at most twice the correction we renormalise the correction to ensure so. We tested the robustness of this parameter showing that is not so sensitive to variations, see appendix B. In general we find that this correction term, even without the threshold, significantly improves all results in our test simulations and effectively suppresses the onset of the clumping instability. It was also already successfully used in previous, cosmological applications (e.g. Dolag et al., 2004a; Rordorf et al., 2004; Dolag et al., 2005a). However, the introduction of the threshold shown to be useful in simulations of colliding galaxies (Kotarba et al., 2010a) and star formation (Bürzle et al., 2010).

2.3.3 Divergence Cleaning: Dedner Method

Dedner et al. (2002) introduced a novel form to control $\nabla\cdot\mathbf{B}$ errors. Their idea is to create a scalar field to follow the numerical $\nabla\cdot\mathbf{B}$ and by these means correct the magnetic field to guarantee a divergence free field. To do so they studied different possible fields and how they should evolve. The resulting evolution implies a *mixed* scheme, that allows to propagate the errors outside the boundary or used region of interest, and damp these effects at the same time. That method is widely used in Eulerian codes and also has been suggested by Price and Monaghan (2005) to be used in SPH.

The first step is to modify the induction equation and adding a term in the form of a scalar field

$$\left(\frac{\mathrm{d}\mathbf{B}_a}{\mathrm{d}t}\right)_{\text{Dedner}} = -\frac{\nabla\phi_a}{Ha} \tag{2.43}$$

The factor $H(z)^{-1}$ takes into account the cosmological derivatives in time and the co-moving coordinates. One should note that for historical reasons in cosmological simulations the units of ϕ are mixed between co-moving and physical [7].

Changes in the energy introduced by this artificial magnetic field in the induction equation should be taken into account in the energy equation.

$$\left(\frac{\mathrm{d}A_a}{dt}\right)_{\text{Dedner}} = -\frac{\gamma-1}{\mu_0\rho_a^{\gamma-1}}\frac{\mathbf{B}_a\cdot(\nabla\phi_a)}{Ha^2} \tag{2.44}$$

Dedner et al. (2002) also show how to construct and evolve this additional field. The evolution equation is given by

$$\frac{\partial\phi_a}{\partial t} = -\left({c_h}^2\nabla\cdot\mathbf{B}_a + \frac{{c_h}^2}{{c_p}^2}\phi_a\right) \tag{2.45}$$

In 2.45 there are two constant values that will determine the evolution of that equation. c_h is related to $\nabla\cdot\mathbf{B}$ as a source term and its wave propagation velocity. c_p is introduced as a damp factor in the evolution. Price and Monaghan (2005) study for the first time the implementation of such correction applied to *Lagrangian* codes. They suggest that it can be useful to, instead of a constant value for c_h, use the maximum signal velocity between particles. In our case it is given by the maximum between the sound velocity and the Alvfén velocity in the media, as described in section 2.2.2. For the damping time or time decay term also they propose to scale it with the signal velocity and the smoothing length as:

$$\begin{aligned} {c_h}^2 &= \sigma(c_a^{mag})^2 \\ \frac{{c_h}^2}{{c_p}^2} &= \frac{\pi c_a^{mag}}{h_a} = \frac{1}{\tau_a} \end{aligned} \tag{2.46}$$

σ and π are dimensionless parameters to be chosen depending on the problem, to balance the source and propagation parts of the evolution. With $\pi = 1.0$ and $\sigma = 1.0$ we recover the best solution in Price and Monaghan (2005). But we study this in detail in section 2.4.

So the total derivative and taking the cosmological dependence one has

$$\begin{aligned} \frac{\mathrm{d}\phi_a}{\mathrm{d}t} &= \frac{1}{a}\frac{\partial\phi_a}{\partial t} - H\phi_a \\ \frac{\mathrm{d}\phi_a}{\mathrm{d}t} &= -\frac{1}{Ha}\left(\pi(c_a^{mag})^2\nabla\cdot\mathbf{B}_a + \frac{\sigma c_a^{mag}}{h}\phi_a\right) - \phi_a \end{aligned}$$

Similar to the $\nabla\cdot\mathbf{B}$ subtraction in the *Lorentz* force, this method has as drawback that the correction can lead to instabilities in the case when the change introduced is larger with the one applied by the induction equation alone.

[7] The actual units of ϕ are $[Velocity][Gauss]$ where the velocity is co-moving and the magnetic field is physical, due our special implementation inside the code.

To avoid this, we also here introduced a numerical limiter $\tilde{\beta}_a$ modifying Eq. (2.43) by

$$\left(\frac{\mathrm{d}\mathbf{B}_a}{\mathrm{d}t}\right)_{\mathrm{Dedner}} = -\tilde{\beta}_a \frac{\nabla\phi_a}{Ha} \tag{2.47}$$

there $\tilde{\beta}_a$ will renormalise the correction to be a fraction Q of the original induction equation in magnitude but allowing the change of the field.

In this case we need to add a new parameter Q that will define at which threshold we renormalise

$$\left|\frac{\nabla\phi_a}{Ha}\right| < Q\left|\frac{\mathrm{d}\mathbf{B}_a}{\mathrm{d}t}\right| \tag{2.48}$$

We study extensively possible constrains of this threshold in addition with the correction itself, but a $Q = 0.5$ seems to be adequate (see apendix B for details). This method successfully regularizes the field locally, which implies that, compared with other methods, it strictly follows the *ideal* MHD equations. This is well studied in section 2.4.

2.3.4 Smoothing the magnetic field

Another method to remove small scale fluctuations and to regularize the magnetic field is to smooth the magnetic field periodically. As suggested by Børve et al. (2001), one can calculate a smoothed magnetic field $\langle\mathbf{B}\rangle$ for each particle,

$$\langle\mathbf{B}_a\rangle = \frac{\sum_b m_b \frac{\mathbf{B}_a}{\rho_b} W_a}{\sum_b m_b \frac{W_a}{\rho_b}}. \tag{2.49}$$

Then, in periodic intervals, one can calculate a new, regularized magnetic field by

$$\mathbf{B}^{\mathrm{new}} = q\,\langle\mathbf{B}\rangle + (1-q)\mathbf{B}. \tag{2.50}$$

Note that this, in principal, acts similar to the mixing process on resolution scale present in Eulerian schemes. However, introduced in this way, the amount of mixing (e.g. dissipation) of magnetic field depends on the frequency with which this procedure is applied and the value of q chosen. Typically, we set q to one and perform the smoothing at every 15^{th}-20^{th} main time-step. It is worth to mention that implemented in this form, total energy is not conserved (as magnetic field fluctuations on scales smaller than the smoothing length are just removed) and, as the time-steps depend on the chosen resolution, this method is even resolution dependent. Never the less it leads to improvements in the results of our test problems, without strongly smoothing sharp features. It also works without problem in 3D and has already been used in cosmological simulations (Dolag et al., 2004a, 2005a).

2.3.5 Artificial magnetic dissipation

Another possibility to regularize the magnetic field was presented by Price and Monaghan (2004b), who suggested including an artificial dissipation for the magnetic field, analogous to the artificial viscosity used in SPH. They suggested that the dissipation terms be constructed based on the magnetic field component perpendicular to the line joining the interacting particles. However, to better suppress the small scale fluctuations within the

magnetic field which appear due to numerical effects especially in multi-dimensional tests, Price and Monaghan (2005) suggested to base the artificial dissipation on the change of the total magnetic field rather than on the perpendicular field components only. We also found this to work significantly better in our test cases and therefore use the latter implementation only. Such an artificial dissipation term can be included in the induction equation as

$$\left(\frac{\mathrm{d}\mathbf{B}_a}{\mathrm{d}t}\right)_{\mathrm{diss}} = \frac{1}{Ha^2}\frac{\rho_a\alpha_B}{2}\sum_b m_b\frac{v_{ab}^{sig}}{\bar{\rho_{ab}}^2}(\mathbf{B}_a-\mathbf{B}_b)\hat{\mathbf{r}}_{ab}\cdot\nabla_a W_a. \tag{2.51}$$

The parameter α_B is used to control the strength of the effect, typical values are suggested to be around $\alpha_B \sim 0.5$. Similar to the artificial viscosity, this will create entropy at the rate

$$\left(\frac{\mathrm{d}A_a}{\mathrm{d}t}\right)_{\mathrm{diss}} = -\frac{\gamma-1}{\rho_i^{\gamma-1}}\frac{\alpha_B}{4\mu_0}\sum_b m_b\frac{v_{ab}^{sig}}{\bar{\rho_{ab}}^2}(\mathbf{B}_a-\mathbf{B}_b)^2\hat{\mathbf{r}}_{ab}\cdot\nabla_a W_a. \tag{2.52}$$

The pre-factor $(\gamma-1)/(\rho_i^{\gamma-1})$ properly converts the dissipation term to a change in entropy.

This method reduces noise significantly. However, depending on the choice of α_B, it can also lead to smearing of sharp features. Additionally, to avoid this outside of strong shocks (e.g. where this is needed), Price and Monaghan (2005) proposed evolving α_B for each particle, similar to the handling of the time dependent viscosity as suggested by Morris and Monaghan (1997). Then, evolution of α_B for each particle will be followed by integrating

$$\frac{\mathrm{d}\alpha_B}{\mathrm{d}t} = -\frac{(\alpha_B-\alpha_B^{\min})}{\tau}+S, \tag{2.53}$$

where the source term S can be chosen as

$$S = S_0\max\left(\frac{|\nabla\times\mathbf{B}|}{\sqrt{\mu_0\rho}},\frac{|\nabla\cdot\mathbf{B}|}{\sqrt{\mu_0\rho}}\right) \tag{2.54}$$

(see Price and Monaghan, 2005). The time-scale τ defines how fast the dissipation constant decays. Taking the signal velocity, one can translate this directly into a distance to the shock over which the dissipation constant decays. A useful choice of τ can be written as

$$\tau = \frac{h}{C\ v^{\mathrm{sig}}}, \tag{2.55}$$

where the constant C typically is chosen to be around 0.2, allowing the dissipation constant to decay within a time that corresponds to the shock travelling 5 kernel lengths (see Price and Monaghan, 2004a),

2.3.6 Euler potential

Besides the implementations to follow the magnetic field evolution using the induction equation 2.35, there are other methods to represent the magnetic fields that implies the use of potential fields (either vector or scalars). Theses methods have the advantage of $\nabla\cdot\mathbf{B}=0$ by construction. However, this constraint is still under the effects of the underlying scheme (i.e. SPH) and other numerical artifacts (i.e. particle noise), that will define the level in which we can sample this condition.

One very elegant way to implement the MHD equations in Lagrangian codes is the usage of so called *Euler* potentials (see Rosswog and Price, 2007, and references therein). They are build as two independent variables α and β and correspond to an implicit choice of a gauge for the *vector potential* [8]. They can be thought of as labels of magnetic field lines and will be advected with the flow. In this formulation, the magnetic field at any time can be represented as

$$\mathbf{B} = \nabla\alpha \times \nabla\beta. \tag{2.56}$$

In principle, having obtained the magnetic field, one could use this magnetic field also in the equation of motion as before. However, this would mean that the magnetic force is based on the second derivative of a variable. This is usually quite noisy and not recommendable unless regularization schemes are implemented for this as well as for example done in Rosswog and Price (2007).

The main drawback of this method is that the final magnetic field in a region of interest usually comes from several field windings. In such situations, the advection of *Euler* potentials with the fluid elements folds improperly the underlaying magnetic field below the resolution, breaking down the scheme, if no re-mapping of the quantities is applied (as implicitly done when follow the induction equation). Therefore, after several "winding-up" times[9], the resulting magnetic field corresponds to the one produced by the stochastic distribution of the potentials due the advection of the fluid.

Rosswog and Price (2007) suggested to evolve the potentials using a similar implementation as the artificial dissipation. We study this possibility and didn't find any improvement in our results. Furthermore, Brandenburg (2010) showed that this kind of implementation is incorrect in the limits of turbulent boxes, showing that the use of an dissipative version of *Euler* potentials will break the gauge with vector potentials, making them unphysical.

Therefore we use this simple description only as a check in cosmological simulations, to investigate the influence of $\nabla \cdot \mathbf{B}$ driven errors, because this implementation should be divergenceless by construction. In such cases the evolution of the magnetic field predicted when using *Euler* potentials can be seen as an upper bound on the amplification processes in lack of back reaction which could lead to saturation effects. Therefore they are a useful tool to check influence of the numerical scheme applied on the results for the cosmological simulations where we have no other means to verify the results. Note that even with this method the $\nabla \cdot \mathbf{B}$ constraint is numerically not fulfilled. As we already mentioned the sampling and the numerical errors due interpolants are always present, this translates to numerical $\nabla \cdot \mathbf{B}$ even if by construction it should be zero. As an example, we found that using the $\nabla \cdot \mathbf{B}$ subtraction method improves our results even with the use of this scheme [10].

2.4 Test problems with stable MHD

The solutions of our astrophysical problems are very complex and non linear. From the original configuration to the final stage, our system will have gone through

[8] Actually what we are representing is just a family of the possible *Vector* potential, therefore not all the possible magnetic field can be represented by the *Euler* potencials.

[9] Time when the magnetic flux had been re-connected in normal cases.

[10] Even it become to be necessary to stabilise the solutions in our studies in star formation (Bürzle et al., 2010), which made us that is the reason why previous studies didn't succeed.

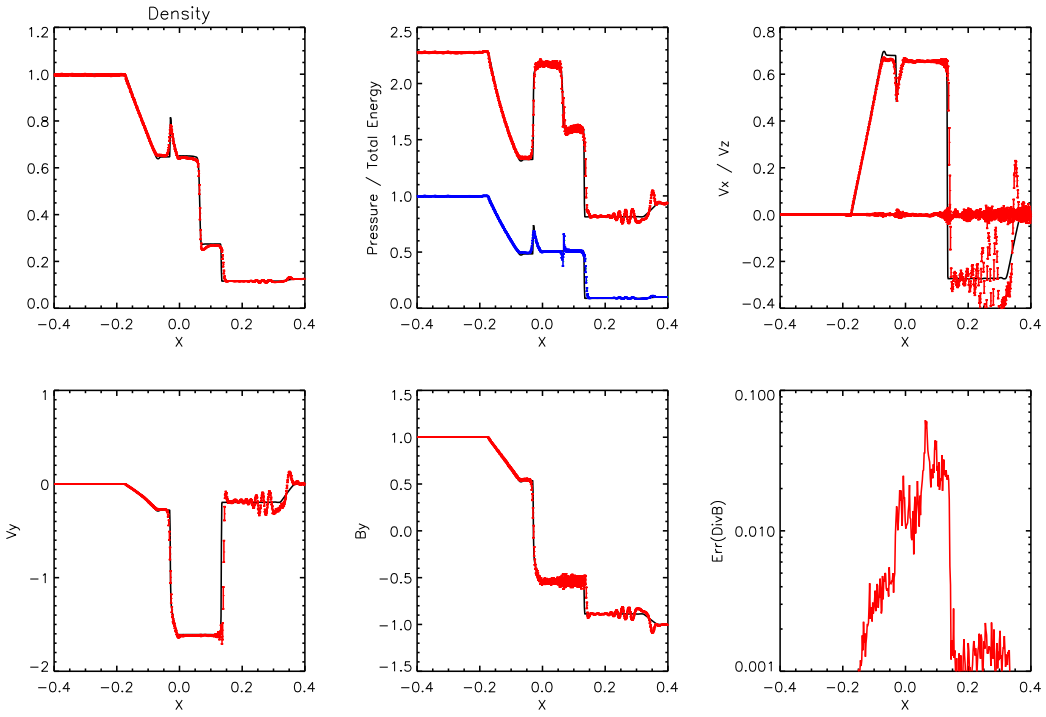

Figure 2.1: Test *5A* at time $t = 7$ with the MHD implementation similar to that used in Dolag et al. (1999, 2002), but already including the instability correction due to subtraction of the $\nabla \cdot \mathbf{B}$ term in the force equation and in a fully three-dimensional setup. Shown in the first row are the density (left panel), total energy and pressure (middle panel) and the x,z component of the velocity field (right panel). The second row shows the y-component in the velocity field (left panel), the three components of the magnetic field (middle panel) and the measure of the $\nabla \cdot \mathbf{B}$ error, see equation Eq. (2.57), in the right panel. The red lines with error bars are show the SPH results and blue just for the pressure case, the black lines are the reference results obtained with ATHENA in a 1D setup.

advection, rarefactions, hydrodynamical, MHD shocks, etc. will happen in different regimes and epochs. To be confident about our results one have to test properly the method used and compare with known solutions. To know the limitations of our implementations we need to know how they perform, and thus even find the optimal numerical parameters for different schemes. Therefore, we performed a series of shock-tube problems as presented by Ryu and Jones (1995). In particular test *5A*, which is also used in Brio and Wu (1988) was used to show the effects of different numerical treatments. Additionally we performed several 2D test cases including the *Fast Rotor* test (Toth, 2000; Londrillo and Del Zanna, 2000; Balsara and Spicer, 1999), a *Strong Blast* (Londrillo and Del Zanna, 2000; Balsara and Spicer, 1999) and the *Orszang-Tang Vortex* (Orszag and Tang, 1979; Dai and Woodward, 1994; Picone and Dahlburg, 1991; Londrillo and Del Zanna, 2000). To obtain results under realistic circumstances, we performed all the tests by setting up a fully three-dimensional particle distribution. Note that three degrees of freedom in each particle are known to arise instabilities, because of the added complexity. There are some regularization methods that show good results in 1/2 dimensions and when tested in 3 dimensions didn't succeed. The astrophysical problems that we want to face have already high complexity and need to be studied in 3

dimensions, therefore we focus directly on this kind of test setups. We also avoid starting from regular grids but used glass-like (White, 1996) initial particle distributions instead. To obtain such a configuration the particles are originally distributed in an random fashion within the volume and then relaxed until they saddle in a equilibrium distribution which is quasi force free and homogeneous in density. This is similar to the distribution of atoms in an amorphous structure like a glass. Compared to a distribution of the particles based on a grid this guarantees that all the kernel averages in the SPH formalism sample the kernel in a uniform way and not several times at the same distances which furthermore are fractions of the underlying grid spacing. For all tests we try to use the same particle masses[11], independent of the initial density. Therefore, typical initial particle distributions for the shock-tube tests where based on 5^3 particles in low density and 10^3 particles in high density regions within unit volume. Usually, these unit volumes are then replicated 35 times along the x-direction each to avoid boundary problems. For some test cases with strong (and therefore fast) shocks, we evolved the simulations longer. In such cases we doubled the simulation setup size in the x-direction.

We assume ideal gas (e.g. $\gamma = 5/3$) and, as described before, use an equivalent of $N = 64$ neighbors for calculating the SPH smoothing length. This ensures that, in the low density regions, SPH particles get smoothed over a region corresponding to a unit length. The number of resolution elements corresponding to a unit length therefore ranges from 1 to 4, depending whether one associates the smoothed region or the mean inter-particle distance with the effective resolution in SPH. In general, SPH converges somewhat slower compared to grid codes when comparing simulations with the same number of grid cells as SPH particles (see section C for an example).

For the SPH results we usually plot the mean within a 3D slab corresponding to the smoothing length and (as error bars) the RMS over the individual particles within this volume. The reference solution was obtained using ATHENA (Stone et al., 2008) with typically 10-20 resolution elements per unit length, depending on the individual test. As one criteria of the goodness of the SPH simulation result we use the usual measure for the non-vanishing divergence of the magnetic field,

$$E_{\nabla\cdot\mathbf{B}} = |\nabla \cdot \mathbf{B}| \frac{h}{|\mathbf{B}|}. \tag{2.57}$$

2.4.1 Brio-Wu shock-tube

The most commonly used MHD shock-tube test is the one studied first time by Brio and Wu (1988) (Test *5A* in Ryu and Jones, 1995, work). This is a good test, because it involves a shock and a rarefaction of the same family moving together. Therefore it allows simultaneous testing of the code in different regimes.

Fig. (2.1) shows the result for a code implementation similar to the first implementation used to study galaxy clusters (e.g. see Dolag et al., 1999, 2002). In addition, the instability correction due to subtraction of the $\nabla \cdot \mathbf{B}$ term was used in the force equation. Various hydrodynamical variables at the final time (e.g. $t = 7$ in this case) are shown. The red lines with error bars show the SPH-MHD result, the black lines are the reference result obtained with ATHENA in a 1D setup (our ideal solution). Shown are (from upper left to

[11] In principle we use exactly the same mass per particle, but in some cases to have the correct density we modify a little bit the masses but less than 1%.

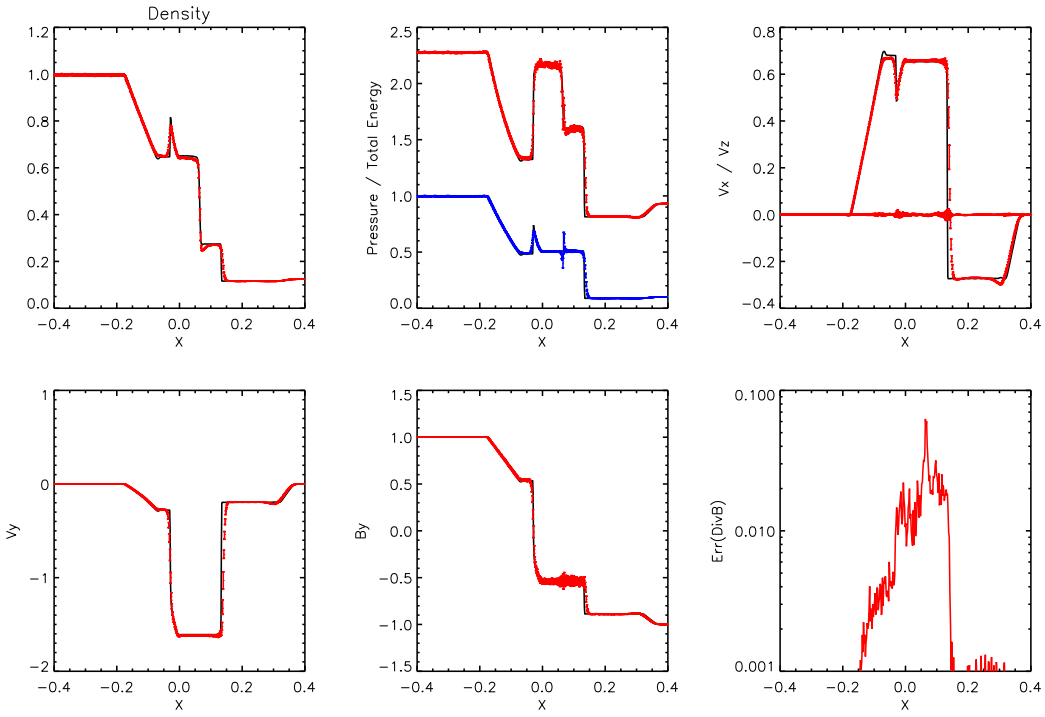

Figure 2.2: As figure Fig. (2.1), but including the magnetic waves in the signal velocity The main advantage are a significant reduction in the noise, specifically in the velocity, but also in the magnetic field. Also the $\nabla \cdot \mathbf{B}$ errors are reduced by a factor of ≈ 2.

the bottom right panel) the density, total energy and pressure, the x- and z-component of the velocity field, the y-component in the velocity field, the three components of the magnetic field and the measure of the $\nabla \cdot \mathbf{B}$ error, obtained from equation (2.57). Note for the SPH pressure is shown in blue to differentiate with the total energy. Here we also switched back to the conventional formulation of the artificial viscosity as for example described in Monaghan (1992), not the one based on signal velocity as used in GADGET. Although the SPH-MHD results in general follow the solution obtained with ATHENA, there is a large scatter in the individual particle values within the 3D volume elements, as well as some instability, especially in the low-density part. Note that although the mean values for the internal energy, as well as the velocity or magnetic field, can locally show some systematic deviations from the ideal solution, the total energy shows much better, nearly unbiased, behaviour. This demonstrates the conservative nature of the symmetric formulations in SPH-MHD.

Noticeable reduction of noise is obtained when using the signal-velocity based artificial viscosity and including the magnetic waves in the calculation of the signal velocity. Therefore, the magnetic waves are directly captured for the time step calculation and in the artificial viscosity, needed to capture shocks. In general, the SPH-MHD implementation gains from the new formulation of SPH, including the $\frac{\mathrm{d}W}{\mathrm{d}h}$ terms and the new way to determine the SPH smoothing length, both contributing to a reduction of noise (and $\nabla \cdot \mathbf{B}$) in the general treatment of hydrodynamics. In figure Fig. (2.2) we include the magnetic waves in the signal velocity. Theses version already has the

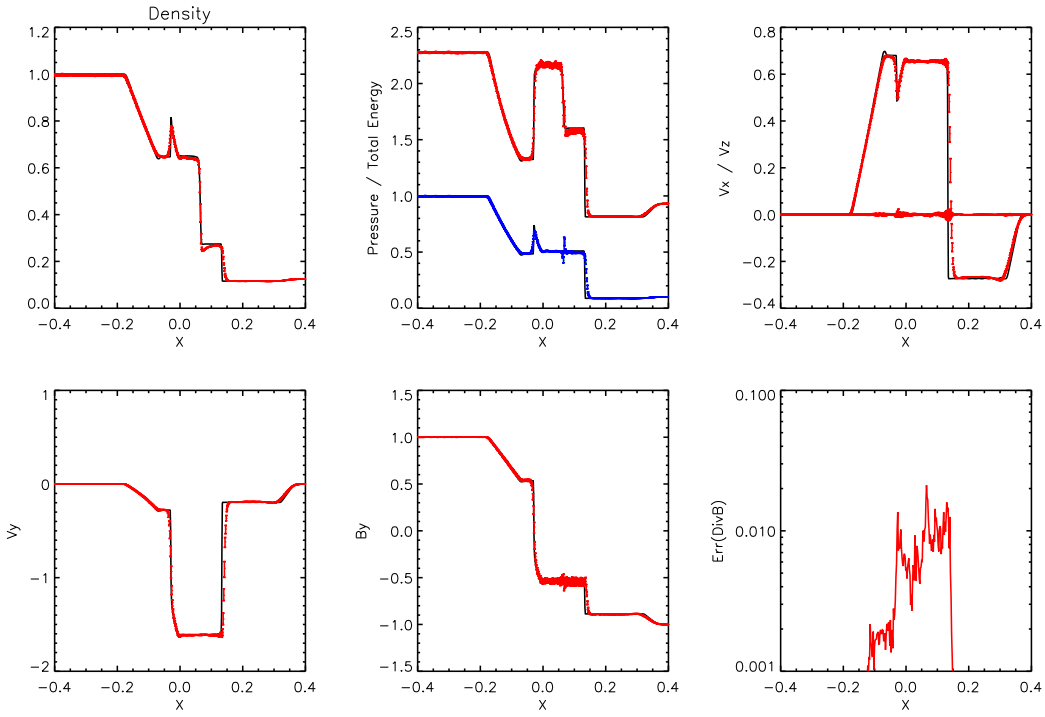

Figure 2.3: As figure Fig. (2.2), but including now the Dedner cleaning scheme. The main advantage that we found is the suppression of the divergence but not features smearing of any kind.

thresholds in the $\nabla \cdot \mathbf{B}$ subtraction [12]. We will refer to this implementation of SPH-MHD as *Standard SPH-MHD* from now on.

In the Fig. (2.3) we can see how the cleaning scheme is working properly with a proper reduction of the $\nabla \cdot \mathbf{B}$ error and lowering the noise. To find the numerical parameters that give best results and increase the stability of the code, we complete a rigorous tests suite performing parameters studies. Theses studies takes into account the quality in terms of noise and accuracy as the proper divergence (see Appendix B). The final parameters range are $\sigma = 2 \sim 5$ and $\pi \sim 1$. The interpretation of these numbers (see Eq. (2.3.3)) are that the $\nabla \cdot \mathbf{B}$ errors propagate at the signal velocity and they will be damped at approximately $2 \sim 5h$.

2.4.2 The effect of field regularization

As described in section (2.3), there are several suggestions for regularization of the magnetic field. We show results obtained by two regularization methods, namely smoothing the magnetic field in regular intervals and including an artificial dissipation. To test theses methods we only use the $\nabla \cdot \mathbf{B}$ subtraction and the magnetic signal velocity for properly stabilize in the *Lorentz* force equation (the *Standard SPH-MHD* runs).

In the smoothing field case, we use the same kernel as used for the normal SPH calculations. In this case, there are two numerical parameters one can choose. One is q in equation (2.50), which quantifies the weight with which the smoothed component

[12] To find the proper numerical parameters we used the same test suit as shown in the next section, the proper studies are shown in Appendix B.

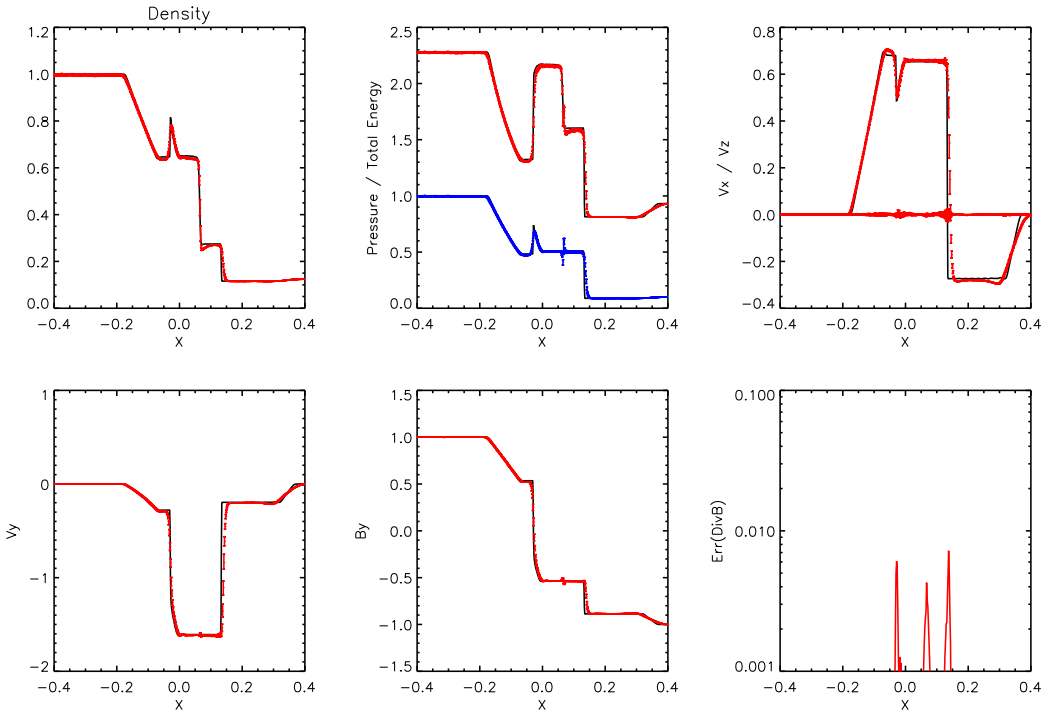

Figure 2.4: As Fig. (2.2), but including the regular smoothing of the magnetic field as a regularization scheme. This SPH-MHD implementation basically reflects the one used in Dolag et al. (2004a, 2005a). The main advantages are a further, significant reduction in the noise as well as a strong reduction of the $\nabla \cdot \mathbf{B}$ errors by a factor of ≈ 10.

enters into the updated magnetic field. We always use $q = 1$ here, which means that we completely replace the magnetic field by the smoothed value. The second is $T_{\rm BS}$, which is the time interval at which the smoothing is done. Here we use a value corresponding to smoothing every 30^{th} global time step. This corresponds to the SPH-MHD implementation used to study the magnetic field in clusters and large scale structure within the local universe(see Dolag et al., 2004a, 2005a). Fig. (2.4) shows the result for the same shock-tube test as before. Clearly, the noise in the individual quantities is strongly reduced. Also the error in $\nabla \cdot \mathbf{B}$ is reduced by more than one order of magnitude. Note that the error bars for the SPH-MHD implementation are of the size of the line width or smaller in most of the cases and therefore no longer clearly visible. However, one can notice some small effect of smearing sharp features. Additionally, some states [13] converge to values which have small but systematic deviations from the exact solution.

The magnetic field can be dissipated in the same way as artificial dissipation works in the hydrodynamics. Here the numerical parameter one has to chose is the strength of this artificial, magnetic dissipation α_B in equation (2.51) and (2.52). Fig. (2.5) shows the result for the same shock-tube test as before using $\alpha_B = 0.1$. Similar to the first method presented, the noise in the individual quantities is strongly reduced and also the error in $\nabla \cdot \mathbf{B}$ is reduced by one order of magnitude. Again, the error bars are smaller than the line width nearly everywhere. Also, some small effects of smearing sharp features are visible

[13] like the region with the negative x-component of the velocity behind the the fast rarefaction wave propagating to the right.

TEST Nr.	Side	ρ	V	B	P
— 1A —	R	1.00	$[10.0, 0.0, 0.0]$	$[5.0, 5.0, 0.0]/(4\pi)^2$	20.0
	L	1.00	$[-10.0, 0.0, 0.0]$	$[5.0, 5.0, 0.0]/(4\pi)^2$	1.00
— 1B —	R	1.00	$[0.0, 0.0, 0.0]$	$[3.0, 5.0, 0.0]/(4\pi)^2$	1.0
	L	0.10	$[0.0, 0.0, 0.0]$	$[3.0, 2.0, 0.0]/(4\pi)^2$	10.0
— 2A —	R	1.08	$[1.2, 0.01, 0.5]$	$[2.0, 3.6, 2.0]/(4\pi)^2$	0.95
	L	1.000	$[0.0, 0.0, 0.0]$	$[2.0, 4.0, 2.0]/(4\pi)^2$	1.00
— 2B —	R	1.00	$[0.0, 0.0, 0.0]$	$[3.0, 6.0, 0.0]/(4\pi)^2$	1.0
	L	0.100	$[0.0, 2.0, 1.0]$	$[3.0, 1.0, 0.0]/(4\pi)^2$	10.0
— 3A —	R	1.00	$[50.0, 0.0, 0.0]$	$-[0.0, 1.0, 2.0]/(4\pi)^2$	0.4
	L	0.100	$[0.0, 0.0, 0.0]$	$[0.0, 1.0, 2.0]/(4\pi)^2$	0.20
— 3B —	R	0.10	$[-1.0, 0.0, 0.0]$	$[0.0, 1.0, 0.0]$	1.0
	L	1.000	$[1.0, 0.0, 0.0]$	$[0.0, 1.0, 0.0]$	1.00
— 4A —	R	1.00	$[0.00, 0.0, 0.0]$	$[1.0, 1.0, 0.0]$	1.0
	L	0.200	$[0.0, 0.0, 0.0]$	$[1.0, 0.0, 0.0]$	0.10
— 4B —	R	0.40	$[-0.669, 0.986, 0.0]$	$[1.3, 0.0025293, 0.0]$	0.5247
	L	1.000	$[0.0, 0.0, 0.0]$	$[1.3, 1.0, 0.0]$	1.00
— 4C —	R	0.65	$[0.667, -0.257, 0.0]$	$[0.75, 0.55, 0.0]$	0.50
	L	1.000	$[0.4, -0.94, 0.0]$	$[0.75, 0.00001, 0.0]$	0.75
— 4D —	R	1.00	$[0.0, 0.0, 0.0]$	$[7.0, 0.001, 0.0]$	1.0
	L	0.300	$[0.0, 0.0, 0.0]$	$[7.0, 1.0, 0.0]$	0.20
— Brio Wu —	R	1.00	$[0.0, 0.0, 0.0]$	$[0.75, 1.0, 0.0]$	1.0
	L	0.125	$[0.0, 0.0, 0.0]$	$[0.75, -1.0, 0.0]$	0.10

Table 2.1: Summary table with the initial conditions of the left and right side of the shock tubes.

as well as some small but systematic deviations from the exact solution. In general, this method works slightly better than the smoothing of the magnetic field, but the differences are generally small.

One idea to reduce the unwanted side effects of such regularization schemes (Price and Monaghan, 2005) is based on a modification of the artificial, magnetic dissipation constant α_B. Therefore every particle evolves its own numerical constant, so that this value can decay where it is not needed and therefore the effects of the artificial dissipation are suppressed. Fig. (2.6) shows the same test as before, but this time where α_B evolves for each particle, as shown in the lower right panel. Clearly, the values are strongly reduced outside the regions associated with sharp features (e.g. shocks), but the effect of smearing sharp features and the small offset of some states are not significantly reduced. This is because in the region in which these side effects originate, the dissipation is still working with its maximum numerical value. On the other hand, due to the suppression of the artificial magnetic dissipation constant outside the shock region, the regularization after the shock passes is nearly switched off. Therefore it does not longer work as efficient as before in the post shock region, visible as increase in the $\nabla \cdot \mathbf{B}$ error compare to the run with a constant, artificial magnetic dissipation.

2.4.3 Shock tube problems

As it can be seen in figures (2.4),(2.5) and (2.3), the side effects of smoothing features by the different regularization methods depend on the details of the underlying structure of the shock-tube test. Even more interesting, the states where one can see small deviations

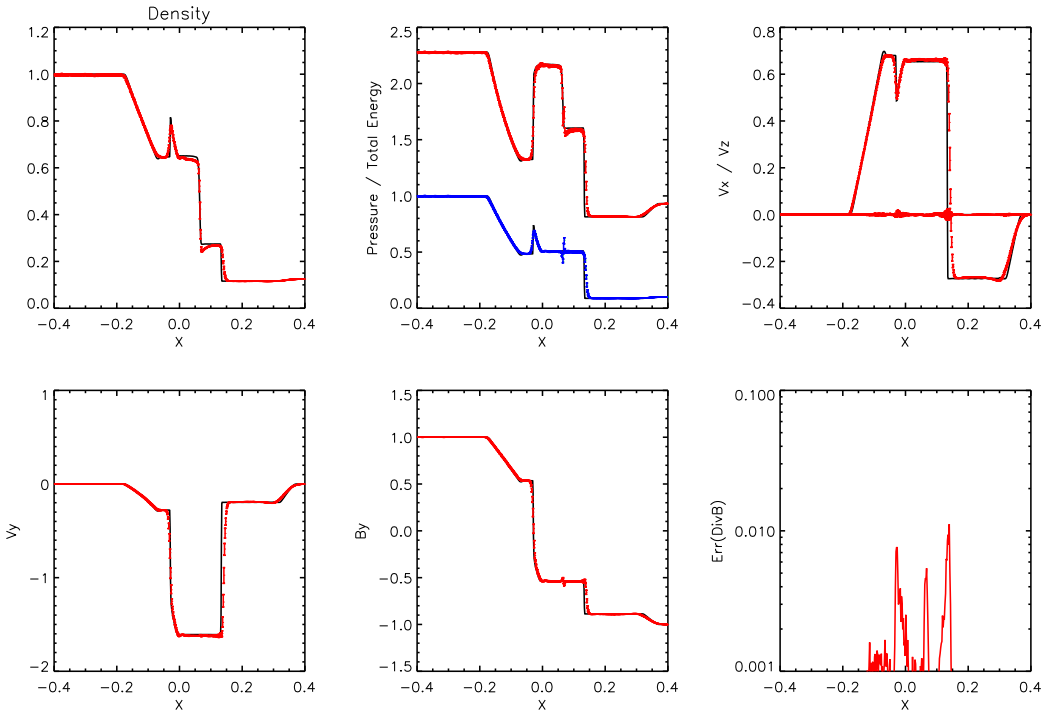

Figure 2.5: As Fig. (2.2), but including artificial magnetic dissipation as a regularization scheme. Similar to the smoothing of the magnetic field, significant reduction in the noise as well as a strong reduction of the $\nabla \cdot \mathbf{B}$ errors by a factor of ≈ 10 is obtained compared to the *basic SPH-MHD* implementation.

from the ideal solution are different for the different regularization methods. Therefore we performed the full set of different shock-tube tests as presented in Ryu and Jones (1995) to test the overall performance of the different implementations under different circumstances. The four test families deal with different complexities of velocity and magnetic field structures, leading to different kinds of waves propagating. A summary of the results of these tests can be found in Fig. (2.7). Plotted are the total energy (left panels), the velocity along the x-direction (middle panels) and the magnetic field along the y-direction (right panels). The red lines reflect the ideal solution obtained with ATHENA, the black lines with error bars mark the results from the SPH-MHD implementation using the magnetic field smoothing every 30^{th} main time step. Note that the error bars in most cases are smaller than the line width. The initial setups for the shock-tube tests can be found in table 2.1, which lists the state vector of the left and right states for the different shock tube tests.

The first family of tests (*1A/1B*) has no structure in the tangential direction of the propagating shocks in magnetic field and velocity, e.g. $B_z = v_z = 0$. As we expect, in the *1A* test, the strong shock (large jump in v_x) leads to some visible noise in the magnetic field component B_y, also translating into significant noise in the total energy. The regularization method here suppresses the formation of the intermediate state in B_y in the SPH-MHD implementation, as can be seen in figure 2.7(a). The second case, the *1B* test, the weak shock is captured well. Again in some regions some smearing of sharp features due to the regularization method is clearly visible.

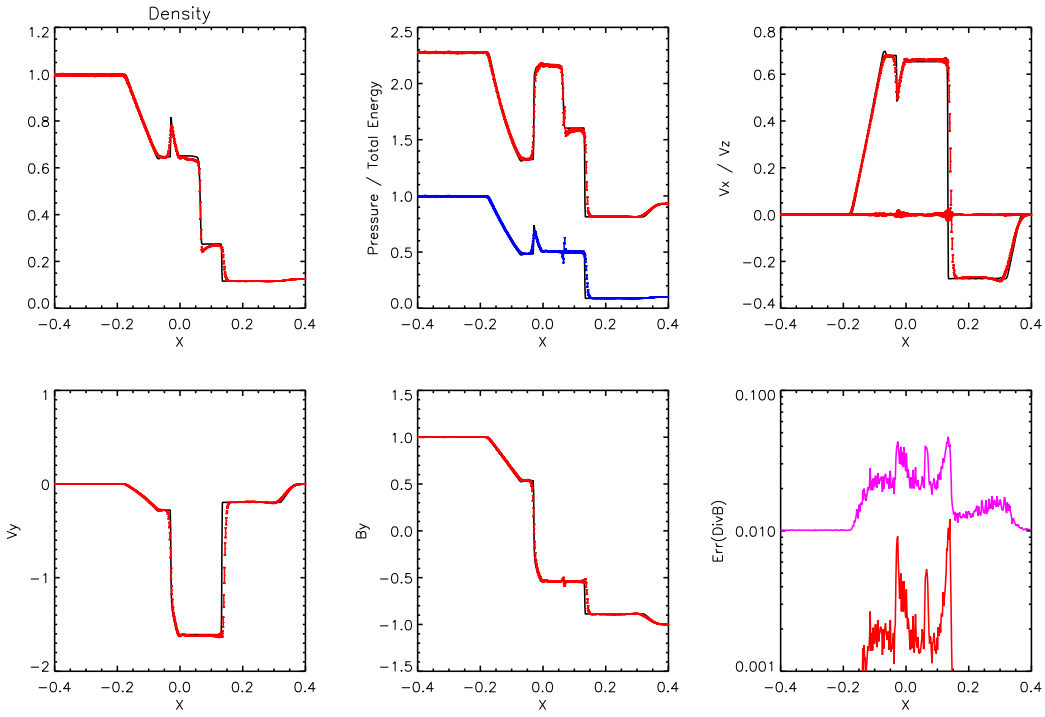

Figure 2.6: As Fig. (2.2), but including time dependent artificial magnetic dissipation as a regularization scheme. No significance improvement is obtained. Note that here in the lower right panel the artificial dissipation constant (α_B) is shown. The effect of suppressing the dissipation is clearly visible, and the maximum value is only reached in peaks associated with the region of strong shocks. However the improvement in the smearing of sharp features is not very significant.

The second class of shocks (*2A/2B*) involve three dimensional velocity structures, where the plane of the magnetic field rotates. All features (e.g. fast/slow shocks, rotational discontinuity and fast/slow rarefaction wave, for details see Ryu and Jones (1995)), are well captured, see figure 2.7(c) and 2.7(d). Some of the features are clearly smoothed by the regularization method.

The third class of tests (*3A/3B*) shows handling of magnetosonic structures. The first has a pair of magnetosonic shocks with zero parallel field and the second are magneto sonic rarefactions. Although there is slightly more noise present, all states are captured extremely well, except the numerical feature left at the position dividing the two states initially, see figure 2.7(e) and 2.7(f).

The fourth test family (*4A/4B/4C/4D*) deals with the so-called switch-on and switch-off structures. The tangential magnetic field turns on in the region behind switch-on fast shocks and switch-on slow rarefaction. Conversely, in the switch-off slow shocks and switch-off fast rarefaction the tangential magnetic field turns off. Again, all structures are captured well with the exception of one feature in figure 2.7(h) as well and maybe 2.7(j) too, where clearly the regularization leads to the washing out of a state. Otherwise the regularization leads to smoothing of some structures similar to the tests presented before.

In general, figure 2.7 demonstrates that all these different situations have to be included when trying to measure the performance and quality of different implementations of regularization methods. The utility of the amount of tests comes when we make a

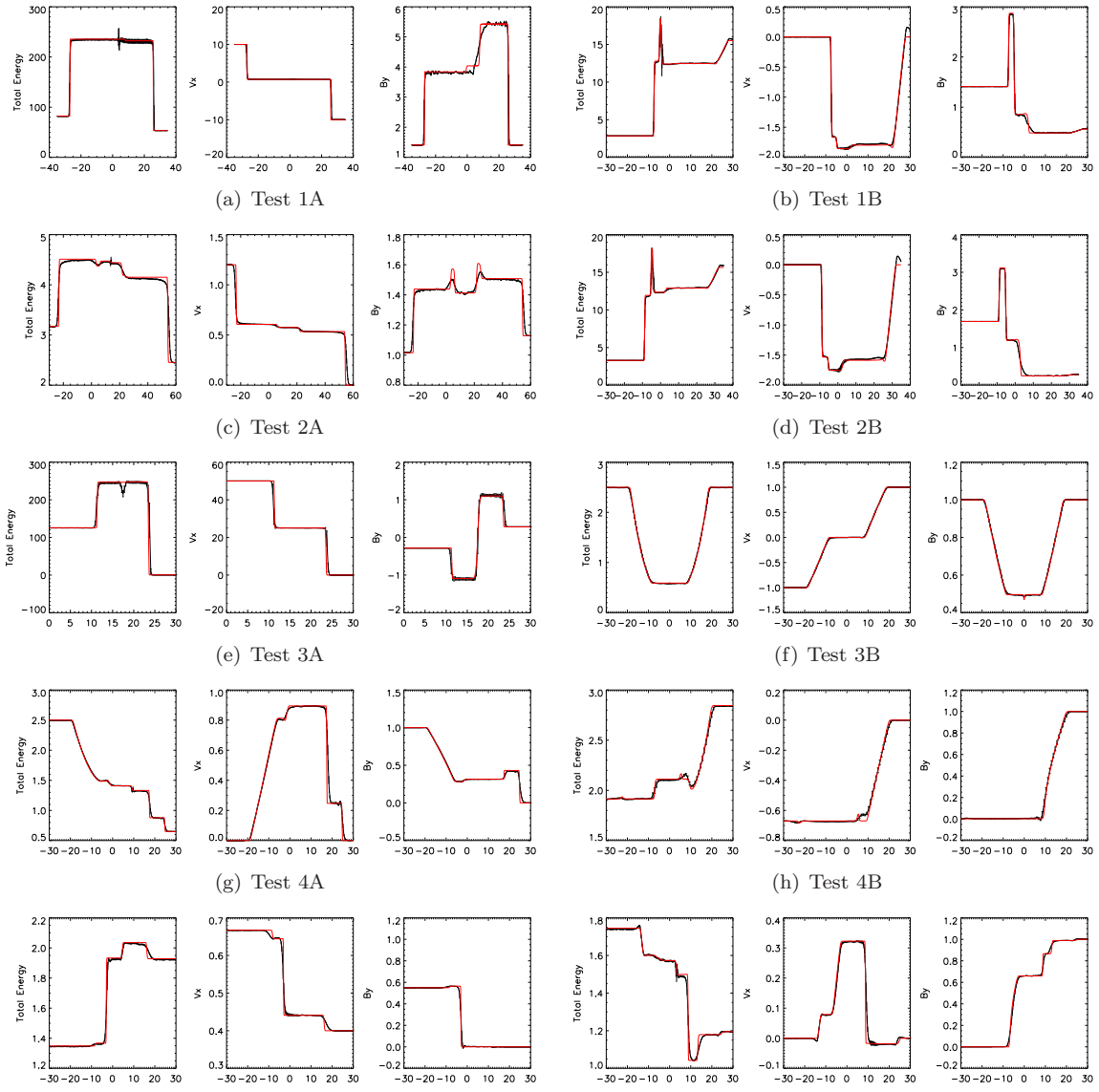

(a) Test 1A (b) Test 1B

(c) Test 2A (d) Test 2B

(e) Test 3A (f) Test 3B

(g) Test 4A (h) Test 4B

(i) Test 4C (j) Test 4D

Figure 2.7: Representative plots of the additional 10 shock-tube tests from Ryu and Jones (1995). Shown for each test are the total energy (left panels), the velocity along the x-direction (middle panels) and the magnetic field along the y-direction (right panels).

parameter study of our implementations described in section 2.3. When doing that one can see how the implementations stress some features with some tests and are almost indifferent to others, allowing to find the optimal numerical parameters as shown in appendix B.

2.4.4 Multi dimensional Tests - Planar Tests

Besides the one dimensional shock tube test described in the previous section, two dimensional (e.g. planar) test problems are a good test-bed to check code performance. Such higher dimensional tests include additional interaction between the evolving

components with non-trivial solution. These can be quite complex (with several classes of waves propagating in several directions) such as the *Orszang-Tang* Vortex or simple (but with strong MHD discontinuities) such as Strong Blast or Fast Rotor.

Fast Rotor

This test problem was introduced by Balsara and Spicer (1999), to study star formation scenarios, in particular the strong torsional Alfvén waves and is also commonly used to validate MHD implementations (for example see Toth, 2000; Londrillo and Del Zanna, 2000; Price and Monaghan, 2005; Børve et al., 2006). The test consists of a fast rotating dense disk embedded in a low density, static and uniform media, with a initial constant magnetic field along the x-direction (e.g. $B_x = 2.5\pi^{-1/2}$). In the initial conditions, the disk with radius $r = 0.1$, density $\rho = 10$ and pressure $P = 1$ is spinning with an angular velocity $\omega = 20$. It is embedded in a uniform background with $\rho = P = 1$. Again we setup the initial conditions by distributing the particles on a glass like distribution in 3D, using $700 \times 700 \times 5$ particles and periodic boundaries in all directions for the background particles. The disk is created by removing all particles which fall inside the radius of the disk and replacing this space with a denser representation of particles of the same mass (mimicking realistic numerical conditions used in cosmological simulations). As an ideal solution to compare with, we again used the result of a simple, two dimensional ATHENA run with 400×400 cells. The solutions for the different implementations and the comparison with ATHENA are shown in Fig. (2.8). The shape, positions and amplitudes correspond quite well, although the GADGET runs appears slightly more smoothed, which is more evident in the cases of dissipation (panel 2.8(c)) and B-field smoothing (panel 2.8(e)).

Fig. (2.9) presents a more quantitative comparison. Shown is a diagonal cut through the *Fast Rotor* at $t = 0.1$ showing the density. The different lines show the results obtained with ATHENA (black line) and for the implementations in GADGET, in blue the standard and in red the artificial dissipation. Very small errors are reflected by the absence of wiggles of those values. Note that our case the simulation is done fully in 3D, whereas the ATHENA solution is two dimensional. The results show remarkable agreement between the two simulations and also compare well with results quoted in the literature (e.g. Londrillo and Del Zanna, 2000).

Note that although we perform our calculations in three dimensions and without a regularization scheme, the implementation produce a result, which has the same quality as other schemes in two dimensions with regularization (e.g. Price and Monaghan, 2005; Børve et al., 2006).

Strong Blast

The *Strong Blast* test consists of the explosion of a circular hot gas in a static magnetized medium and is also regularly used for MHD code validation (see for example Londrillo and Del Zanna, 2000; Balsara and Spicer, 1999). The initial conditions consist of a constant density $\rho = 1$ where a hot disk of radius $r_0 = 0.125$ is embedded, which is hundred times over-pressured, e.g. the pressure in the disk is set to $P_d = 100$ whereas the pressure outside the disk is set to $P_0 = 1$. Additionally there is initially an overall homogeneous magnetic field in the x-direction, with a strength of $B_x = 10$. The system

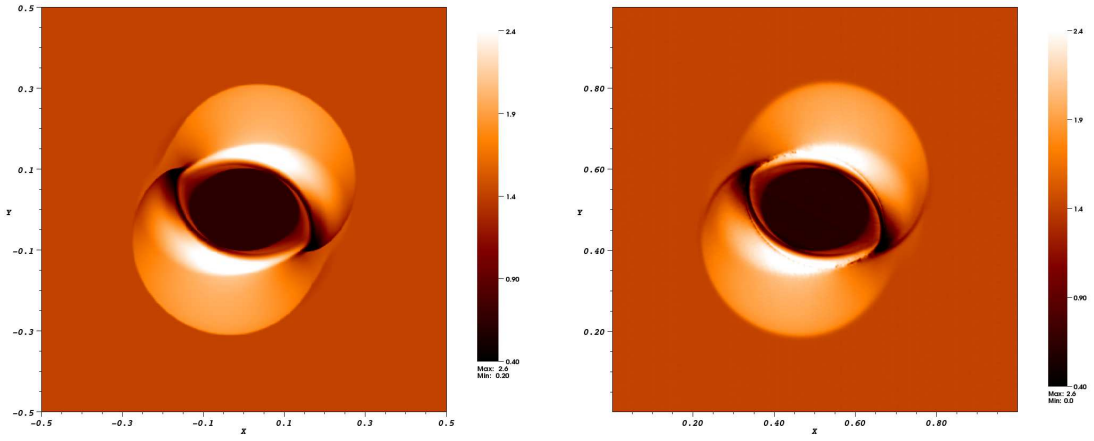

(a) *Fast Rotor* - ATHENA

(b) *Fast Rotor* - Standard

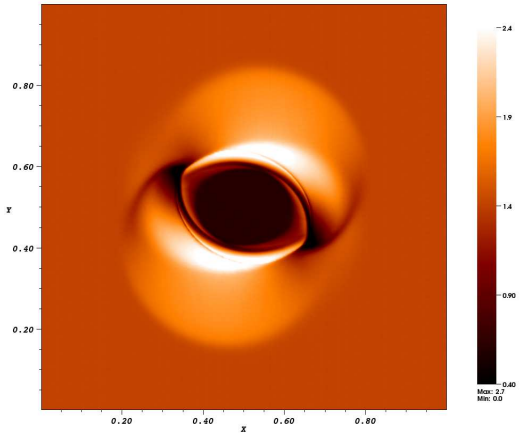

(c) *Fast Rotor* - Dissipation

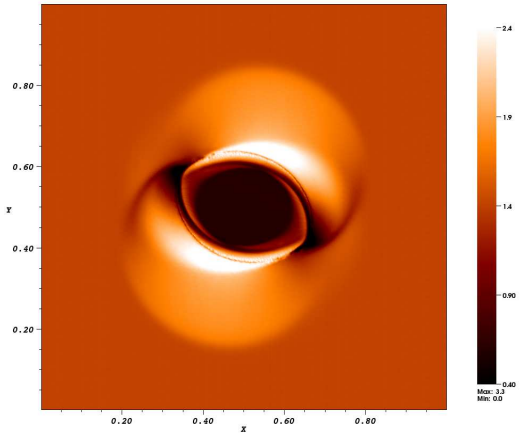

(d) *Fast Rotor* - *Dedner*

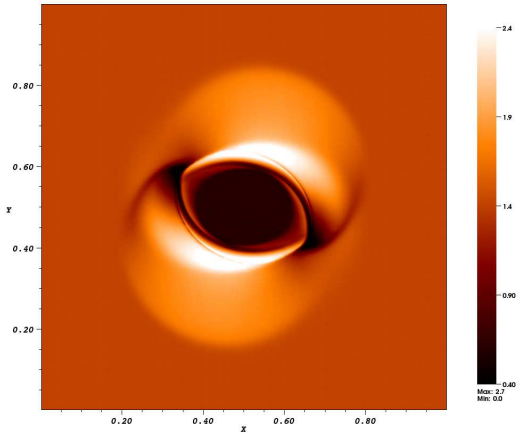

(e) *Fast Rotor* - B-field Smoothing

Figure 2.8: The magnetic field strength in the *Fast Rotor* test at $t = 0.1$. The ATHENA solution of the test problem is shown in the panel 2.8(a) whereas the other panel show the result obtained with the different schemes in GADGET. All the main features are reproduced in the GADGET runs. The shape, positions and amplitudes correspond quite well, although the GADGET run appears slightly more smoothed, which is more evident in the cases of dissipation (panel 2.8(c)) and B-field smoothing (panel 2.8(e)), see also Fig. (2.9).

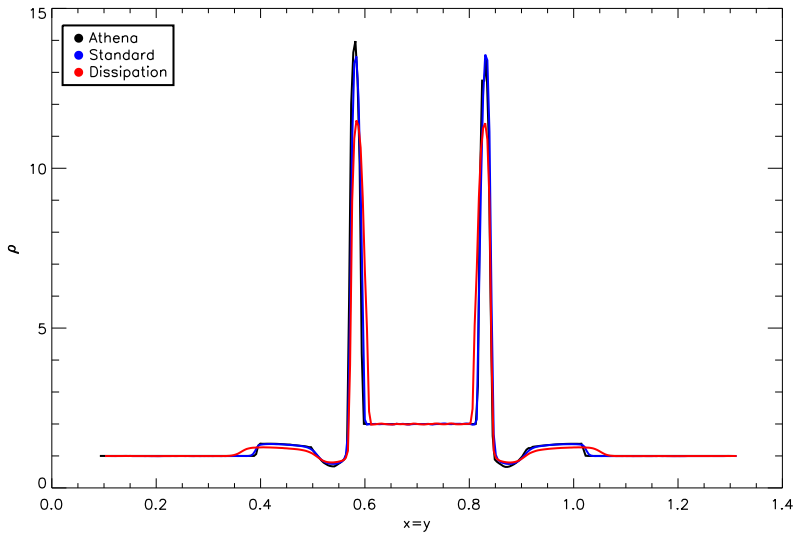

Figure 2.9: Cut through the diagonal ($x = y$) of *Fast Rotor* at $t = 0.1$ showing the density. In black result obtained with ATHENA. The blue line show the GADGET solution using the *standard SPH-MHD* implementation. The red line show the solution using the artificial dissipation scheme. In general, the *standard SPH-MHD* result shows an excellent agreement in all the features, however the dissipation run shown a visible over-smoothing at the outer edges and lower values at the peaks.

is evolved until time $t = 0.02$ and an outgoing shock wave is visible which, due to the presence of the magnetic field, is no longer circular but propagates preferentially along the field lines. Fig. (2.10) shows the density at the final time, comparing the ATHENA results with the ones from the different schemes in GADGET. Although the setup is a strong blast wave, there is no visible difference between the SPH-MHD implementations and the ATHENA results. This is quantitatively confirmed in Fig. (2.11) which shows a horizontal cut (at $y = 0.5$) of the density through the *Strong Blast* test, comparing the ATHENA (black line) with the GADGET results. In blue we show the standard SPH-MHD, in red the artificial dissipation and in green the *Dedner* scheme. Besides very small variations there is no significant difference between the two results and all features are well reproduced by the SPH-MHD implementation. Note that the errors of the GADGET results again are in all cases smaller than the shown line width.

Orszang-Tang Vortex

This planar test problem, introduced by Orszag and Tang (1979), is well known to study the interaction between several classes of shock waves (at different velocities) and the transition to MHD turbulence. Also, this test is commonly used to validate MHD implementations (for example see Dai and Woodward, 1994; Picone and Dahlburg, 1991; Londrillo and Del Zanna, 2000; Price and Monaghan, 2005; Børve et al., 2006). The initial conditions for an ideal gas with $\gamma = 5/3$ are constructed within a unit-length domain (e.g. $x = [0, 1], y = [0, 1]$) with periodic boundary conditions. The velocity field is defined by $v_x = -\sin(2\pi y)$ and $v_y = \sin(2\pi x)$. The initial magnetic field is set to be $B_x = B_0 v_x$ and $B_y = B_0 sin(4\pi x)$. The initial density is $\rho = \gamma P$ and the pressure is set to $P = \gamma B_0^2$. This system is evolved until $t = 0.5$. Fig. (2.12) shows the final

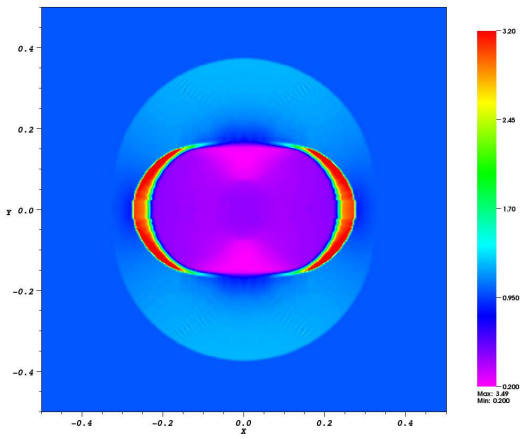

(a) *Strong Blast* - ATHENA

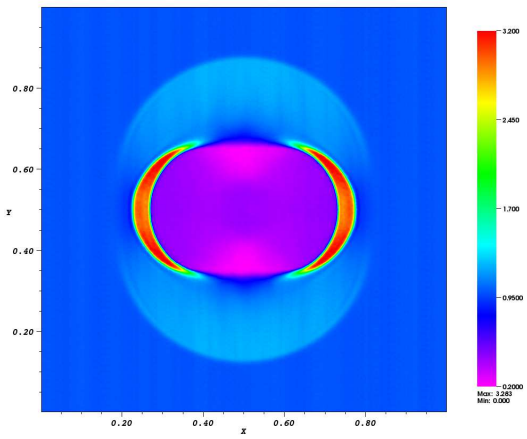

(b) *Strong Blast* - Standard

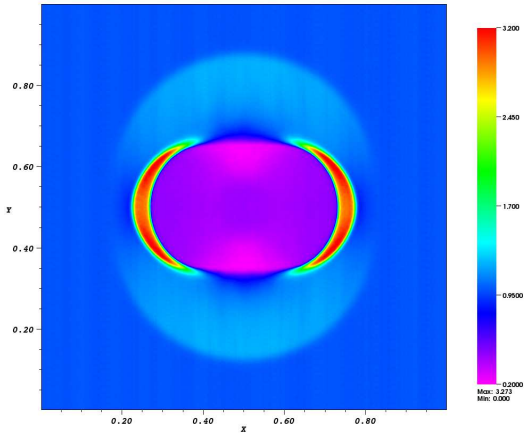

(c) *Strong Blast* - Dissipation

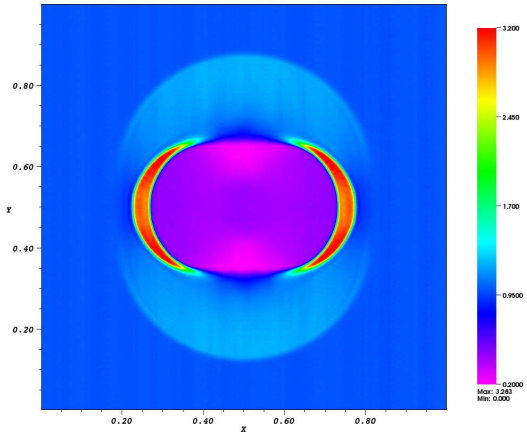

(d) *Strong Blast* - *Dedner*

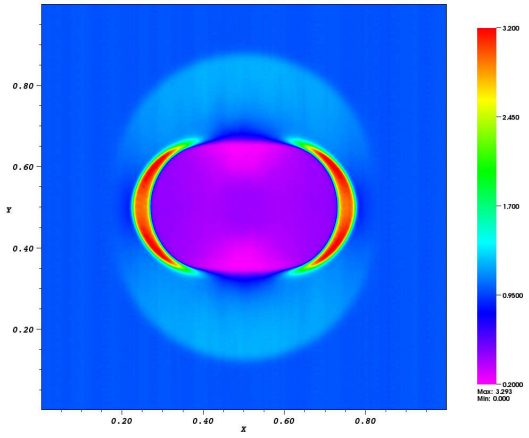

(e) *Strong Blast* - B-field smoothing

Figure 2.10: Shown is the resulting density distribution for the *Strong Blast* test at $t = 0.02$. The panel 2.10(a) shows the results obtained with ATHENA, the results obtained with the different implementations in GADGET are shown in the rest of the plots. There is no visible difference between the different schemes, however we note slight smooth in sharp features compared with the ATHENA solution (see also Fig. 2.11).

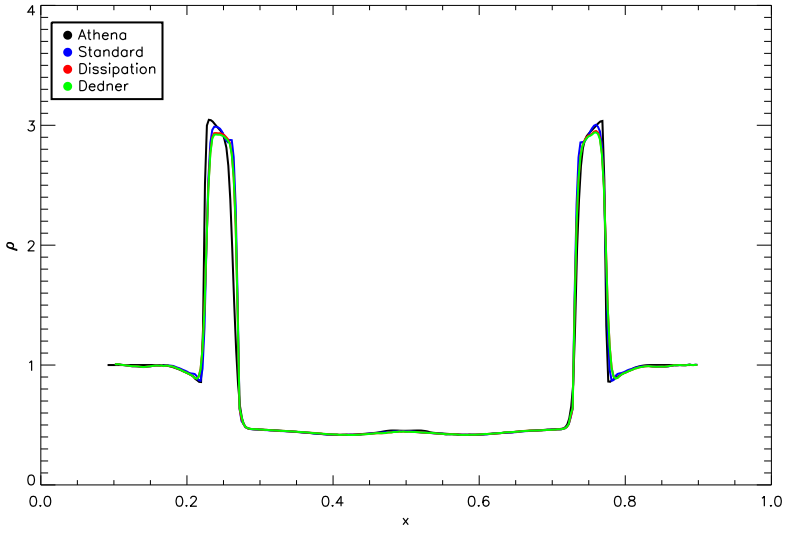

Figure 2.11: Horizontal cut through the *Strong Blast* test ($x = [0.0; 1.0], y = 0.5$) showing the density. The black line is from the ATHENA simulation, the blue line reflects the *standard*, the red one the artificial dissipation and in green we show the *Dedner* implementation. The overall behavior is excellent, with only very small differences between the solutions in the sharp edges.

result for the magnetic pressure for the ATHENA run, in panel 2.12(a), and the different implementations in GADGET, including the *Euler* case, in panel 2.12(f). Visually the results are quite comparable, however the GADGET results look slightly more smeared, which is the imprint of the underlying SPH method. This impression is confirmed in figure Fig. (2.13), which shows a cut through the simulations, made to be comparable with other cuts done in the literature (Børve et al., 2006). In this case, the black line shows the ATHENA result, in blue in the standard, in red the artificial dissipation, in green the *Dedner* and in pink the *Euler* potential representation. In general there is a reasonable agreement, however all the SPH-MHD results clearly show a smoothing of some features. However, the *Dedner* and standard implementations, tends to match better some regions that the dissipative schemes over-smooth (e.g. region near $x \sim 1$ in Fig. 2.13), even better that the *Euler* scheme. A proper comparison is difficult, mainly because this test includes the propagation of several types of magneto sonic waves, this implies that if one miss the correct velocity (i.e. by some dissipative effect) of a particular wave, the result will diverge between implementations. This is shown even by the Eulerian schemes, when we compare the solutions from the AMR code RAMSES and ATHENA in different resolutions and there is no complete convergence with the solution.

The adaptive nature of the SPH-MHD implementation allows the central density peak to be resolved whereas in ATHENA is can only be resolved by increasing the number of grid cells. Never-the-less the SPH-MHD implementation seems to converge slower when increasing the resolution (see Appendix C).

Note that this test, because of their characteristic periodicity, is the one that we use the check the *Euler* potentials formalism. We found a perfect agreement with other authors (i.e. Rosswog and Price, 2007). Our major interest in this scheme is the possibility to measure the errors that arise from the interpolation itself or the coarseness of our initial

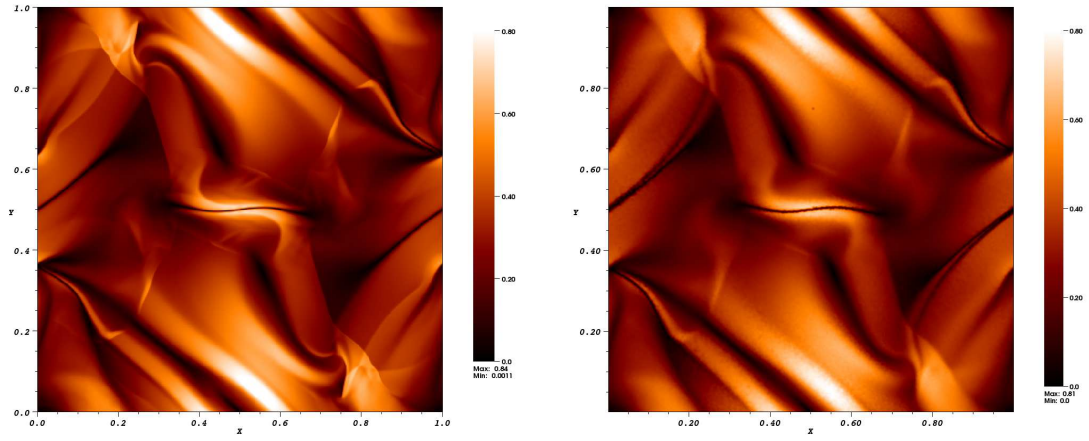

(a) *Orszang-Tang Vortex*- ATHENA

(b) *Orszang-Tang Vortex*- Standard

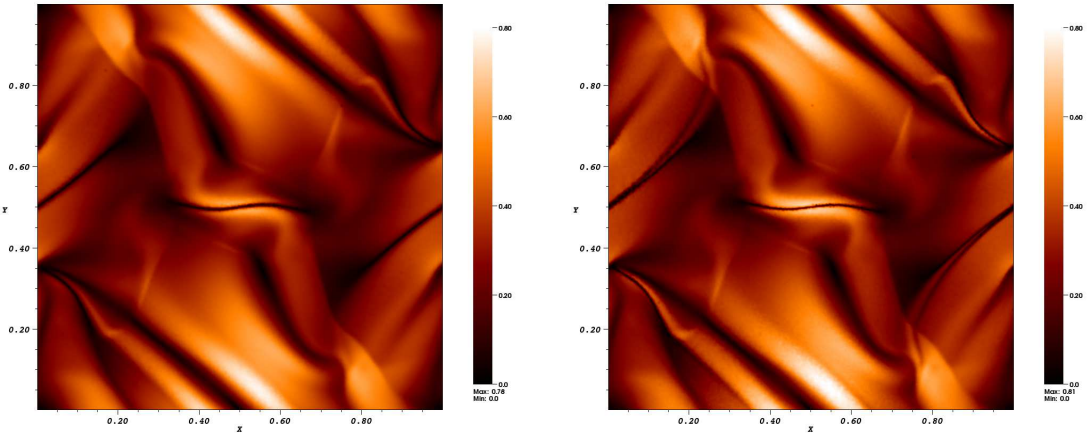

(c) *Orszang-Tang Vortex*- Dissipation

(d) *Orszang-Tang Vortex- Dedner*

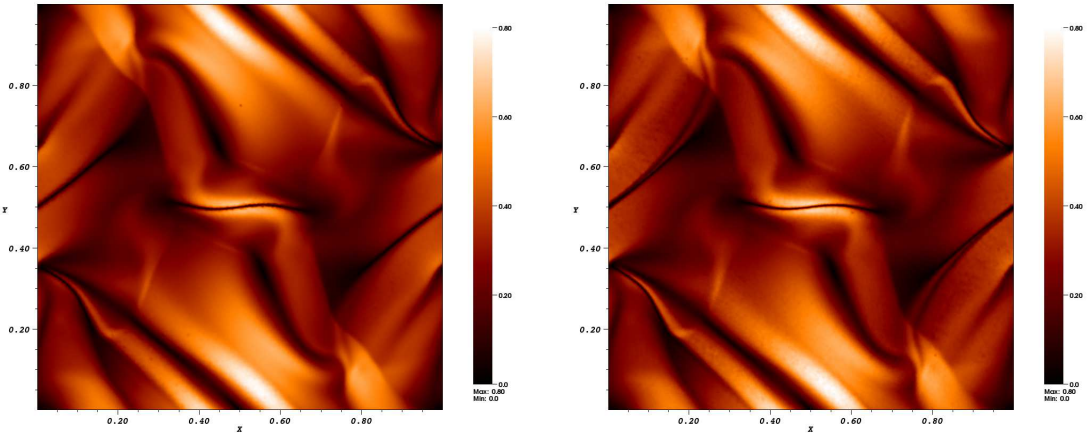

(e) *Orszang-Tang Vortex*- B-field smoothing

(f) *Orszang-Tang Vortex- Euler* scheme

Figure 2.12: The magnetic field strength of the *Orszang-Tang Vortex* at $t = 0.5$. The panel 2.12(a) shows the ATHENA solution and other panels show the different implementation in GADGET. In the panel 2.12(f) we shown the solution from the *Euler* scheme. Some of the sharp features are smoothed in all the SPH-MHD implementations but overall the results compares very well (see also Fig. 2.13). Interestingly some reconnection features are better captured in the SPH cases (see appendix C).

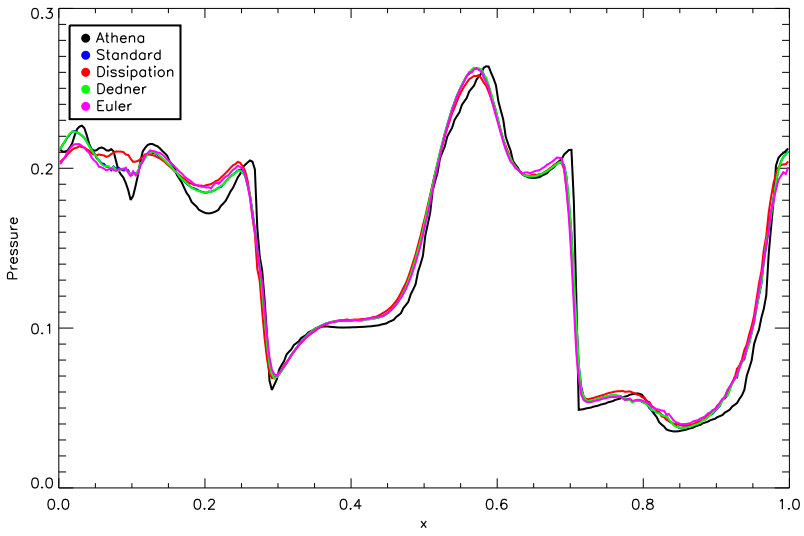

Figure 2.13: A $t = 0.5$ cut through the pressure in the *Orszang-Tang Vortex* at $y = 0.4277$.As before, the black line reflect the results obtained with ATHENA, in blue the standard, in red the artificial dissipation, in green the *Dedner* and in pink the *Euler* potentials implementation. The cut is chosen to compare with results from the literature, e.g. Børve et al. (2006). Note the variations in the solution between schemes, mainly due to the difference in the dissipative characteristics. However, the overall solutions are in reasonable agreement.

conditions. Having this information we can distinguish better which issues comes from the SPH formulation itself and which ones come from the MHD part.

In Fig. (2.14) we plot the $\nabla \cdot \mathbf{B}$ errors as defined by Eq. (2.57). First, the errors from the *Dedner* implementation, in the middle the results from the *Euler* formulation, and finally an example from the dissipative method. Note, that as by construction, the *Euler* scheme should be divergenceless, this shows that with the *Dedner* implementation we are already at the numerical limit. Most of the errors will come from the stochasticity and sampling noise. The only way to get rid of this is to use an extension to the "ideal" MHD as are the magnetic field smoothing or artificial dissipation.

2.5 Discussion

We presented the implementation of MHD in the cosmological, SPH code GADGET. We performed various test problems and discussed several instability correction and regularization schemes. We studied demonstrated the role of the $\nabla \cdot \mathbf{B} = 0$ constrain and schemes with resolution and comparing them to Eulerian solutions.

Our main findings are:

- The combination of many improvements in the SPH implementation, like the correction terms for the variable smoothing length (Springel and Hernquist, 2002) as well as the usage of the signal velocity in the artificial viscosity (Monaghan, 1997) together with its generalization to the MHD case (Price and Monaghan, 2004a) improve the handling of magnetic fields in SPH significantly.

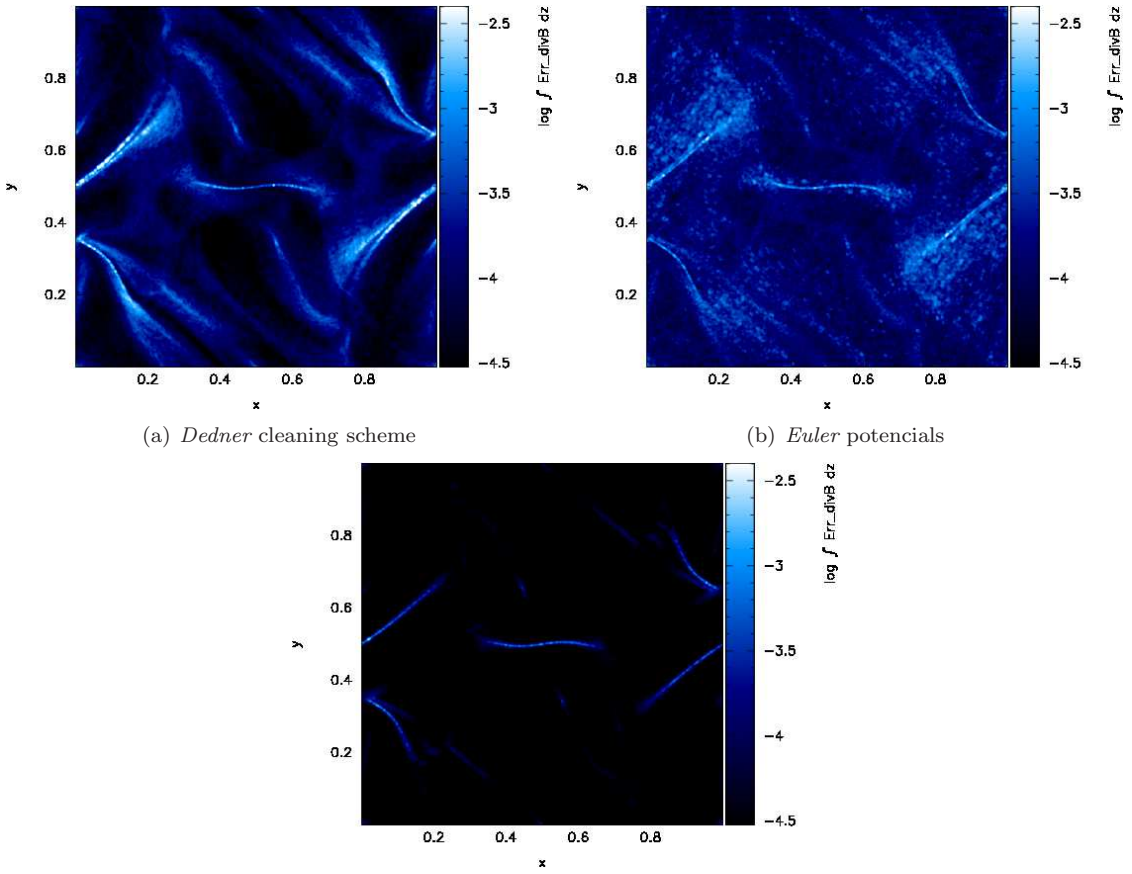

(a) *Dedner* cleaning scheme

(b) *Euler* potencials

(c) Artifitial dissipation

Figure 2.14: $\nabla \cdot \mathbf{B}$ errors as defined by Eq. (2.57). First, the errors from the *Dedner* implementation, in the middle the results from the *Euler* formulation, and finally an example from the dissipative method. Note, that as by construction, the *Euler* scheme should be divergenceless, this shows that with the *Dedner* implementation we are already at the numerical limit. Most of the errors will come from the stochasticity and sampling noise. The only way to get rid of this is to use an extension to the "ideal" MHD as are the magnetic field smoothing or artificial dissipation.

- Correcting the instability by explicitly subtracting the contribution of a numerical non-zero divergence of the magnetic field to the Lorenz force from the Maxwell tensor as suggested by Børve et al. (2001) seems to perform well. To avoid spurious instabilities due to sampling problems, particularly in the front shocks, a maximum threshold in the correction improves the performance and quality. Specifically in three dimensional setups where it seems to work much better than other suggestions in the literature. This feature turn out to be fundamental to progress in works like Bürzle et al. (2010) and Kotarba et al. (2010b), where previously the numerical instabilities dominate and such problems could not be investigated.

- The SPH-MHD implementation performs very well on our multidimensional shock tube tests as well as on commonly used planar test problems. We performed all tests in a fully three-dimensional setup and find excellent agreement of the results obtained with the SPH-MHD implementation compared to the results obtained with ATHENA in one or two dimensions only.

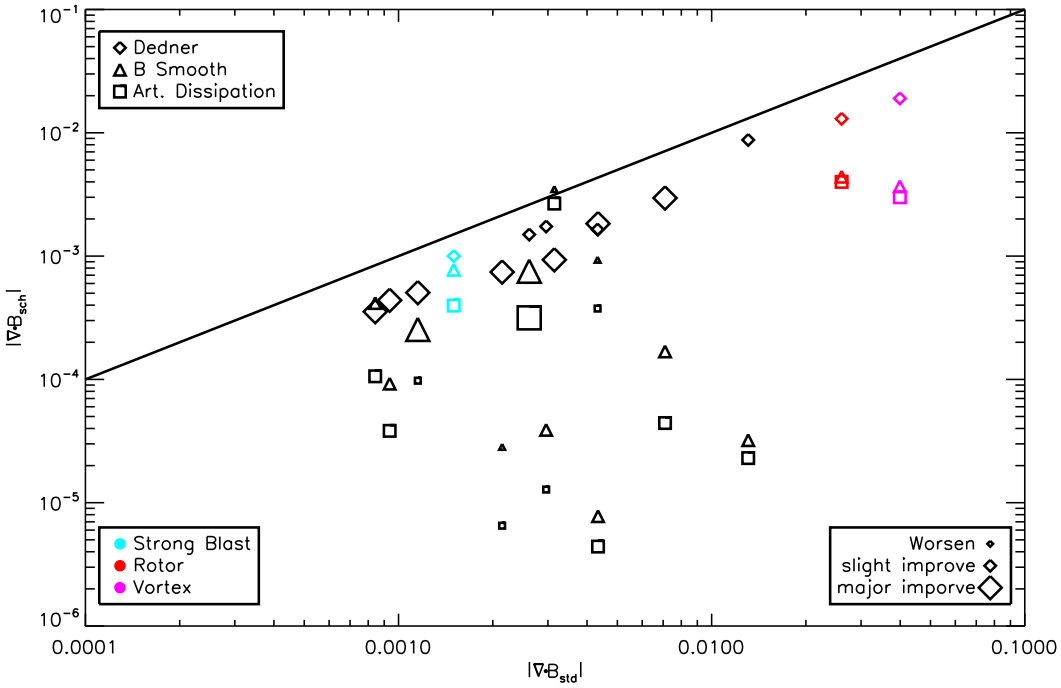

Figure 2.15: Comparison plot between all the implementation in tests. Clearly the dissipative schemes have lower $\nabla \cdot \mathbf{B}$ errors, however *Dedner* cleaning schemes outstands, as the lowers the $\nabla \cdot \mathbf{B}$ keeping the diffusion at Hsml scale. Also is shown when the tests are improved compared with correct solutions. We can see the trend when the dissipative effects make the final result differ by smoothing features.

- The stability of our implementation corresponds to the expected values for the tests, without bias and low inter particle scatter.

- We successfully implemented for first time a multidimensional divergence cleaning method in SPH. We showed that *Dedner* scheme does not affect strongly the shape of shocks, but reduces the $\nabla \cdot \mathbf{B}$ errors. This is important in physical meaningful situations. Also the evolution of this correction is completely local and only affected by the SPH interpolants.

- Regularization schemes help to further suppresses noise and $\nabla \cdot \mathbf{B}$ errors in the test simulations, however one has to carefully select the numerical parameters to avoid too strong smoothing of sharp features. Performing a full set of shock tube tests allows one to tune the numerical schemes and to determine optimal values in different conditions (i.e. rarefaction, magnetic-sonic regimes, etc.).

- The magnetic field smoothing succeeds in terms of stability, however in general it over-smooths features. Also is parametrised by global time-steps of all the particles, therefore it will not adapt to dynamical changes.

- The artificial dissipation implementation also increases the stability and behaves similar to the magnetic field. In this case, the over-smoothing of features comes from the changes in the magnetic field morphology itself, as expected from the scheme.

There is no dependence in global time-steps, and it will only depend on the local magnetic field gradients.

- We implemented an *Euler* Potential approach to evolve the magnetic field without the need of the induction equation. This has the benefits of fulfill the constraint $\nabla \cdot \mathbf{B} = 0$ by construction, up to the numerical level. We demonstrated that our schemes reached these errors levels when measure them in the tests (see Fig. 2.14).

The most important finding of our studies is the comparison to a divergenceless-by-construction scheme (i.e. *Euler* scheme). It shows tat we already reached the $\nabla \cdot \mathbf{B}$ error levels inherent from the SPH scheme itself, and any further cleaning or regularization will require to numerically dissipate the magnetic field. However this does not meant that we are error-free, thus still some $\nabla \cdot \mathbf{B}$ related instabilities can arise that we need to avoid. Additionally this shows the great improvements done in the underlying schemes since the first MHD-SPH implementations, where this instabilities dominate the SPH behavior.

Further more our code has different features with each regularization or cleaning scheme used. The success of $\nabla \cdot \mathbf{B}$ cleaning bring our simulations closer to the "ideal" MHD state. These flavor concentrates all the efforts of cleaning locally, by measuring the "local" error and subtracting it in the Induction equation.

In Fig. (2.15) we show the comparison between all the implementations in different tests. Clearly the dissipative schemes have lower $\nabla \cdot \mathbf{B}$ errors, however *Dedner* cleaning schemes out stands, lowering the $\nabla \cdot \mathbf{B}$ keeping the diffusion at Hsml scale, and in most of the cases improving the results. In contrast there some tests show that to lower $\nabla \cdot \mathbf{B}$ errors the scheme over smooth features, therefore enhancing differences with the correct solution.

Other regularization schemes (e.g. as smoothing and artificial dissipation) depend strongly on the gradients of the magnetic field. Both cases can be seen as mimics of *Ohmic* dissipation. Therefore, leading us away from "ideal" MHD, fact which can be an issue for further development of additional physics. Furthermore, a non dissipative scheme will allow more complex morphological structures as expected in complex regions as galaxy cluster cores. From the other side, additional physics like *Ohmic* dissipation are expected to be important (Bonafede et al., 2010), being an interesting case for the physics to be added, and making important to know how our numerical dissipation works.

Part III

Applications

Chapter 3

Galaxy cluster and magnetic fields

A subtle thought that is in error may yet give rise to fruitful inquiry that can establish truths of great value.

Isaac Asimov (1920-1991)

We already discussed some properties and open issues of galaxy clusters in the first chapter especially in sections 1.1 and 1.3. As we mentioned galaxy clusters are complex systems, with a long history from their hierarchical build up within the large-scale structure of the Universe. Therefore, to study their formation it is necessary to follow a large volume of the Universe. We also mentioned that simulations described fairly well the self-similar scenario, but we must go down to to relatively small scales, thus spanning 5 to 6 orders of magnitude in size, to describe them properly. The complexity of the cluster atmosphere reflects the in-fall of thousands of smaller objects and their subsequent destruction or survival within the cluster potential. Being the source of shocks and turbulence, these processes directly act on the magnetic field causing re-distribution and amplification. Therefore realistic modelling of these processes critically depends on the ability of the simulation to resolve and follow correctly this dynamics in galaxy clusters.

To perform our studies we use a re-simulation of a Lagrangian region selected from a lower resolution dark matter only cosmological box. This parent simulation has a box–size of 684 Mpc, and assumed a flat ΛCDM cosmology with $\Omega_m = 0.3$ for the matter density parameter, $H_0 = 70$ for the Hubble constant, $f_{bar} = 0.13$ for the baryon fraction and $\sigma_8 = 0.9$ for the normalization of the power spectrum. The cluster has a final mass of $1.5 \times 10^{14}\ M_\odot$ and was re-simulated at 3 different particle masses for the high resolution region. Using the "Zoomed Initial Conditions" (ZIC) technique (Katz and White, 1993b; Tormen et al., 1997), these regions were re-simulated with higher mass and force resolution by populating their Lagrangian volumes with a larger number of particles, while appropriately adding additional high–frequency modes drawn from the same power spectrum. To optimize the setup of the initial conditions, the high resolution region was sampled with a 16^3 grid, where only sub-cells are re-sampled at high resolution to allow for quasi arbitrary shapes of the high resolution region. The exact shape of each high–resolution regions was iterated by repeatedly running dark-matter only simulations, until the targeted objects are clean of any lower–resolution boundary particle out to $3 \sim 5$ virial radii. The initial particle distributions, before adding any Zeldovich displacement, were taken from a relaxed glass configuration (White, 1996). The

three resolutions used correspond to a mass of the dark matter particles of $1.6 \times 10^9 M_\odot$, $2.5 \times 10^8 M_\odot$ and $1.6 \times 10^8 M_\odot$ for the *1x*, *6x* and *10x* simulation. The gravitational softening corresponds to 7, 3.9 and 3.2 Kpc respectively. For simplicity we assumed an initially homogeneous magnetic field of 10^{-11} G co-moving as also used in previous work (Dolag et al., 1999, 2002). Furthermore we tested our different implementations. We applied the regularization by smoothing the magnetic field in the same way than we did in previous work (Dolag et al., 2004a, 2005a). We also checked the effects of regularization by artificial dissipation varying values of α_B and in the case of the cleaning scheme, we test a small set of parameters. Always in correspondence with the results shown in the appendix B.

Fig. (3.1) shows a zoom-in from the full cosmological box down to the cluster. The structures in the outer parts get less pronounced due to the decrease in resolution, which is designed to capture only the very largest scales of the simulation volume. Each panel shows (in clockwise order) a zoom-in by a factor of ten. Finally the elongated box in the lower left panel marks the size of the observational frame shown on the left. The dynamical range of the simulation spawns more than five orders of magnitude in spatial dimension. The size of the underlying box is 6 and 5 times larger than the AMR simulations presented in Dubois and Teyssier (2008) and Brüggen et al. (2005), respectively. Still the resolution of the underlying dark matter distribution is, respectively, 2 and 5 times better than these AMR simulations and the cluster is resolved with more than one million dark matter particles within the virial radius at the *10x* resolution.

We mainly focus on the aspects of the magnetic fields itself. Given the complexity inherent from MHD simulations, our the studies shown here are non-radiative to understand better how the different implementations them selfs capture the magnetic field features without any confusion possible from additional physics.

3.1 Galaxy cluster slices

We study the inner part of the object making slices trough the center, giving us broad information in the magnetic field distribution. Fig. (3.2) shows a density slice for two different resolutions *1x* and *10x*, easily is seen that smaller structures are resolved in the higher resolution slightly changing the dynamics of the system. However, we don't observe important difference between the different schemes. In figure Fig. (3.3) we see characteristic shapes of the magnetic field distribution inside of the galaxy cluster, compared with Fig. (3.2) one can observe the expected correlation between the density and the magnetic field. In high β plasmas as the ones we are simulating, the magnetic field lines are "frozen" to it, being compressed and advected all together. Smaller structures are resolved in the higher resolution slightly changing the dynamics of the system.

The diffusive schemes, panels *c* and *d* in Fig. (3.3), show less growth of the magnetic field towards the center due the transport of the field to the cluster surroundings. The Standard, *Euler* and *Dedner* implementations are able to keep the magnetic field in the central part. We study two cases for the *Euler* potential runs, one following the *Lorentz* force, while other run is completely hydrodynamical but we build up the final magnetic field from the *Euler* potentials. Remember that the *Euler* scheme is valid only at approximately the firsts winding of the field, basically it breaks when the reconnection should occur, and the scheme is unable to handle it. Therefore the panel *e* from Fig.

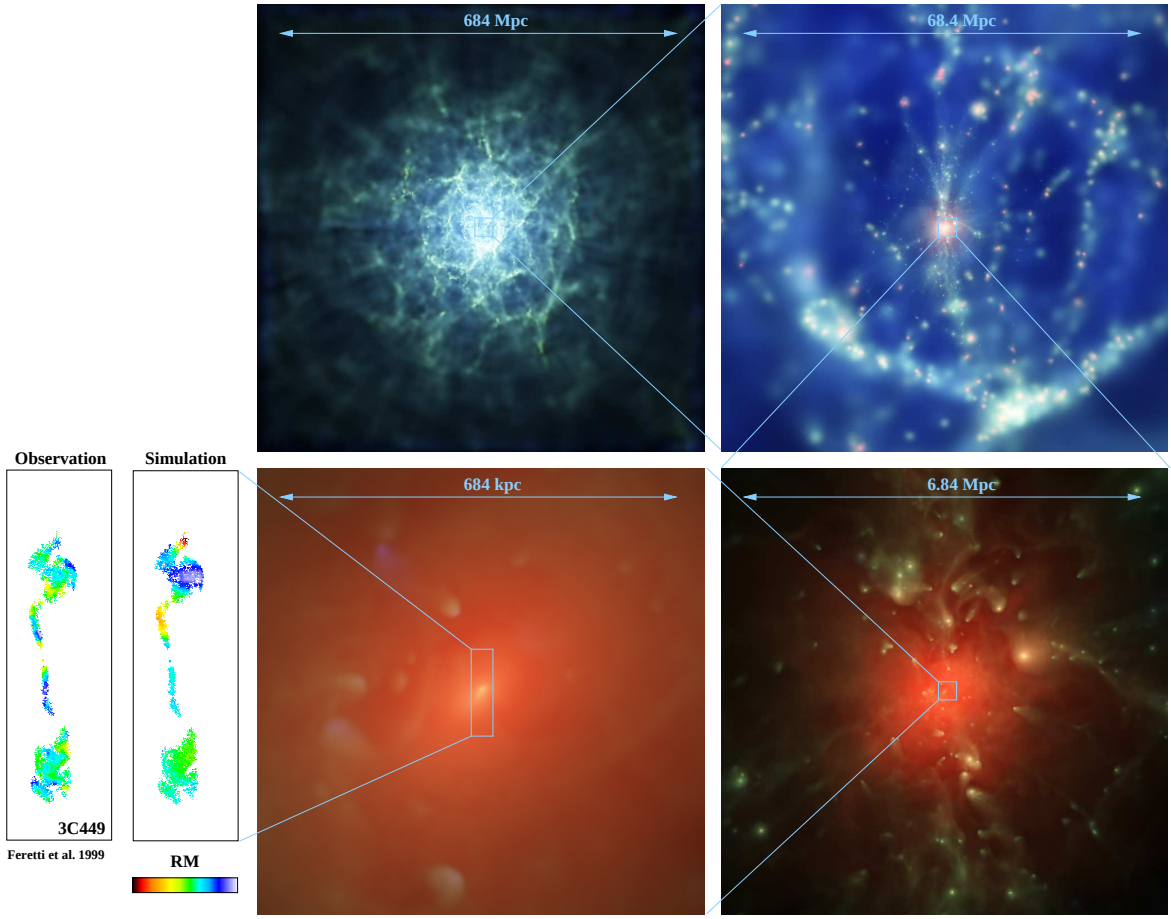

Figure 3.1: Zoom into the cluster simulated within the cosmological box. Clockwise, each panel displays a factor 10 increase in imaging magnification, starting from the full box (684 Mpc) down to the cluster center (680 Kpc). On the very large scale, the density of the dark matter particles are shown, whereas in the high resolution region the temperature of the gas is rendered to emphasize the presence and dynamics of the substructure. The last zoom extracts a region of the same size of an observed radio jet (3C449) with measured rotation measure (Feretti et al., 1999b). Both, the simulated and the observed map are displayed using a linear color-scale based on the minimum and maximum values in the maps. The synthetic RM map is clipped to the shape of the observations.

(3.3) represents the distribution from a random magnetic field but with the dynamic of the system modified by an additional magnetic pressure. The final panel *f* shows the magnetic field is build from the advection of the potentials taking only the hydrodynamical forces into account. The result should be considered as magnetic field from a complete hydrodynamical turbulence case. In Fig. (3.4) we see the same cut but showing the $\nabla \cdot \mathbf{B}$ errors for different regularization schemes. The first thing to notice is that we are still in a low percentage error, compared with the magnetic field strength. In the standard case and *Dedner* case the values are higher than in the other runs, however, the errors are smaller with the *Dedner* scheme. In the high density regions are the lower values, with the exception of the *Euler* potential cases where the errors are almost constant trough the slice. This is explained, in the *Standard* case, because the numerical $\nabla \cdot \mathbf{B}$ errors in the center are temporal due to shock fronts passing thought the ICM

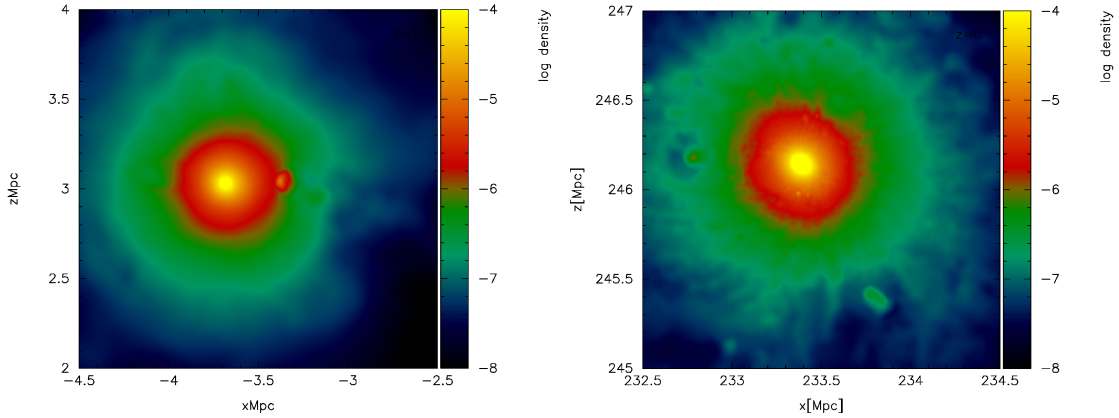

(a) Standard implementation 1x

(b) Standard implementation 10x

Figure 3.2: Density slice trough the center of the galaxy cluster at redshift $z = 0$ for two resolutions. Smaller structures are resolved at high resolution. This can slightly modify the dynamics of the system. However, the overall structure is similar and the radial profiles generally converge. When comparing the schemes, we don't found differences, even in density profiles.

(in the same way as shown in the test shock tubes). Meanwhile in the outer regions the dynamical times are longer and additionally the baryons properties are mostly driven by the kinetic energy (see appendix D). However, this facts does not apply to the *Euler* potential simulations because of the nature on how we build the magnetic field, from the final configuration of the adverted potentials. Additionally, is interesting to note that even if the representations of those fields have different origins ,one completely hydrodynamical and other magnetohydrodynamical (into some extent), there are no effects in in the $\nabla \cdot \mathbf{B}$ distribution, but there is change in the core magnetic field strength.

Besides the density comparison, we study the magnetic field in different resolutions runs. Slices comparing two resolutions and the magnetic properties are shown in Fig. (3.5). The amplification of the magnetic field is stronger as we increase the resolution, as a consequence of resolving better the turbulence at smaller scales. However, we don't see an enhancement of the values of the $\nabla \cdot \mathbf{B}$ errors, getting even a lower average. This fact demonstrates that the growth of the magnetic field in SPH schemes is not dominated by $\nabla \cdot \mathbf{B}$ terms that generate instabilities and unphysical dynamo effects (Brackbill and Barnes, 1980). In the inner region of the cluster, the turbulent motions and shocks from the incoming halos that steer the ICM can lead to complex configurations of magnetic fields, being a source of $\nabla \cdot \mathbf{B}$ errors to appear temporally. These kind of errors are harmless for the overall evolution of the code because, being just a temporary stage located in the front shocks (as seen also in the tests), and do not propagate, and any further spurious effect is controlled by the improvements in our implementations (section 2). As is seen in the shock tube and test problems, in the front shocks itself there is a numerical $\nabla \cdot \mathbf{B}$ because a numerical incapacity in properly resolve that particular region between two divergenceless stages. However as soon as the front shock went trough that region the field keeps evolving to the correct solution of the shock problem. Different is the case of the outermost regions. There the magnetic field energy is quite low compared with thermal or kinetic [1] ,making the magnetic field be dominated by the kinematics of

[1]We are always in a high $\beta_{plasma} = 8\pi \cdot u/B^2$ regime, in this cases we refer higher than 10^9, see apendix D to see an

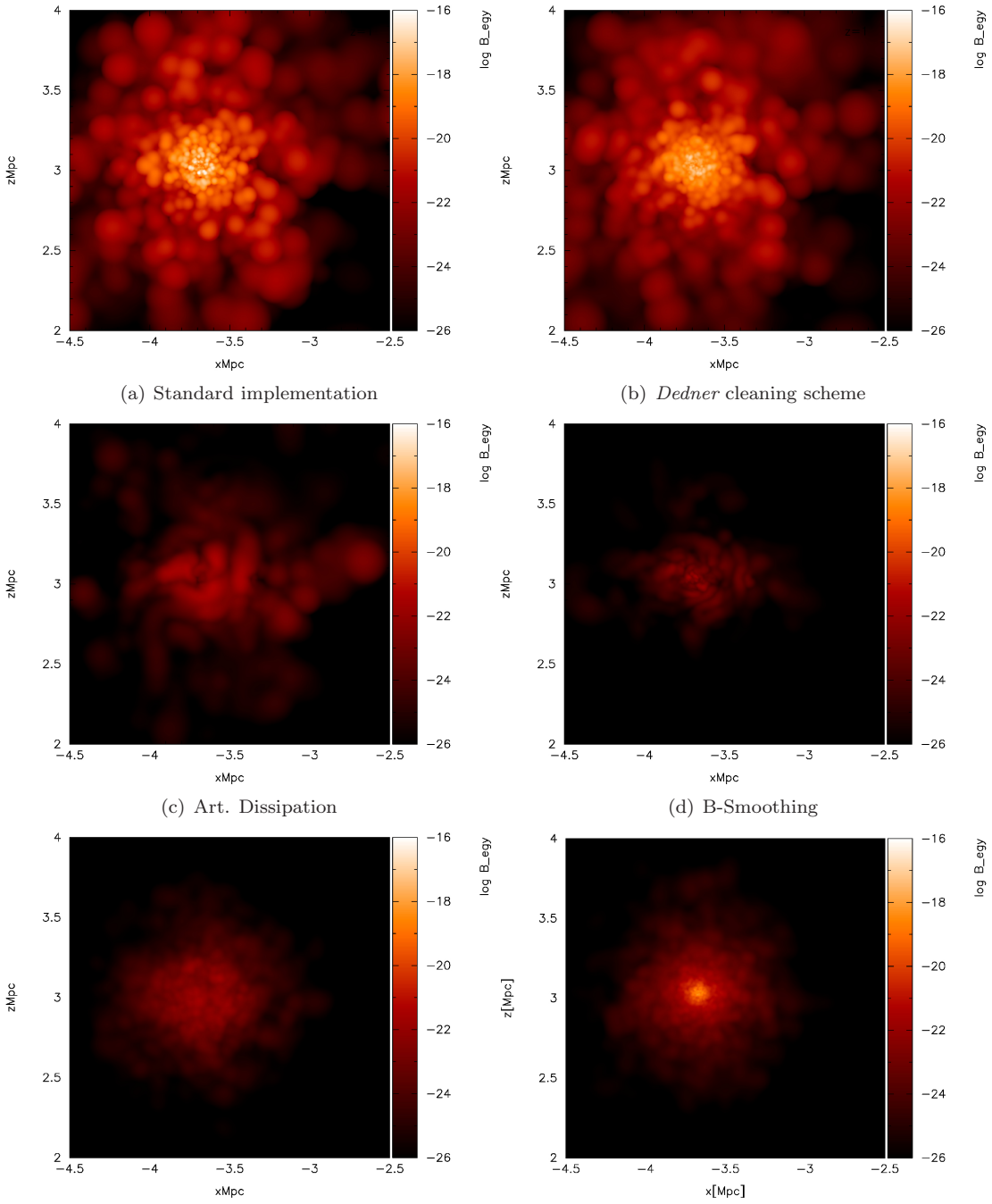

(a) Standard implementation

(b) *Dedner* cleaning scheme

(c) Art. Dissipation

(d) B-Smoothing

(e) *Euler* Potentials

(f) *Euler* Pot. without *Lorentz* Force

Figure 3.3: Magnetic field energy density slice trough the center of the galaxy cluster at redshift 0 for the *1x* resolution runs. Different panels show the magnetic regularization/cleaning schemes. One can see several differences in magnetic field distribution. Also there is a decrease of the center values for the schemes more diffusive. In the case of *Euler* Potentials is due the lack of reconnection. The Standard and Dedner, slices (a) and (b), show the large scatter in low density regions that will be the main source of the $\nabla \cdot \mathbf{B}$ errors. Finally we show two runs of the *Euler* potentials implementations with and without the back reaction given by the *Lorentz* force. The run without force represents a magnetic field distribution completely build from the Hydrodynamical turbulence, while the run with force build a magnetic field from a almost randomly distributed magnetic field.

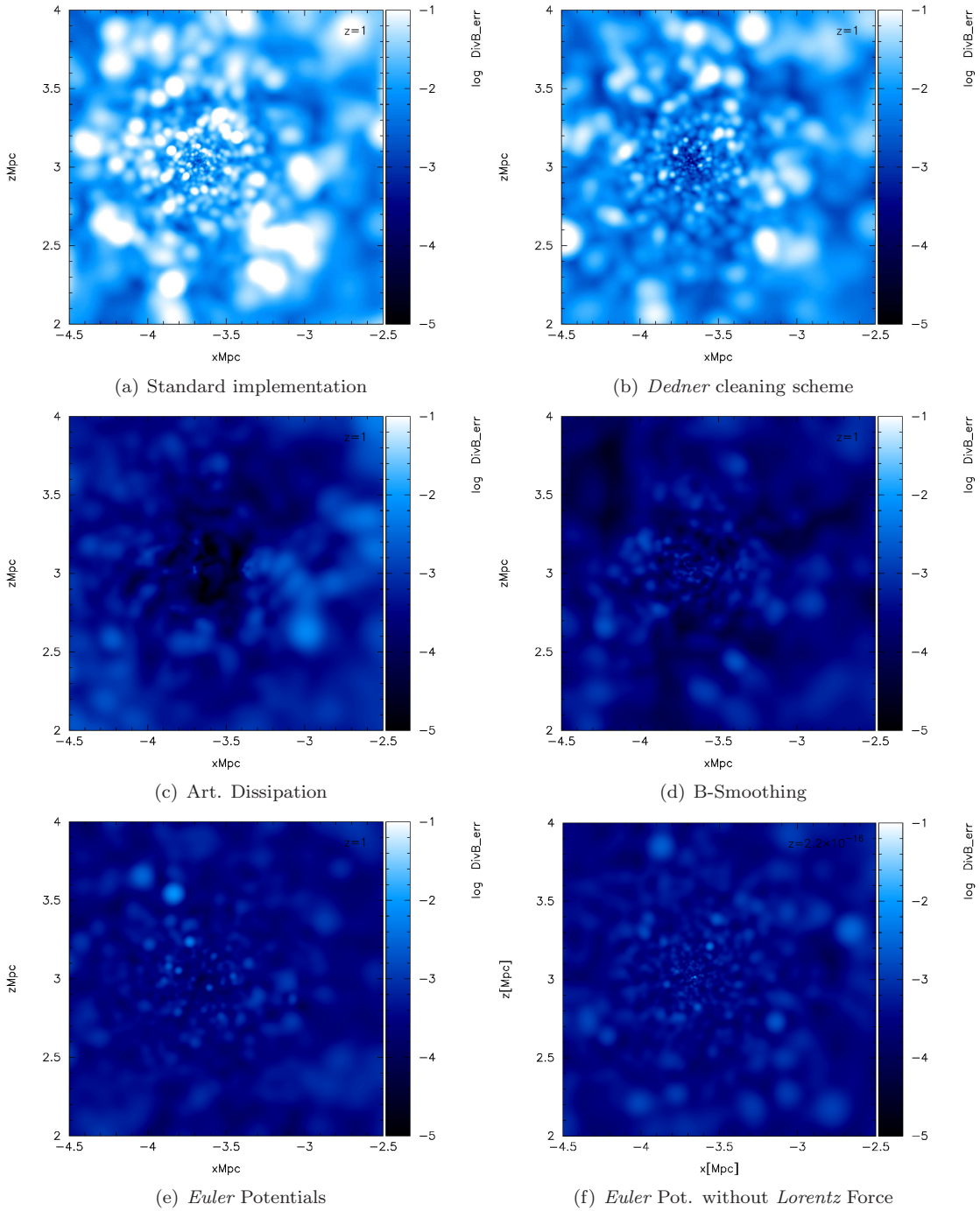

(a) Standard implementation

(b) *Dedner* cleaning scheme

(c) Art. Dissipation

(d) B-Smoothing

(e) *Euler* Potentials

(f) *Euler* Pot. without *Lorentz* Force

Figure 3.4: $\nabla \cdot \mathbf{B}$ errors cut trough the center of the galaxy cluster at redshift 0 and *1x* resolution. We present the same resolution with different regularization schemes. One can see several substructures in the $\nabla \cdot \mathbf{B}$ errors, that anti-correlates with density, with exception of the *Euler* potential cases. The lower $\nabla \cdot \mathbf{B}$ errors are obtained with the dissipative schemes, however we are still in small faction of the total magnetic field strength.

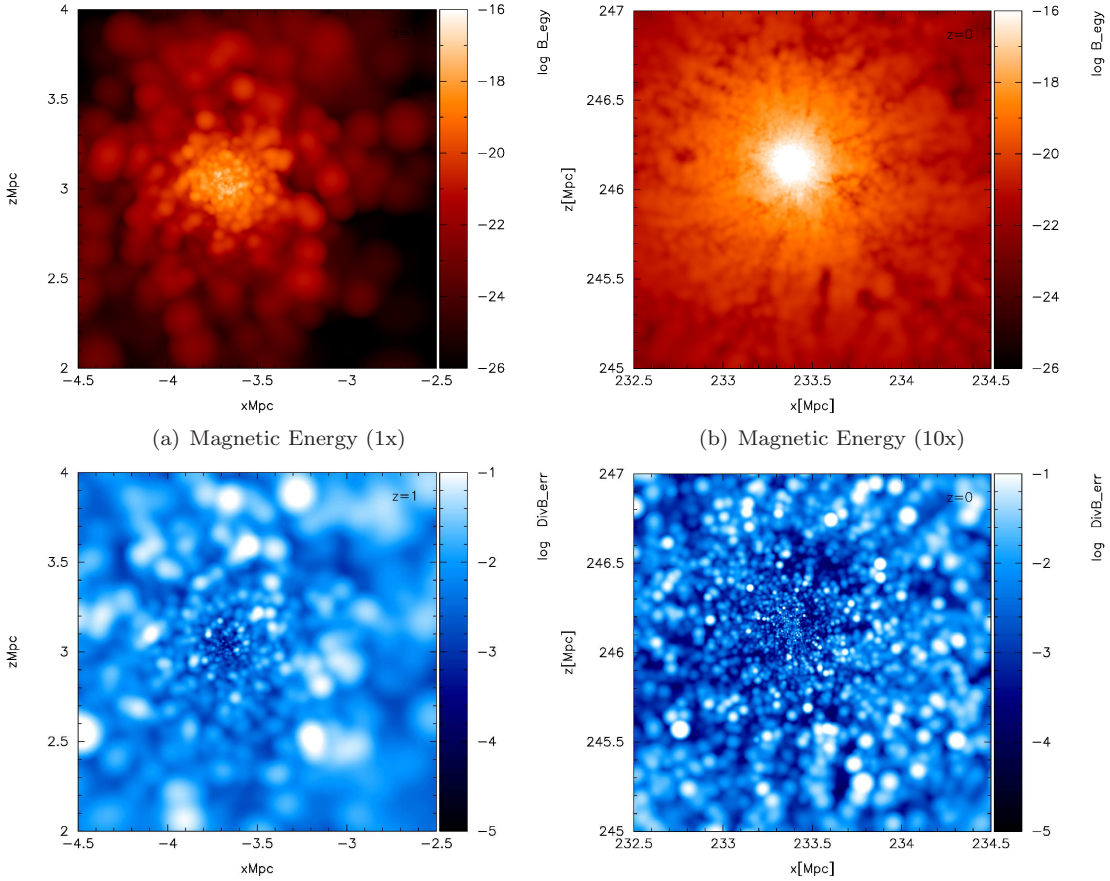

(a) Magnetic Energy (1x)

(b) Magnetic Energy (10x)

(c) $\nabla \cdot \mathbf{B}$ errors (1x)

(d) $\nabla \cdot \mathbf{B}$ errors (10x)

Figure 3.5: In the first row we show the magnetic energy slices trough the cluster center at redshift $z = 0$ for two different resolutions. We are able resolve smaller scales and follow the turbulent motions accordingly, showing an enhancement of the magnetic field. In the bottom row are shown $\nabla \cdot \mathbf{B}$ errors slices. Note that increasing the resolution we decrease the errors in the inner region, demonstrating the fact that the inner errors are consequence of the temporary unresolved shock fronts, as found in shock tube tests.

the baryons. Additionally the non-diffusive characteristic of SPH, makes the $\nabla \cdot \mathbf{B}$ errors difficult to disappear (see Appendix D). Finally, density and magnetic field profiles have different slopes in the outskirts of the cluster or in the halos in the simulation, being the magnetic field profile steeper. This facts in the outskirts of the cluster, can be a source of instabilities that can be solved implementing high order *Kernels* or taking special care in the time step integration for those particles.

3.2 Magnetic field profiles

In Fig. (3.6), the radial magnetic field profiles (left panel) as well as the numerical $\nabla \cdot \mathbf{B}$ errors to (right panel) are shown. For galaxy clusters, only the shape of the predicted magnetic profiles converge (with the exception of the central part of clusters)

distribution of β_{plasma}.

with resolution and are in good agreement with previous studies (Dubois and Teyssier, 2008; Brüggen et al., 2005), and in correspondence with the self-similar models. The shape of the magnetic field is basically unchanged when including the *Dedner* cleaning scheme, however, the numerical $\nabla \cdot \mathbf{B}$ error drops almost one order of magnitude in the center (see right panel in Fig. 3.6). These values are at the same level of the *Euler* case in the center, therefore we reach the numerical threshold given the resolution. In addition, we show the *Euler* implementation without any back reaction from the *Lorentz* force dynamics. Therefore, the final stage of the magnetic field comes from the construction of the advected quantities that only follow hydrodynamical forces. In this configuration, as we lack of the magnetic pressure, the magnetic field continues rising towards the center. Note that the *Dedner* method is characterized to transport and dump the numerical errors outside our region of interest (the halo). In the case of a periodic box (as it happened in the *Vortex* test) the most important parameter in that scheme is π, which control the dumping term, however in the case of open boundaries and collapsing regions we note that σ, which control the propagation, should be high enough otherwise we cumulate errors in the center of the cluster. Previous works in star formation works, using the *Dedner* method, this velocity propagation was fix and not studied, reporting no success for this implementation (Price and Monaghan, 2005). The dissipative regularization schemes, namely *Art. Dissipation* and *B-smoothing*, does get lower errors but at the cost of suppressing the turbulent growth of the field.

Comparing the panels in Fig. (3.6), we demonstrate that the amplification of the magnetic field in is not significantly influenced by the non-zero numerical $\nabla \cdot \mathbf{B}$. The central $\nabla \cdot \mathbf{B}$ errors for the dissipative schemes and *Dedner* are similar (even for the case of hydrodynamical case of *Euler*) but the central magnetic field differs in several orders of magnitude.

As already noted in earlier work (Dolag et al., 2002), in Fig. (3.8) shows the dependence of the amplification of magnetic fields with resolution. In addition, although the absolute value of the amplification is not converged yet with resolution, the shape of the predicted magnetic field profile appears to be converged. Note that this convergence, as usual for all hydro-dynamical quantities, is only reached at radii significant larger than the size of the gravitational softening, that in our cases is ~ 10 Kpc, ~ 7 Kpc and ~ 6 Kpc for the $1x$, $6x$ and $10x$ respectively.

The situation changes when using artificial magnetic dissipation, as shown in Fig. (3.7). In the left panel we show the magnetic field profiles for three values of α_B compared and two frequency values for the magnetic field smoothing. Clearly a normal value ($\alpha_B \sim 0.5$) for artificial magnetic dissipation leads to a large dissipation of magnetic field over the simulation time (e.g. close to the Hubble time). The right panels show the profiles artificially normalized at large radius ($\sim 1Mpc$). Clearly the self similarity of the profiles is lost. Therefore it appears that the use of artificially dissipation as a regularization scheme is not a good choice for cosmological simulations. Additionally it points out that true physical dissipation might play an important role in determining the shape of the magnetic field profile in galaxy clusters. Here transport processes, the role of cosmic rays, turbulence (specially at scales below the resolution) as well as reconnection of magnetic field lines are not well understood.

Within the ICM there the micro-physics mentioned are far outside the resolution scales which can be ever reached by cosmological simulations, future work will have to include them as sub-grid models. This means, additional physic models to be followed inside

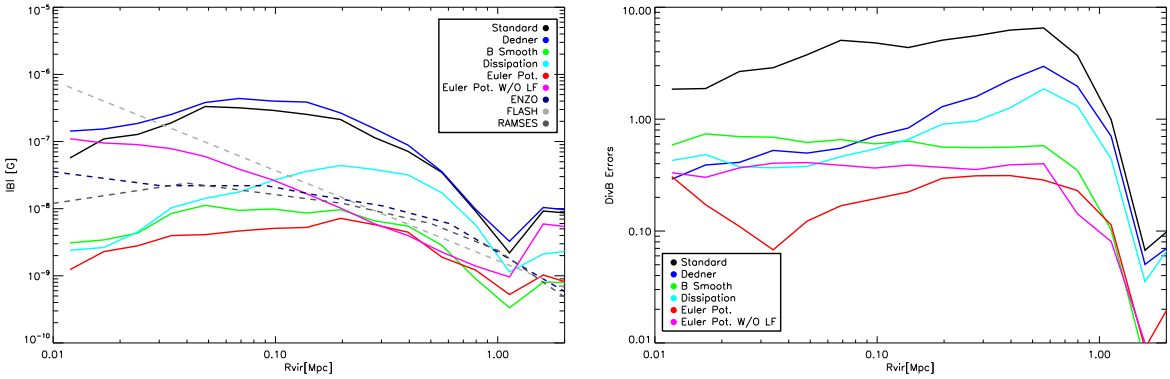

Figure 3.6: In the left magnetic field profiles obtained for the galaxy cluster using different regularization methods. Additionally, results from Eulerian codes are shown. In the right panel the profile of the $\nabla \cdot \mathbf{B}$ errors are shown. Note how the results improves with the methods towards the center, reaching values below one. The *Euler* potentials case without the *Lorentz* force mimics the case of a random field dominated by the turbulence hydrodynamic. Therefore the $\nabla \cdot \mathbf{B}$ errors are almost constant inside the cluster and the profile keeps growing towards the center.

the Hsml kernel, and motivated and corroborated by small scale numerical experiments. The existing implementations of radiative cooling, star formation and AGN feedback do not take into account yet the effects of magnetic fields. Magnetic fields can act as an additional reservoir of energy, therefore a self-consistent implementation is needed. In the case of radiative cooling, this addition might not only give a more complete physical scenario but also contribute to prevent the excessive clumping of the baryons that needs to be re-heated by some other mechanism (e.g. *Supernova* feedback).

The results obtained with dissipative regularization schemes in cosmological simulations indicate that physical dissipation could play a crucial role in determining the exact shape of the predicted, magnetic field profiles in galaxy clusters. Future work, especially when including more physical processes at work in galaxy cluster – as can be done easily with our SPH-MHD implementation – might reveal an interesting interplay between the dynamics of the cluster atmosphere and amplification of magnetic fields. Thus having the potential to shed light on many, currently unknown aspects of cluster magnetic fields, their structure and their evolution.

3.3 Synthetic RM Measurements

For comparison with observations we produced a synthetic Faraday rotation map from the simulation, additionally this studies give an indication of the structures resolved by our simulations. The simulations were not specially designed to compare with an object in particular, therefore in these comparisons we focus on the main features of the schemes contrasted with a real astrophysical system. As we shown the schemes have different magnetic field growth rates, but the baryon distribution is quite similar. Therefore we focus on the spatial distribution and structures obtained. As in observations, a Faraday rotation map give us spatial information in the line of sight distribution of magnetic fields and constrains on the morphological properties. As we discussed early, in Section 1.3,

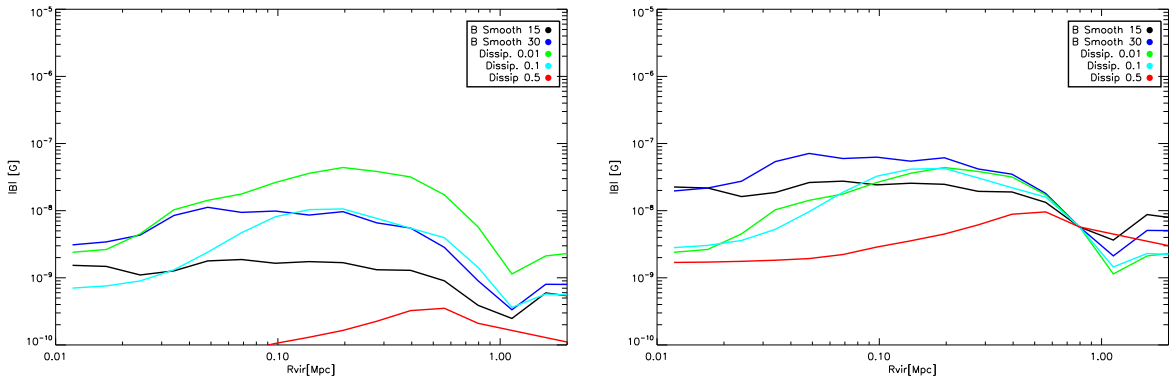

Figure 3.7: The magnetic field profiles obtained for the galaxy cluster using different Art. Dissipation constants and Smoothing the magnetic field at different frequencies. The right panel shows the normalized profiles at $\sim$ 0.8Mpc. Therefore the changes in the shape of the profile as stronger is the diffusivity is shown.

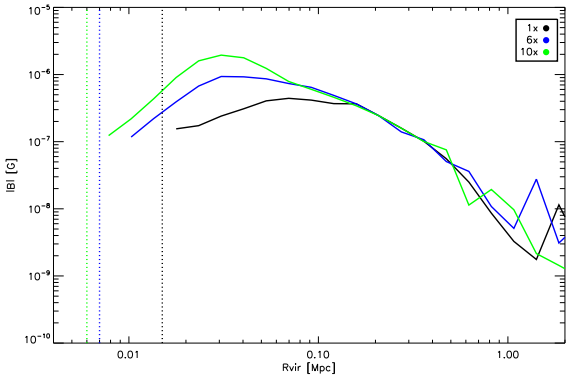

Figure 3.8: The magnetic field profiles for a resolution study of our cluster. The profiles are normalized to the value of the (1x) simulation at $\sim$ 0.8Mpc. In dashed lines we see the limit resolution given by the Hsml. We can observe how increases the central values of the magnetic field.

the inner regions of the galaxy cluster environment presents a complex mixture of physics that imprints all the formation history of the observed object. In our case we compare with simulations simple physics and magnetic fields, that in any case were meant to match an specific object. However, the comparison are needed as a starting point to validate our schemes, at least to broadly reproduce basic observation features. In section 1.2 we presented *Faraday* rotation measures, basically this observation that depends on the electron density and the strength of the magnetic field in the line of sight. It is an integrated quantity, therefore there is the cumulative effect during the path to the observer. Given the information (e.g. density, temperature, magnetic field) that we have from our numerical simulations we are able to build these line of sight integration. However only in the volume that our simulation occupies, therefore we neglect the effects from the foreground. In our case this hypothesis is not so bad, given the distance of the sources, the angular diameter is small and therefore the expected contribution from the close foreground sources will be constant or at least smooth. The fact that we don't know

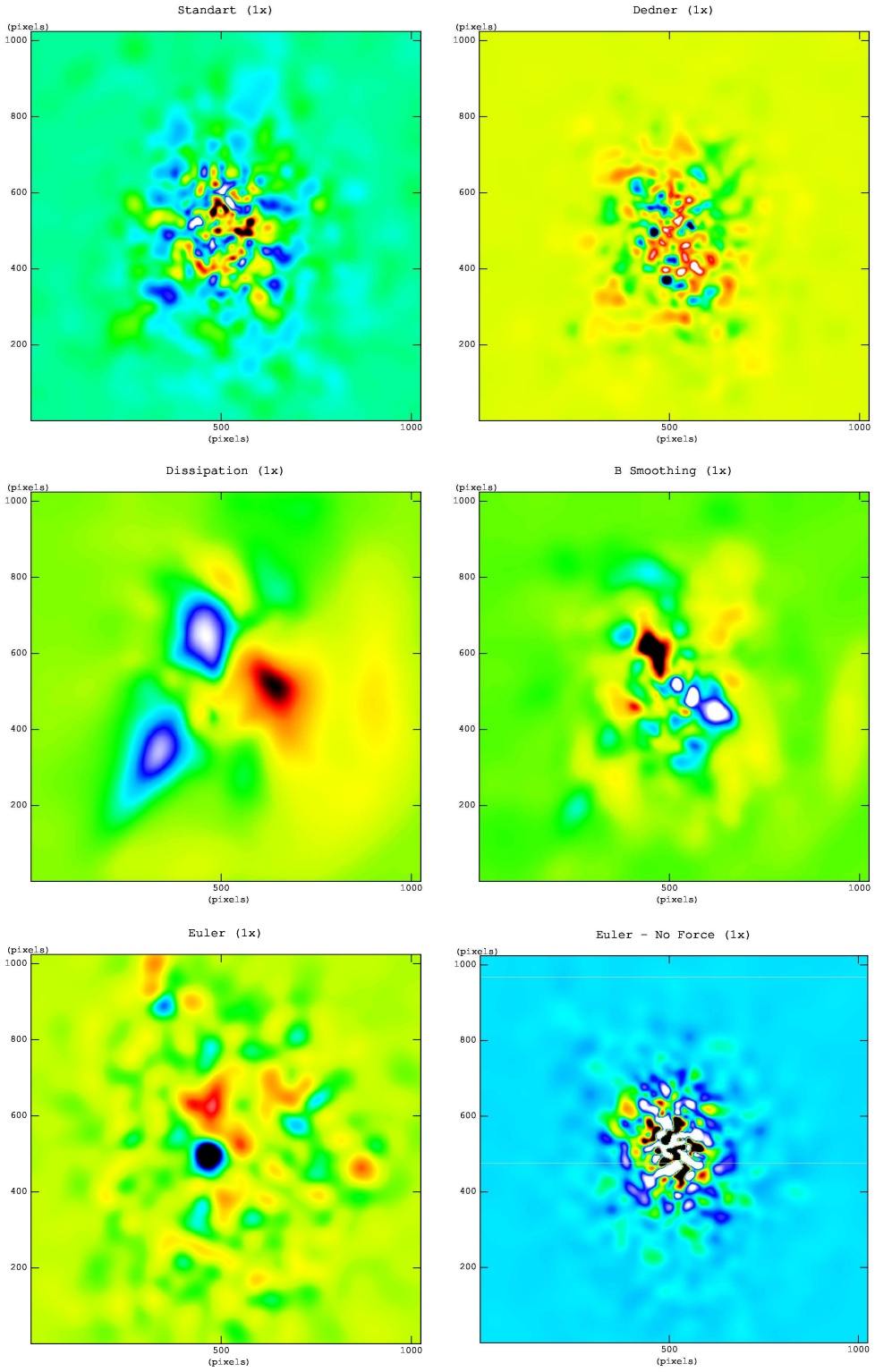

Figure 3.9: Synthetic RM maps for the single resolution and several regularization schemes. Note how the dissipative schemes diminish the amount of rehearsals and the extension. All the plots have an scale of 0.8 Kpc/pix, so we cover the central part of the cluster.

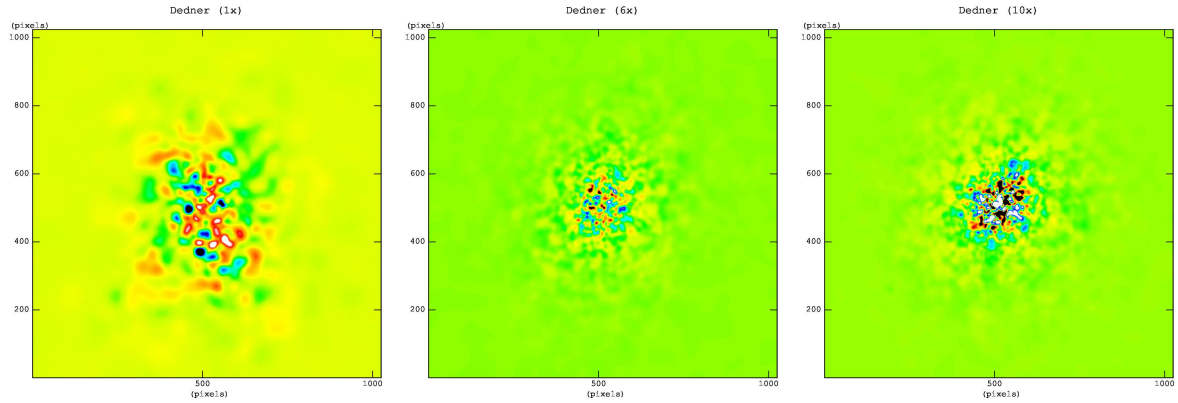

Figure 3.10: Synthetic RM maps for different resolutions with *Dedner* regularization scheme. Note that as we increase the resolution we resolve more rehearsals in the field. Therefore we increase the amount of structures, but the morphology seems to be quite similar. All the plots have an scale of 0.8 Kpc/pix, so we cover the central and the outer part of the cluster.

exactly the foreground is not an issue, as we don't study the absolute values but their distribution inside the *Faraday* screen. Different is the case if we consider larger volumes as we do in chapter 4.

To make our synthetic maps from our simulations we use "Smac" (Dolag et al., 2005b), that basically reads our simulation output, project it to a given distance to match the observation size of the object, and integrates the magnetic field on the line sight, weighed by the electron density. This integration takes into account all the cosmological factors and effects due to the distances from the object, giving us as a result a mock observation.

Similar to plots in previous sections, in Fig. (3.9) we compare the effects of the regularization schemes at the same resolution. Note that the scale in the figures is 0.8 Kpc/pix, giving a total size for the image $\sim$ 0.8Mpc. This is half of the size of the slices shown in Fig. (3.3), properly centered on the cluster, and clearly showing the effects of the different numerical schemes. We observe the reversals of the magnetic field as bubbles or blobs in the figures. Note that we expect to have similar density distributions, therefore the patterns shown here are produced by the magnetic fields. The rotation measurements varies from hundreds rad m^{-2}in the Standard run to tens rad m^{-2}in the dissipative runs, therefore the plots are adjusted to remark the reversal sizes. The dissipative schemes diminish the amount of rehearsals and extend them for various Kpc, Consequently the other schemes have smaller reversals, with the exception of the *Euler* potentials. This case is particular, due the fact that tries to conserve the morphology of the field, therefore suppresses small reversals Formally speaking the *Euler* potentials have null helicity [2], this is a topological property of the field and is null from the way we re-construct the field. However, is an open issue if this property can evolve or is constant in time, recent studies concludes that is not a conserved (Brandenburg et al., 2009). However, our schemes using the induction equation do not suffer from this restriction.

In Fig. (3.10) we show the synthetic maps that come from the *Dedner* scheme applied at three different resolutions. We note an increase in the number of reversals with resolution. This is expected as we resolve more smaller structures and therefore the inverse turbulent

[2]Defined as $\int \mathbf{A} \cdot \mathbf{B} dV$

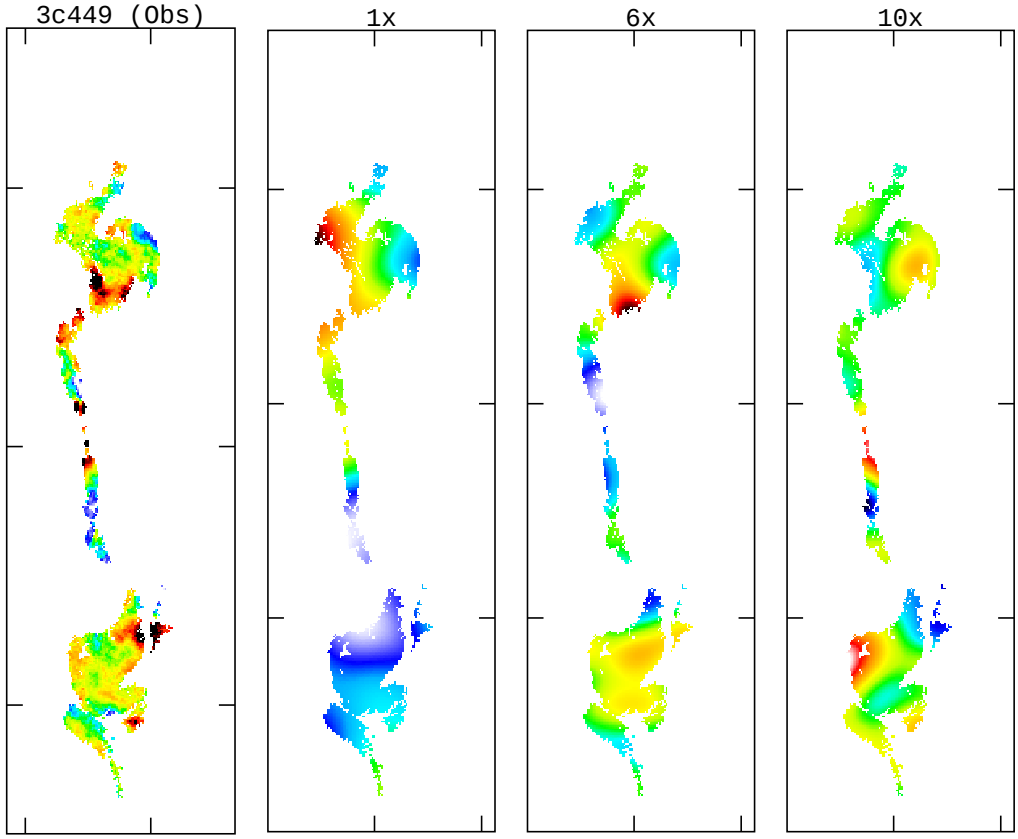

Figure 3.11: Shown is a comparison of the predicted RM signal from the cluster simulation at various resolutions compared to the observational signal. One can see that we still not reach the amount of small structure seen in the observation but, when we increase the resolution it begin to appear. In all this cases the projection scale is 0.17 Kpc/pix to be comparable with observations.

cascade, that we show enhances the magnetic field. Note that we reach coherence lengths of few Kpc, showing the complexity in morphology that the magnetic field lines can acquire.

To compare with observations of real objects, we need to build up RM maps, projecting the galaxy cluster to the observed resolution available, and using a mask with the shape of the *Faraday* screen. This help us to mimic any kind of bias that we can introduce in the latter comparison procedure. Note that the shape of the images is given by distribution of polarized emission of the observation. This can be quite irregular for several reasons: the shape of the source (in general a jet-like structure), the noise of the observation and the sensitivity of our instrument. The observation that we use is from Feretti et al. (1995) of 3c449, a radio galaxy. The soft X-ray emission from this object is dominated by an extended halo with a scale comparable to that of the radio source. Observations suggests that the jets are strongly influenced by the external medium. The minimum pressure in the radio lobe is considerably lower than estimates of the pressure in the external medium, meaning that is not in equilibrium (Hardcastle et al., 1998). The radio galaxy is located at $z = 0.1711$, giving us a resolution of 0.17 Kpc/pix in the image. The comparison results from our procedure are shown in Fig. (3.11).

3.4 Structure Functions

To obtain a more quantitative comparison we calculated the projected structure function

$$S(d) = \left\langle (RM(r') - RM(r'+d))^2 \right\rangle, \tag{3.1}$$

from both the observed and synthetic Faraday rotation maps, with $d = \sqrt{\Delta x^2 + \Delta y^2}$ being the radial offsets from a pixel at position $r = (x, y)$. The resulting matrix is then averaged in radial bins to obtain the structure functions.

Kraichnan (1965) formulate one of the first phenomenological theory of MHD turbulence. They argued that in the presence of a strong mean magnetic field, the Alfven waves will interact weakly, deriving an energy spectra that is proportional to $\sim k^{-3/2}$. However, if the magnetic field is weak, as used in most of the mean field theories, the expected magnetic energy spectra should be *Kolmogorov* like and expected to be proportional to $\sim k^{-5/3}$. Those phenomenologies assume isotropic turbulence, that may be not the case in some astrophysical systems, yielding to a suppression of the energy cascade along the direction of the mean magnetic field. However, observations in galactic scales (Han et al., 2004) and numerical simulations (Mason et al., 2008), flavors the *Kolmogorov* slope in the spectrum, meaning that there is a energy transfer from larger to small scales.

Following Ruzmaikin, A. A. and Sokolov, D. D. and Shukurov A.M. (1988), we can derive rough estimates for our structure functions for the rotation measurements. There will be a coherence length l_0, which will determine when the RM are not longer specially correlated. Thus, for scales $d \ll l_0$

$$S(d) \simeq RM_0^2 \left(\frac{d}{l_0}\right)^{2/3} \tag{3.2}$$

for the *Kolmogorov* spectrum and

$$S(d) \simeq RM_0^2 \left(\frac{d}{l_0}\right)^{1/3} \tag{3.3}$$

for the *Kraichnan* spectrum. At scales larger than l_0 the structure functions should be have a constant value RM_0^2 and the rotation measurements should be uncorrelated.

In Fig. (3.12) we compare the theoretical predictions for the structure functions with the observed RM (shown in Fig. (3.11)). The black line is the result from the observation. In *red* is shown the expected shape for a *Kolmogorov* like spectrum and in *green* one expected from a *Kraichnan* spectrum. As we mentioned, at larger distances the RM should be uncorrelated and therefore have a constant structure function. We show the results for two different parameter sets for the predictions. In dotted lines for $RM_0 = 35 radm^{-2}$ and $l_0 = 18$Kpc and in dashed line for the smaller values $RM_0 = 27$ and $l_0 = 11$Kpc. It is really difficult to flavor any of the phenomenological models. In the case of larger values for the parameters (dotted line), it seems that the *Kolmogorov* like dependence fits better, but if we change the parameters to lower values flavors the *Kraichnan* slope. Note that given the dispersion in the image, and accuracy of the measurements all this parameters are arbitrary chosen. And even if fixed the errors from the measurement makes impossible to distinguish between the models. At scales larger than 60 Kpc we observe the effects due to the shape of our *Faraday* screen, therefore the function gets very irregular.

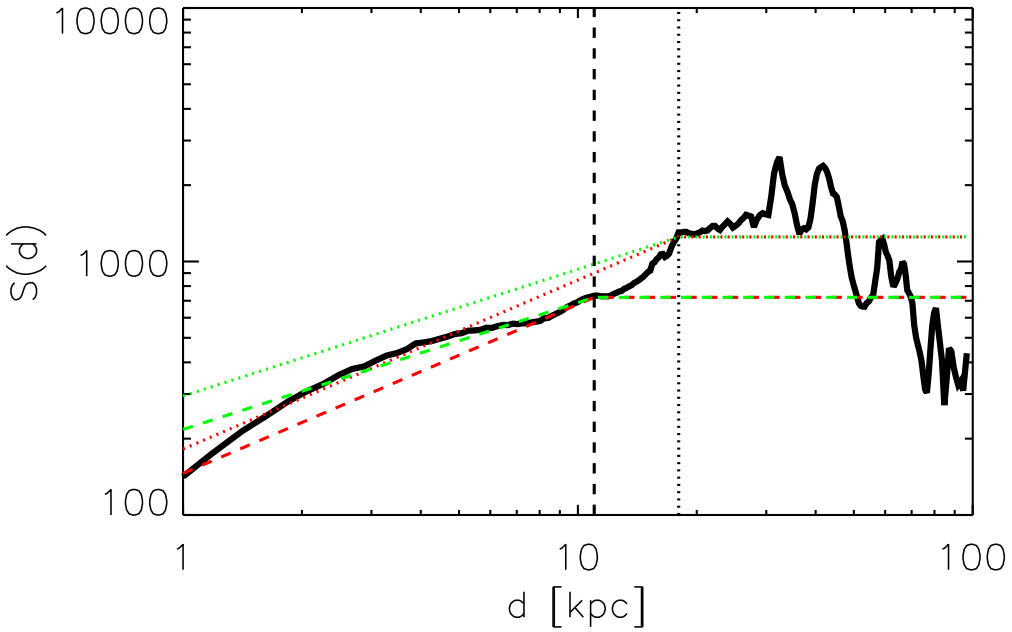

Figure 3.12: Structure functions of the rotation measurement of the observations (shown in Fig. (3.11)) and theoretical predictions. The black line is the result from the observation. In *red* the expected shape for the *Kolmogorov* spectrum and in *green* one expected from a *Kraichnan* spectrum. At larger distances the RM should be uncorrelated and therefore have a constant value. We show two different fittings. In dotted lines, for the parameters $RM_0 = 35\ rad\ m^{-2}$ and $l_0 = 18$ Kpc and in dashed line for the smaller values $RM_0 = 27\ rad\ m^{-2}$ and $l_0 = 11$ Kpc.

Fig. (3.13) shows a comparison of the obtained structure function from the observations (black line) and the simulations. For each simulated cluster we calculated the synthetic rotation measure maps, clipped accordingly to the shape of the observed map. To obtain different realizations of the same simulation we produced nine different maps where we shifted the clipped region by ±20 Kpc in both spacial directions within the original, cluster centered maps. The thick lines mark the mean structure function over these maps, whereas the thin lines show the RMS scatter between the different maps (shown only for one scheme). To be properly comparable with the observations, we scaled up the synthetic maps with the amplitude at large scales, given that at those scales the RM should be uncorrelated. Doing so, the amplitude of the structure function should be the same. Due to the large scatter in the values at large scales we make this normalization averaging in values between 30 Kpc and 100 Kpc The effects of the different implementation will also we reflected in those functions. The most dissipative the scheme will tend to suppress small scale structures, therefore is expected that the *Euler* simulation without the *Lorentz* force should have large values at small d because is only driven by the hydrodynamical turbulence. However, this is not the case it has the same power than the *Dedner*, which is a scheme that takes into account the magnetic pressure of the system.

It is interesting to note that in the *Euler* potential case have the lower power of all the $1x$ simulations. This is due the low final magnetic field, and the small difference between the reversals. For all the $1x$ simulations we have a minimum resolution constrain

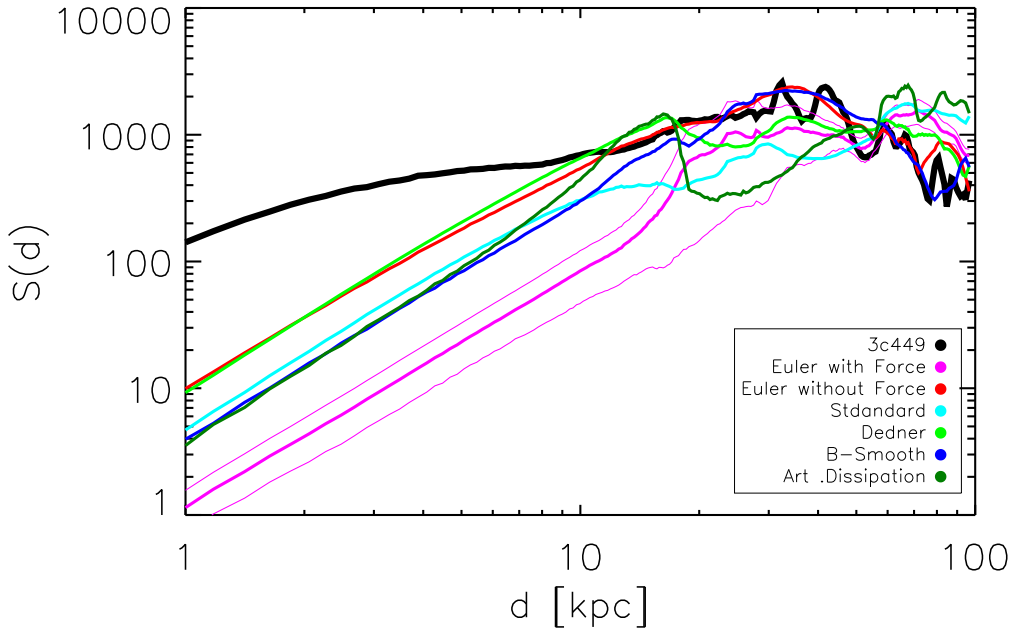

Figure 3.13: Shown are the structure functions (S) calculated from the observed (black line) and from the synthetic Faraday Rotation maps (colored lines) for the different implementations. The thick lines correspond to the mean calculated over 9 realizations of the maps, whereas the thin lines mark the RMS scatter between the different maps (only shown for the *Euler* simulation).

of Hsml $\sim$ 15 Kpc, explaining the different slope compared with the observations for lower radii. Note that the synthetic maps are the result of a projection, where each pixel is the integrate value from several particles, that contributes during the path. This fact allow us to observe the features even a smaller radii than the Hsml, as is shown by the structure function.

In Fig. (3.14) show the effects with resolution. As we already mentioned, increasing the resolution we are able to resolve smaller scales in the RM maps, and this is shown in the functions. We don't observe considerable differences between $6x$ and $10x$, but we see the tendency to better agreement with observations in the internal regions. Although the total magnetic field in both simulations are different, reversals have similar structure, independent of the underlying magnetic strength. Interestingly, the *10x* simulation, seems to match the features at observations at 20 Kpc and the drop at 6 Kpc given by the resolution. We can explain this changes in the slope by considering as transition between different regimes, i.e. from a uncorrelated to a *Kolmogorov*, and then to a *Kraichnan* for small scales. However, given the scatter from the observations and uncertainties from the simulations (remember that this set of simulations were not meant to be compared with any observation in particular), we need more information to arrive to any conlution. However clearly demonstrates that using such advanced scheme together with very high resolution allows to probe the properties of the ICM and comparing synthetic and observed maps one can estimate which physics are more important in the RM phenomena.

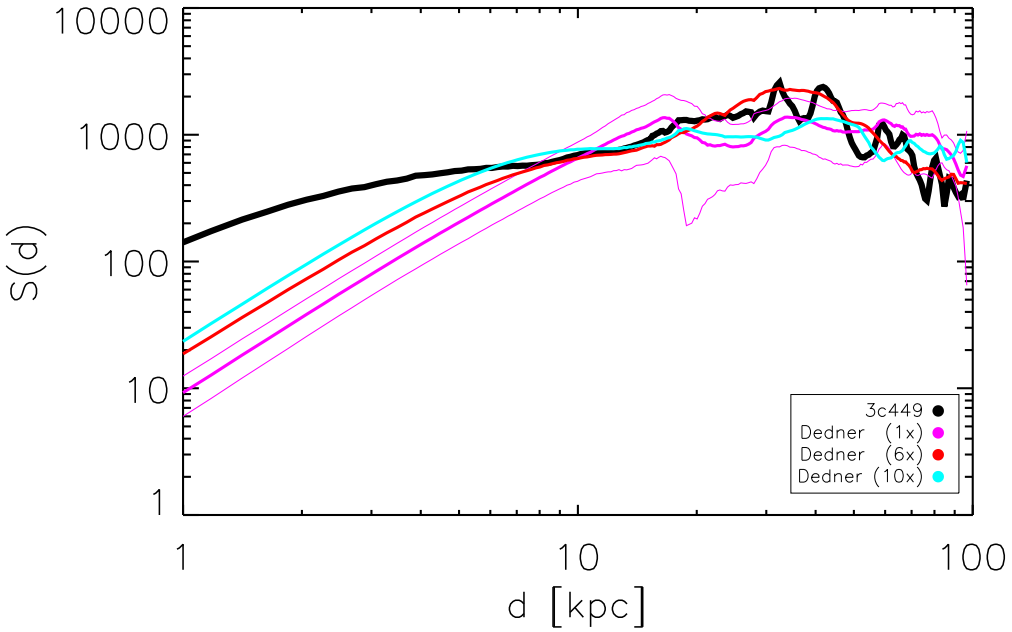

Figure 3.14: Shown are the structure functions (S) calculated from the observed (black line) and from the synthetic Faraday Rotation maps (colored lines) for different resolutions. The thick lines correspond to the mean calculated over 9 realizations of the maps, whereas the thin lines mark the RMS scatter between the different maps (only shown for the *1x* simulation).

3.5 Discussions

We run cosmological simulations of galaxy clusters with different underlying SPH schemes of magnetic field evolution. The magnetic field profiles in the different implementations show similar properties, even in comparison with Eulerian codes.

The main difference comes from the inner region (i.e. $radius < 0.5$Mpc), where the slopes are quite different in each of the methods. In the most dissipative cases, there is a flatter slope due all the losses in the small scale growth. SPH schemes are known to have a less numerical mixing than other schemes. However, inside the smoothing length, there is a intrinsic *softening* of the properties. In schemes as, *Dedner* Cleaning, *Standard* and *Euler* potentials, reconnection occurs at this level, thus, keeping the numerical dissipative processes as low as the scheme permits. The comparison between different schemes and common properties lead us to the conclusion that the non vanishing numerical $\nabla \cdot \mathbf{B}$ terms are not important for the evolution or growth of the magnetic field. But, they help to determine where numerical instabilities can happen, therefore a correct treatment of these quantities is needed. We know, from the successful tests studies (see chapter 2), that we can reproduce the correct properties from the shocks. Exactly the front shock and contact discontinuity are a transient stages between two different ones. Thus, depending on those final stages, temporally can show some numerical inaccuracy that will disappear when the system evolves. The astrophysical case is even more complicated, having a

variety of shocks configurations and possible interactions that are impossible to test [3]. In non-radiative simulations, we found that the numerical MHD implementation is stable enough to properly simulate galaxy clusters in cosmological context, showing that the scheme successfully do not generate or propagates spurious $\nabla \cdot \mathbf{B}$ in our region of interest, and lowering the numerical $\nabla \cdot \mathbf{B}$ errors with increasing resolution as expected.

It is known that the growth of the magnetic field having only the adiabatic collapse as dynamo mechanism is unlikely. One of the reasons is the strong tangling of the field lines, that leads to instabilities and thus a complex morphology of the field (Ruzmaikin, A. A. and Sokolov, D. D. and Shukurov A.M., 1988). An exclusive characteristic of SPH is the adaptivity, thus the particles can follow the properties in different scales. Therefore, the turbulent cascade is well described, integrating correctly the growth of the magnetic field. Note that even without knowing exactly the proper value of the initial magnetic field strength for our simulations, we showed in other works that the astrophysical systems reach an equipartition between the magnetic energy and the turbulent, in accordance with turbulent dynamo theories (Kotarba et al., 2010b).

In the case of *Euler* potentials we stress the fact that this representation lacks from important features in their evolution. This, implies that the structure represented afterwards is mostly driven by turbulent motions and a magnetic pressure term. The final field obtained is related to the stochastic events that derives the field to that particular configuration, but the causality from the previous time steps is not followed properly. In the case without the back reaction from the magnetic field (i.e. *Lorentz* force), the final field structure is build by the advection of the Euler potentials to the final configuration completely driven by the hydrodynamical turbulence. In this case the final magnetic field is higher than the ones that take into account the magnetic force. The $\nabla \cdot \mathbf{B}$ errors in both cases are similar because they are constraint by numerical precision of the building up each time step. The lack of reconnection, characteristic from *Euler* potentials, is shown in the fact that the magnetic field is accumulated in the center, but does not grow as in the induction cases.

In the case of smoothing the magnetic field at the point we smooth the field we break the idealisation of the MHD and let the field diffuse with the surroundings. The same principle applies to Dissipation. A numerical dissipation is difficult to translate to a determined physical diffusion value, because they depend on different local properties[4] making comparisons and predictions more complicated.

When we study synthetic RM maps we can see how the reversals scales in the dissipation and smoothing case are extreme. They are represented by just a few big reversals zones of the orders of ~ 100 Kpc. In the other cases, there are more zones, with sizes relatives to of the order ~ 10 Kpc, which is closer to the values from observations. Additionally the dissipative cases, the magnetic field is propagated far away from the cluster center, which is difficult to constrain by observations.

From simple isotropic turbulent theories, one can try to estimate the shape of the structure functions. However, when comparing theory with observations, we are not able to distinguish between models, because the uncertainties in observations. When we study the structure functions of the synthetic maps, we observe that in general we can't reproduce the features in observations at all scales, but we confirm a trend to the observed results when we increase the resolution. This comparison between observations

[3] At most we can test different shocks families as done in section 2.4.

[4] Being the signal velocity for the numerical case and resistivity on the physical one.

and high resolution simulations, suggests that the physics may be described by a multi scale turbulence model. The improvements in observations and numerical power in the next years will allow us to constrain different features in the structure function, and build a compressive model for the physics involved at different scales.

We clearly demonstrates that using advanced SPH MHD schemes together with very high resolution allow to probe the properties of the ICM. More effects that can help to steer-up the inter-cluster medium, therefore helping to generate turbulence and/or power in the magnetic field structure function in different scales. Additionally we show that comparing synthetic RM maps with observations can be used to estimate which physics are relevant to understand the underlaying phenomena, contributing to the global picture of the galaxy cluster physics.

Chapter 4

Large Scale cosmological magnetic fields

I was thinking the day most splendid till I saw what the not-day exhibited, I was thinking this globe enough till there sprang out so noiseless around me myriads of other globes.

Night on the Prairies - Walt Whitman (1819-1892)

4.1 Introduction

Recently an interesting attempt to constrain the value of large scale cosmic magnetic fields was done by Lee et al. (2009). These authors detected a positive cross-correlation signal between the distribution of galaxies from the SDSS Sixth Data Release (Adelman-McCarthy et al., 2008) and the RM values extracted from the Taylor et al. (2009) catalog. Statistical tools, as the correlation functions, demonstrated to be sufficient show a positive signal due to the RM quality constrains, increasing the signal to noise ratio (see section 1.4). Using the amplitude of the correlation signal, together with a simplified model for the magnetic fields configuration in the Universe (estimated from its mean electron density), let us to calculate the typical RM values expected from this coherent field in a given length scale. In this way they were able to derive limits for the corresponding cosmic magnetic fields, at scales where it is difficult to infer the magnetic fields strengths from other methods.

In this scene we investigated: (*i*) to what extent a self-consistent treatment of the cosmological RM signal based on magneto-hydrodynamical (MHD) simulations of structure formation changes the expected shape and amplitude of such a correlation signal, and (*ii*) how such an approach is affected by the presence of the Galactic foreground (GF) and noise in the final RM signal. Both points are of extreme importance, if robust field properties are to be derived from any observed signal. Furthermore, the appearance of magnetic field reversals (as observed in galaxy clusters at various length scales) will alter the cosmological signal magnitude and shape, whereas the residuals of any foreground and measurement errors will bias the relation between the amplitude of the correlation function and the underlying cosmological field. In order to self-consistently treat cosmic magnetic fields, we make use of several cosmological MHD simulations which compute the resulting magnetization of the cosmological structures (e.g. amplitude and structure) following different models for the origin and seeding process of such magnetic fields. We

also construct magnetic field models with much higher magnetization amplitude in the low density regions to test how the resulting signatures of more extreme models affect our results. Here we scale up the predicted amplitude of the magnetic field in filaments by several orders of magnitude to test if such strong magnetic fields in low density regions significantly effect the expected correlation signal. By introducing GF and adding noise to the signal on top of the underlying cosmological signal, we can study how the shape and amplitude of the cross-correlation function would be modified when considering actual observations. To avoid further complications we ignore the cosmological evolution of magnetic fields, which, in principle, would be consistently treated within our cosmological MHD simulations. Hence, we neglect the evolution of the cosmic magnetic field seen in the simulation as a result of the structure formation process, and assume the present day magnetization of the simulated universe to be present up to the redshift of the sources.

This chapter is organized as follows. In Section 4.2 we describe the cosmological MHD simulations used and how we compute the synthetic RM catalogs. In section 4.3 we discuss the cross-correlation estimators used, the estimation of the intrinsic uncertainties due to the limited number of lines of sight probing the magnetization of the cosmological structures, the different signals expected for the various magnetization of the universe, as well as the uncertainties induced by the redshift distribution of the sources. In section 4.4 we show how the shape and amplitude of the signal is affected by the recipe normally used to remove the foreground signal, due to observational noise and to the Galaxy itself. In section 4.5 we summarize the combination of all the effects, and present the resulting observable signal of the different magnetic field models. Finally, our conclusions are given in Section 4.6.

4.2 The Simulations

4.2.1 The cosmological MHD simulations

We used results from one of the constrained, cosmological MHD simulations presented in Dolag et al. (2005a) and Donnert et al. (2009). In both simulations, the initial conditions for a constrained realization of the local Universe were the same as used in Mathis et al. (2002). The initial conditions were obtained based on the the *IRAS* 1.2-Jy galaxy survey (see Dolag et al., 2005a, for more details). Its density field was smoothed on a scale of 7 Mpc, evolved back in time to $z = 50$ using the Zeldovich approximation, and used as an Gaussian constraint (Hoffman and Ribak, 1991) for an otherwise random realization of a ΛCDM cosmology ($\Omega_M = 0.3$, $\Lambda = 0.7$, $h = 0.7$). The *IRAS* observations constrain a volume of ≈ 115 Mpc centered on the Milky Way. In the evolved density field, many locally observed galaxy clusters can be identified by position and mass. The original initial conditions were extended to include gas by splitting dark matter particles into gas and dark matter, obtaining particles of masses 6.9×10^8 $M_\odot$ and 4.4×10^9 $M_\odot$ respectively. The gravitational softening length was set to 10 Kpc.

The magnetic field was followed by our MHD simulations through the turbulent amplification driven by the structure formation process. For the magnetic seed fields, the first simulation (labeled *MHD*) followed a cosmological seed field (see Fig. 4.1), while in the second (labeled *MHD Gal*) used a semi-analytic model for galactic winds. In particular, we considered the result of the *0.1 Dipole* simulation from Donnert et al. (2009). In both simulations, the resulting magnetic field at $z = 0$ reproduce the observed

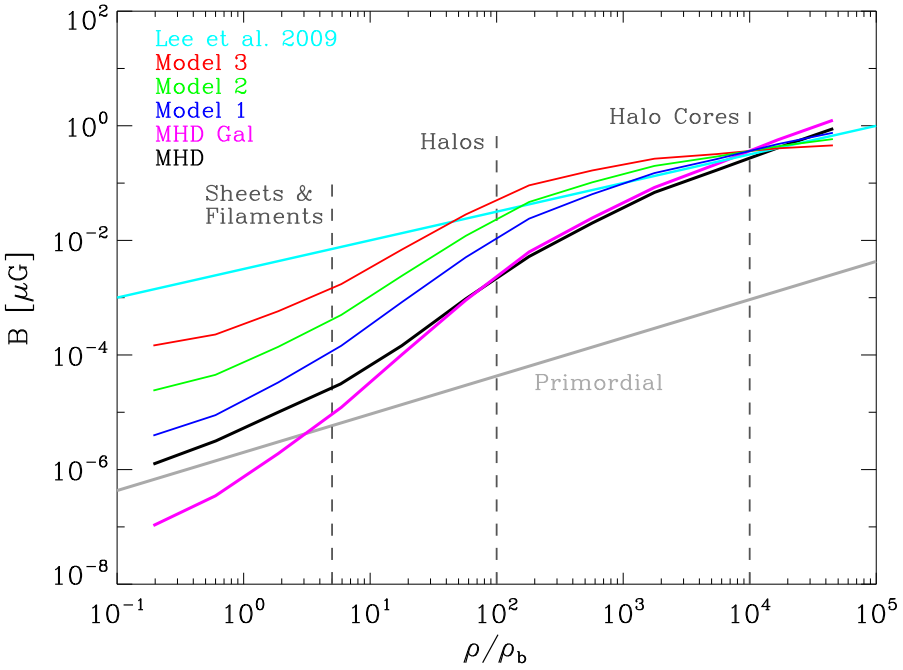

Figure 4.1: Mean cosmic magnetic field as a function of density (in units of the mean cosmic baryon density) obtained from two, fully self-consistent, cosmological MHD simulations for different magnetic field origins (*MHD* and *MHD Gal*), as well as three models, where we artificially scaled-up the magnetic field intensity at low densities to obtain scenarios with extreme values in filaments (*Model 1*, *Model 2* and *Model 3*). For more details on these models see the text. Additionally, the primordial seed fields of the *MHD* simulation and that obtained by Lee et al. (2009) are shown.

Model	$\overline{\lvert RM \rvert}_{z=0.03}$ [rad m^{-2}]	$\Delta\overline{\lvert RM \rvert}_{z=0.03}$ [rad m^{-2}]	$\overline{\lvert RM \rvert}_{z=0.52}$ [rad m^{-2}]	$\Delta\overline{\lvert RM \rvert}_{z=0.52}$ [rad m^{-2}]	$\overline{\lvert RM \rvert}_{z=1.03}$ [rad m^{-2}]	$\Delta\overline{\lvert RM \rvert}_{z=1.03}$ [rad m^{-2}]
MHD Gal	0.025	0.010	0.12	0.05	0.21	0.09
MHD	0.018	0.010	0.09	0.05	0.15	0.09
Model 1	0.018	0.008	0.09	0.04	0.15	0.07
Model 2	0.025	0.010	0.12	0.05	0.21	0.09
Model 3	0.040	0.013	0.20	0.06	0.34	0.11

Table 4.1: Mean and standard deviations of RM absolute values for the different catalogs at $z = 0.03$ and estimates for $z = 0.52$ and $z = 1.03$. The catalogs were constructed in each case using four different realizations (see text). *MHD* is our fiducial structure formation model. *Models 1, 2* and *3* are its scaled-up versions. *MHD Gal* includes a semi-analytic model for Galactic winds to seed magnetic fields at $z = 4.1$.

rotation Measure in galaxy clusters very well. A visual impression for the magnetic field within the two different simulations and their corresponding galaxy distribution is shown in Fig. 4.2.

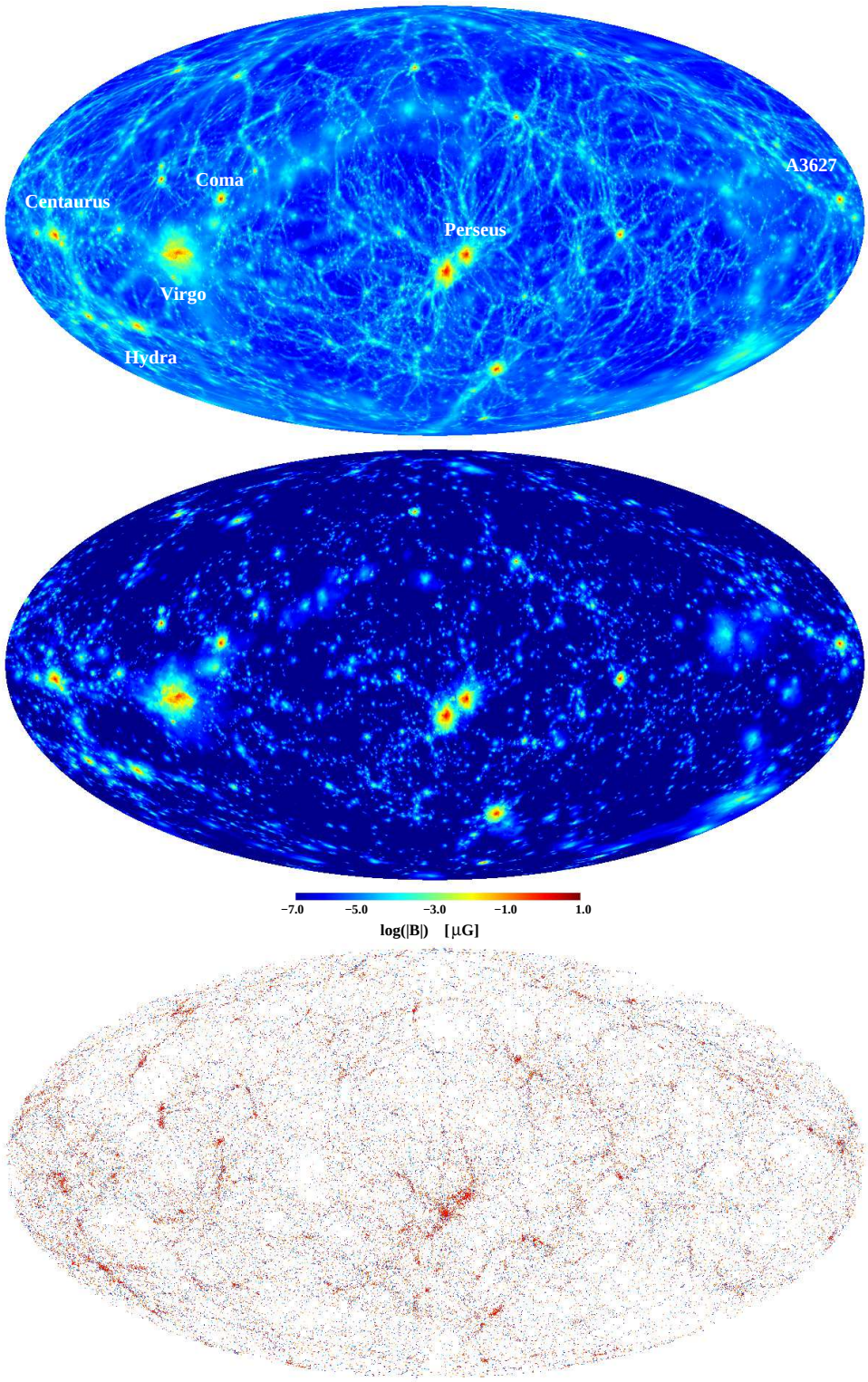

Figure 4.2: Full sky maps of the local universe in super-galactic coordinates for the projected magnetic field in the *MHD* run (upper panel) and in the *MHD Gal* run (middle panel). The galaxy distribution expected from the corresponding hydrodynamical run is shown in the bottom panel. Galaxies are colour-coded from blue to red using their $B-V$ colors ($0.3 < B-V < 1$; see Nuza et al. (2010).

4.2.2 Artificial MHD models

As is clearly visible in Fig. 4.2, such cosmological simulations usually predict relatively low magnetic fields in low density regions. To explore more extreme models, we scaled-up the magnetic field of the *MHD* simulation by a factor

$$B_{1,2,3} = B_{\rm MHD} \times \left(\frac{\rho}{\rho_{\rm scale}} \right)^{\alpha}, \tag{4.1}$$

with α being 1/3 (*Model 1*), 1/2 (*Model 2*) and 2/3 (*Model 3*). Here $\rho_{\rm scale}$ denotes density scale for fixing the magnetic field, which we choose to be 10^4 times the mean cosmic baryon density. The resulting behavior of the mean magnetic field as a function of baryon density for the original runs, as well as for the scaled-up models, are shown in Fig. 4.1. Note that the lines shown reflect the mean value of the magnetic field at the corresponding over density, while the dispersion of its amplitude can span several orders of magnitude in each density bin (see Dolag et al. 2005). The ratio between the magnetic and kinetic energy in the simulations is on average at the percent level, which results in a magnetic field counterpart at least 2 orders of magnitude below the equipartition value, meaning that the magnetic field is not dynamically important, even in cluster cores. It stays below equipartition also for the models where the magnetic field is scaled up, with the exception of *Model 3*, where the magnetic field nearly reaches equipartition in the cluster outskirts. We want to stress that such scaled-up magnetic fields are artificial models, as the primordial field needed to generate them would be well above current cosmological constraints (e.g. from CMB). Such strong seed fields would lead to an over-prediction of the magnetic field amplitude in galaxy clusters by the simulations and it is quite unclear which physical process could be responsible to avoid this. We also remark that the scaled-up models lead to slightly lower central values for the magnetic field inside of galaxy clusters. Donnert et al. (2010) show a direct comparison of observed magnetic field radial profiles and simulations, in particular they consider a similar scaled-up version of the magnetic field than *Model 2* used in this work. This is qualitatively in agreement with what is needed to fit the observed RM signal within the Coma galaxy cluster (see Bonafede et al., 2010).

4.2.3 Synthetic RM catalogs

For each of the 5 models, we construct full sky RM catalogs, sampling the whole sky using 3072 different lines of sight (i.e. $\sim 3^\circ$ resolution) making use of the HEALPix (Górski et al., 2005) tessellation of the sphere. Therefore, our RM catalog contains roughly half as many number of lines of sight to probe the RM signal of the large scale structure than the catalog used as Lee et al. (2009).

Although we are only reproducing much shorter lines of sight than expected in the real Universe (due to the limited volume of the underlying simulation) we believe that the region probed reflects a fair representation of the present large scale distribution of galaxies (Nuza et al., 2010), and therefore, we do not expect the amplitude of any normalized correlation signal to be strongly affected by a lack of fluctuation power.

4.2.4 Magnetic depth of the universe

On its way to the observer, the polarized radio emission of the observed sources will pass several times through the cosmological filamentary structures. The final RM value does accumulates in a random walk. Examples of the magnetic field structure along some lines of sight through the simulated local universe can be found in previous work as Fig. 12 in Dolag et al. (2005a) or Fig. 10 in Dolag and Stasyszyn (2009). The magnitude of the observed RMs, and thus, the mean of the RM absolute values, will strongly depend on the *magnetic depth* (given by the redshift range probed) accessible to the observed sample of radio sources. In addition, if the magnetic field changes during the formation of the universe, such changes have to be convolved with the redshift distribution of the observed sources. For simplicity, we assume that the magnetization of the universe at the time of interest was the same as today and that all sources towards the RMs are measured at the same redshift, e.g. all lines of sight used probe the same *magnetic depth* of the universe.

Unfortunately, our cosmological MHD simulation is much smaller than is required to compare with observations directly and therefore we have to extrapolate our calculated RMs to the redshift of the real observed sources. With the size of our simulation box, we can probe only out to $z = 0.03$. Because of this, we account for the increase of the RM values due to a random walk process towards higher redshift by assuming the same contribution of cosmic structures to estimate the cosmological RMs. This is done by replicating the original volume 15 and 22 times (corresponding to redshifts out to $z = 0.52$ and $z = 1.03$). As shown in Table 4.2.1, the associated RM amplification factors, including the shift of the rest-frame frequencies due to the cosmological expansion for each replication of the box, are 4.97 and 8.54 respectively. We will use such expected amplified RM signals in the following analysis, indicating this by adding the redshift used for the *magnetic depth* together with the model name. Note that to increase the RM signal by a factor of 100 one must probe cosmic structures up to $z \approx 8$.

Even for the extreme scaled-up models and extrapolation out to $z = 1.03$, the expected RM signal is still one order of magnitude smaller than the reported value by Lee et al. (2009) in their simplified model (i.e. $|\mathrm{RM}| \approx 2$ rad m^{-2}). This emphasizes the fact that simulations which properly take the cosmological structures into account are needed to relate any possible correlation signal to global magnetic field values. Note also that such small signals are expected to be very sensitive to measurement errors which will scale with the even much larger foreground signal imposed by our galaxy. We explore these problems in the following sections.

4.3 Evaluating the cosmological Cross-Correlation Signal

4.3.1 Estimators

We compute the cross-correlation signal between the RM computed along 3072 lines of sight using a HEALPix tessellation of the sky and the angular positions of simulated galaxies. For every direction, we count the number of galaxies lying at an angle between θ and $\theta + d\theta$, weighting the counts with the corresponding absolute RM value. Formally, the cross-correlation function between |RM| and the galaxy density n is defined as follows

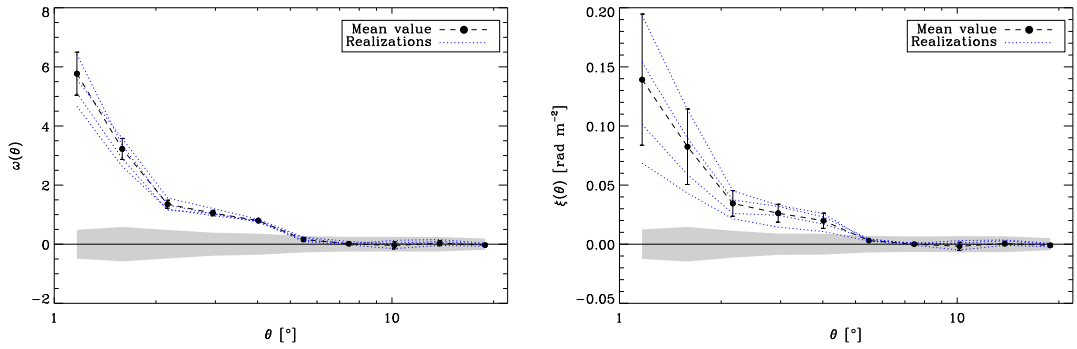

Figure 4.3: Angular cross-correlation functions, for the full sky map based on the original *MHD Gal* simulation, using the two estimators presented in the text (see Eqs. 4.2 and 4.3). In both panels, the results of different magnetic field realizations can be seen as blue dotted lines. The average result is shown as black filled circles. Error bars denote the 1-σ dispersion due to the different realizations. The Grey area indicates the *null* signal obtained by reshuffling the RMs.

$$\omega_{\rm RM}(\theta) \equiv \frac{\langle \Delta n(\theta) |{\rm RM}| \rangle}{\bar{n}\overline{|{\rm RM}|}}, \tag{4.2}$$

where Δn measures the fluctuations around the mean value of n, $\bar{n}$ is the mean density of the galaxy sample, $\overline{|{\rm RM}|}$ is the mean of the $|{\rm RM}|$ catalog, and $\langle \ldots \rangle$ denotes ensemble average. If the distributions of n and RM are Gaussian, this estimator is insensitive to the addition of an uncorrelated signal (like noise and/or foreground). While for the galaxy density n a Gaussian distribution is still a reasonable assumption, the RM absolute values are strongly non-Gaussian. Therefore, it cannot be easily predicted how this estimator will behave once the observational process is included. In fact, Lee et al. (2009) used a different estimator, where the normalization by $\overline{|{\rm RM}|}$ is not evaluated, i.e.

$$\xi_{\rm RM}(\theta) \equiv \frac{\langle \Delta n(\theta) |{\rm RM}| \rangle}{\bar{n}}. \tag{4.3}$$

Note that this estimator is likely quite sensitive to processes which change the value of $\overline{|{\rm RM}|}$, such as the *magnetic depth* probed by the redshift distribution of the sources.

4.3.2 Evaluating uncertainties

We investigate two types of errors for our simulated cross-correlation functions. To estimate the significance of our obtained correlation signal, we shuffled the RM data twenty times. By doing this, we randomly change the direction of the lines of sight, while keeping the value distribution. This procedure guarantees that the synthetic RM values and the simulated galaxy distribution will be uncorrelated, while keeping the mean value of the RM non-Gaussian distribution unchanged. As a consequence, the average value of the different realizations will correspond to the *null* signal.

This allow us to take into account the variance given by the used sampling and reveals the significance of the correlation itself. We will indicate this as the expected level for a *null* signal in the figures. A second source of errors is given by the magnetic field realizations available inside the simulated volume. Since we are still using a small number

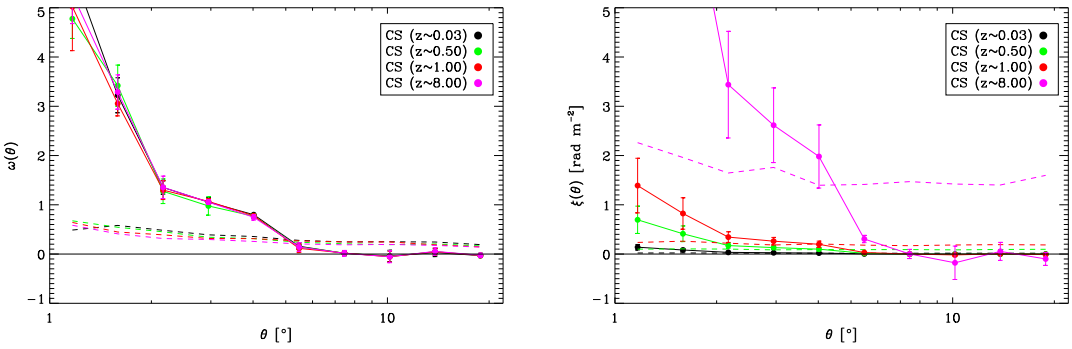

Figure 4.4: Angular cross-correlation function, based on the original *MHD Gal* cosmological signal (CS), evaluated for different *magnetic depths* probed by the RMs, using the two estimators presented in the text (left and right panels).

of RM points (i.e. 3072), this also introduces significant noise to the correlation functions obtained. It is beyond the scope of the present work to produce several independent simulations based on different realizations of the initial magnetic seed field. Therefore, we assessed this by calculating the RM signal of each particle using either the x, y and z component or the radially projected magnetic field component. Note that the first three components are only statistically equivalent to the radially projected component once a isotropic distribution of the magnetic field is assumed. Next we use these four realizations of the RM signal to estimate the uncertainty according to the underlying cosmic magnetic field realization in the simulations. This uncertainty is then added as error bars to the individual models.

Fig. 4.3 shows the correlation function signal obtained from the *MHD Gal* model for the two estimators ($\omega_{\rm RM}$ and $\xi_{\rm RM}$). It shows the individual signal for the four different realizations of the magnetic fields and the resulting mean signal with their corresponding error bars. The *null* signal obtained from reshuffling the RMs twenty times is indicated by the grey area. Whereas the uncertainties coming from the magnetic field variance in the different realizations changes the amplitude of $\omega_{RM}(\theta)$ only by 10%, it is clearly visible that using the unnormalized $\xi_{RM}(\theta)$ estimator introduces much larger uncertainties in its amplitude (by roughly a factor ~ 2). It also highlights the fact that using this estimator together with the mean of the |RM| signal to infer the underlying magnetic field will generate large uncertainties in the estimation. It is important to keep in mind that the ratio between both estimators (in every scale) for each of the individual realizations is given by the mean value of the corresponding absolute RMs. However, the normalization of the different realizations of each magnetic field model can vary significantly (up to a factor of ~ 3). Whereas in the normalized cross-correlation this is naturally absorbed, in the unnormalized case it enters in the error bars when building the assembly average over different realizations.

As a final remark, we expect that both errors will decrease similarly as Poissonian errors do when the number of lines of sight to probe the RM signal is increased.

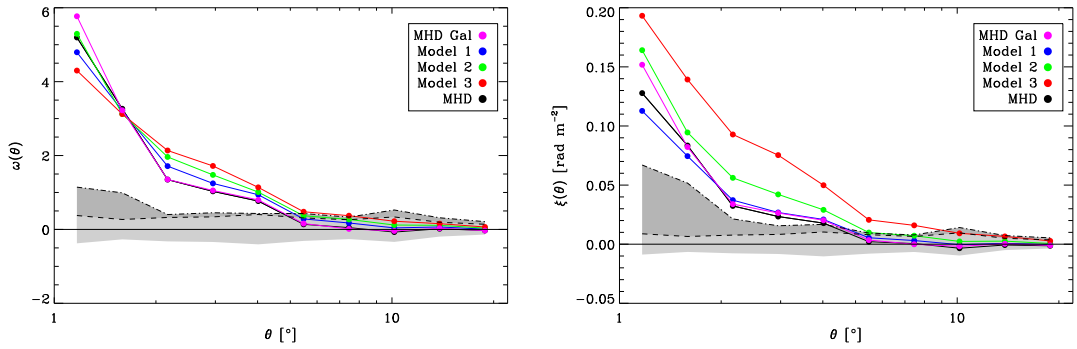

Figure 4.5: Comparison between the angular cross-correlation functions, for the full sky maps in different models, using the two estimators presented in the text (left and right panels). Black solid line indicates the *MHD* model, while blue, light green and red indicate *Model 1, 2* and *3* respectively. Pink solid line indicates the *MHD Gal* model. In both panels, the light Grey shaded area indicates the randomly shuffled region, while the dark Grey area indicates the magnitude of typical errors present at a given scale due to the different RM realizations.

4.3.3 Magnetic depths

As mentioned before, to correctly interpret the cross-correlation signal we must consider the *magnetic depth* probed by the RMs. Fig. 4.4 shows the expected signal, assuming a non-evolving magnetic field probed by the sources up to a certain given redshift. As expected, the normalized correlation function signal $\omega_{RM}(\theta)$ is insensitive to the particular probed volume and its amplitude reflects the underlying magnetic field distribution, independent on the redshift distribution of the sources. On the other hand, the signal given by the unnormalized estimator $\xi_{RM}(\theta)$ increases as a function of the *magnetic depth* as expected. In this case, the amplitude changes by more than a factor of two if the redshift distribution of the radio sources is changed from $z = 0.52$ to $z = 1.03$. This means that one has to consider the redshift distribution of the radio sources towards the observed RMs in order to relate the amplitude of the signal to the underlying magnetization of the large scale structures. Therefore, it is difficult to interpret such an observed signal (as done e.g. by Lee et al., 2009).

4.3.4 Magnetic field models

Fig. 4.5 shows the cross-correlation function signal obtained from the five different models investigated. The two shaded regions indicate the contribution of the two errors discussed before. The shape and the ordering of the correlation signal of ω_{RM} reflects the scaling of the underlying magnetic field models with density. In particular, the crossover of the correlation function reflects the one seen in the underlying magnetic field models very well (see Fig. 4.1). The correlation signal thus indeed carries information about the strength and distribution of the cosmic magnetization. It is expected that using more lines of sight will reduce the statistical errors enough to make our extreme models clearly distinguishable. This would be in principle possible with the available number of line of sights in current data (e.g. Taylor et al., 2009).

The unnormalized correlation function ξ_{RM} leads to a larger relative change of the amplitude of the correlation signal for the different magnetic field models, especially for

the ones with very high magnetic fields in filaments. However, the resulting signal comes with much larger errors (coming mainly from the different magnetic field realizations in the same models) and is therefore less significant. Also, the ordering of the magnetic field models with less extreme magnetic field values in filaments is not longer reflected in the correlation amplitude, particularly towards smaller impact parameters.

In summary, we conclude that the correlation signal for ω_{RM} inherits a clear signal from the cosmological magnetization, whereas the correlation function ξ_{RM} (as used in Lee et al., 2009) is very difficult to interpret. Because of the missing normalization, changes in the underlying RM distribution (caused by different realizations of the same magnetic field model or the *magnetic depth* probed by the radio sources) are not compensated for.

4.4 Simulating the observational process

To test for the effects caused by the observational process on the cross-correlation functions it is important to use an underlying scenario which reflects the expected amplitude of the RM signal. Therefore, we use (unless specifically stated) an underlying *magnetic depth* of the universe of $z = 1$.

4.4.1 Foreground removal procedure

For RM observations, the removal of the foreground imposed by our galaxy is a major problem. Usually one assumes that the foreground varies on (much) larger scales than the ones of interest and removes the GF by subtracting a smoothed signal from the original data. Here we test how such a removal procedure affects the underlying cosmological signal traced using correlation functions following exactly the same procedure applied in Lee et al. (2009). At every point, we subtract the mean of the RM absolute values within a given radius (excluding the central value). Specifically, we tested three different angular sizes for the removal (i.e. 3°, 6° and 9°). Fig. 4.6 shows the result of such foreground subtraction technique on the normalized correlation function for the cosmological signal using the normalized estimator ω_{RM}. At small distances, this procedure leads to a significant suppression of the correlation signal, even up to a factor of ~ 2 for angular distances below $\sim 2°$, almost independently of the size of the removing radius. At larger distances, the amplitude of the correlation function is slightly increased ($10 - 20\%$) starting from scales larger than the smoothing radius.

4.4.2 Adding observational noise

Another problem for the observed RMs are the measurement errors by themselves. For example, since the data recently published by Taylor et al. (2009) is based on only two different frequency bands the resulting RMs will be affected by a significant uncertainty. We also note that these errors are not reduced by the smoothing involved when removing the foreground. The typical error of the observational RMs (as inferred from comparison with a data subset which was observed at more frequency bands) turns out to be around 10 to 20 rad m^{-2} (see Taylor et al., 2009, Fig. 2). In order to estimate the effect of the observational errors, we added random values to our simulated RM signal, which were drawn from a Gaussian distribution with a dispersion given by $\sigma_{\rm RM}$. We explored values

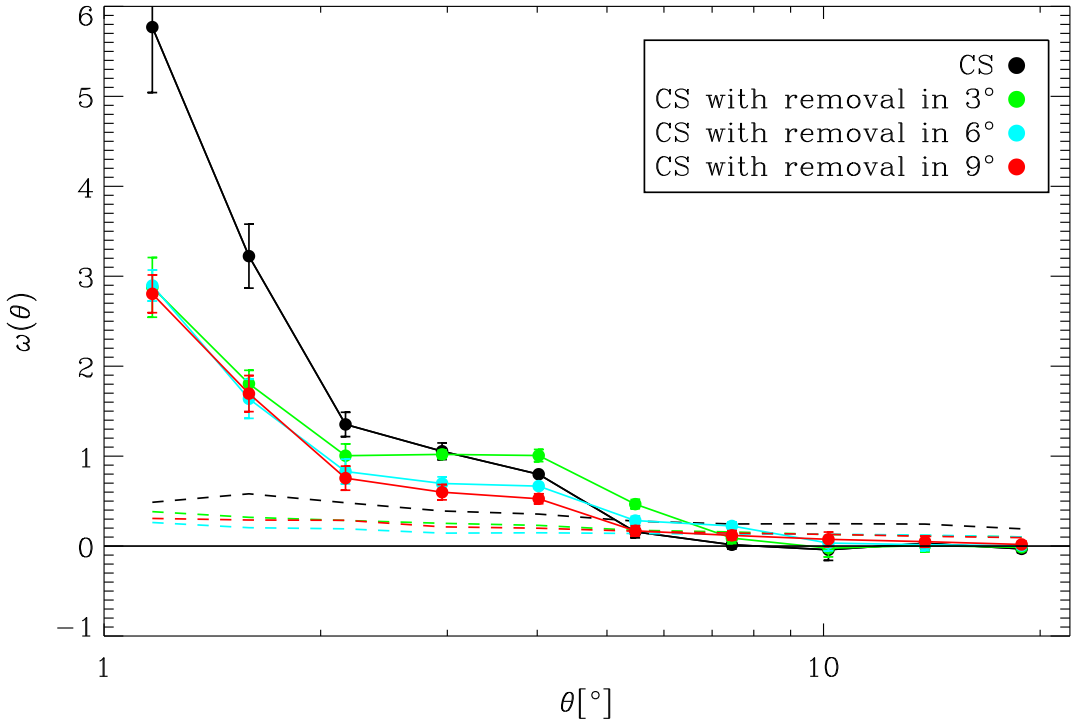

Figure 4.6: Angular cross-correlation function, based on the *MHD Gal* cosmological signal (CS), assuming a magnetic depth of $z = 0.03$. Shown are the results obtained by subtracting to each |RM| the average of its neighbors (excluding itself) within a radius of 3°, 6° and 9° for the ω_{RM} estimator.

of 0.001, 0.01, 0.1, 1.0 and 10 rad m^{-2} for $\sigma_{\rm RM}$. Note that most of these values are much more optimistic than what is expected from current instruments. However, future instruments, like e.g. SKA and ASKAP will achieve an RM accuracy of a few rad m^{-2} (Beck and Gaensler, 2004).

Fig. 4.7 shows the impact of such measurement errors onto the resulting correlation function. Even $\sigma_{\rm RM} = 0.01$ (e.g. a hundredth of the actual measurement error) leads to a sizable (ca. 50%) reduction of the correlation signal. Furthermore, $\sigma_{\rm RM} = 0.1$ (e.g. ten percent of the actual measurement error) reduces the signal by a factor of ~ 5 and $\sigma_{\rm RM} = 1$ (e.g. nearly the present measurement errors) makes the correlation very close to the one of the corresponding *null* signal. From this it is clear that using the normalized estimator $\omega_{RM}(\theta)$ will be quite problematic. The presence of even small measurement errors (far smaller than what can be reached currently) will affect the shape and amplitude of the correlation function in a way that the information on the cosmic magnetization is basically lost.

4.4.3 Adding Galactic foreground

In recent years, different models for the Galactic magnetic field were proposed (e.g. Han et al., 2006; Page et al., 2007; Jansson et al., 2008; Sun et al., 2008). To estimate the influence of the GF on the cosmological cross-correlations we produced a synthetic map of the RM signal expected for our galaxy using the publicly available code HAMMURABI

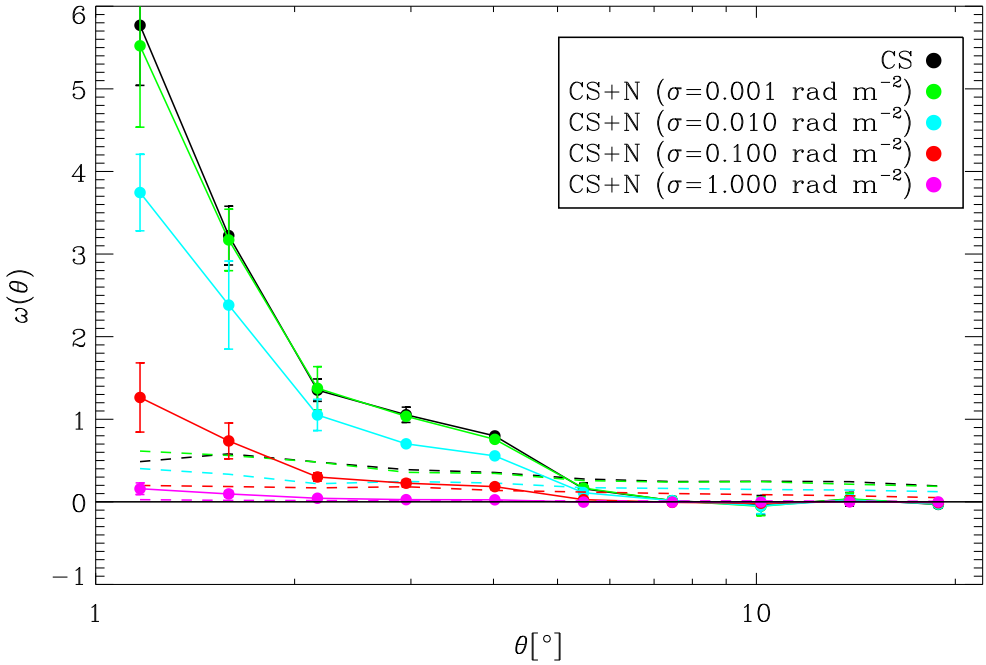

Figure 4.7: Angular cross-correlation function for the *MHD Gal* cosmological signal (CS) using the ω_{RM} estimator. Same as Fig. 4.3 (left panel), but including the effects of different random noise (N) scenarios at magnetic depth of $z = 0.03$.

(Waelkens et al., 2009), where we made use of the Galactic magnetic model given by Sun et al. (2008). The original model was constructed to give a good representation of the synchrotron emission of the Milky Way but, by missing possible reversals within the model magnetic field, it overproduces the RM signal by a significant factor. We therefore scaled the original model down to obtain a better representation of the observed RMs. We also note that such reversals could lead to significant small scale structures in the RM signal due to the GF, as shown by Sun and Reich (2009). Such fluctuations could significantly compromise the cosmological signal, as they would be present on scales smaller than the one used to filter the GF. However, we do not currently include this effect in our foreground model.

In Fig. 4.8 we show the obtained RM map models (left column) compared to the observed RM signal (right column) taken from Taylor et al. (2009). From top to bottom we show the original GF model with noise and the RM data-set, a smoothed version of the maps (within 8°), and the residuals when applying the foreground subtraction as described above for 3°. All the synthetic maps are imprinted with an observational error of $\sigma = 10$ rad m^{-2}. The last row shows the synthetic residual map when reducing the noise level to $\sigma = 1$ rad m^{-2} as expected for future instruments. The close-ups show the remaining signal of prominent galaxy clusters in the residual maps. Note that the signal of other prominent clusters, lying behind the Galactic plane, are not longer visible after the foreground subtraction was applied. As expected, when adding such a large, plain foreground signal to the cosmological one, the cross-correlation function vanishes. Therefore, we also applied the GF removal technique described before. The results can be

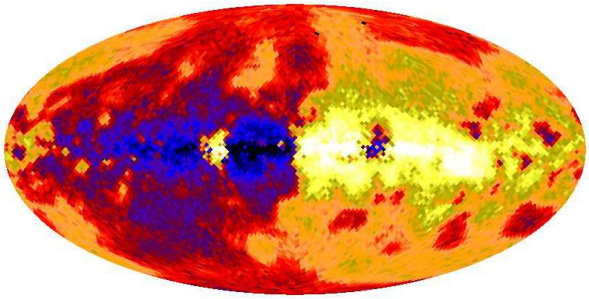

(a) CS+GF+N($\sigma = 10.0$ rad m^{-2})

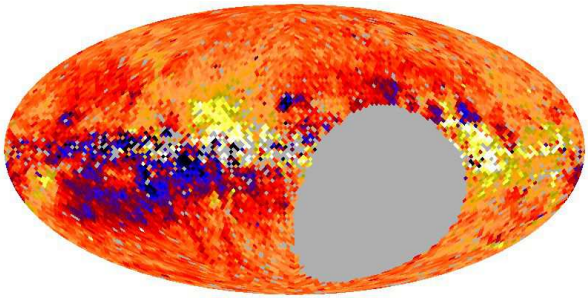

(b) RM data

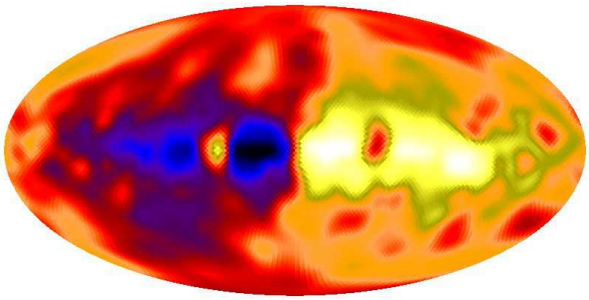

(c) CS+GF+N($\sigma = 10.0$ rad m^{-2}) smoothed in 8°

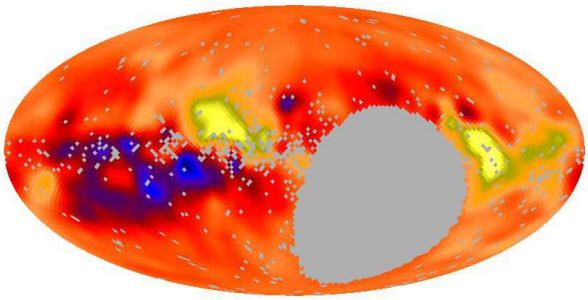

(d) RM data smoothed in 8°

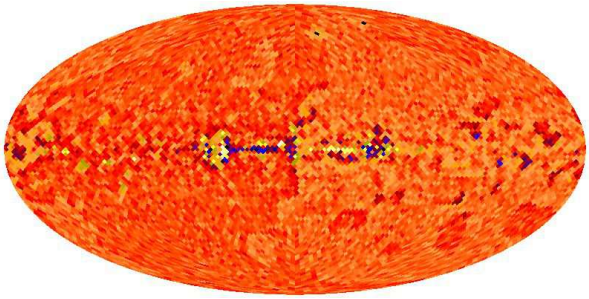

(e) CS+GF+N($\sigma = 10.0$ rad m^{-2}) with GF removal in 3°

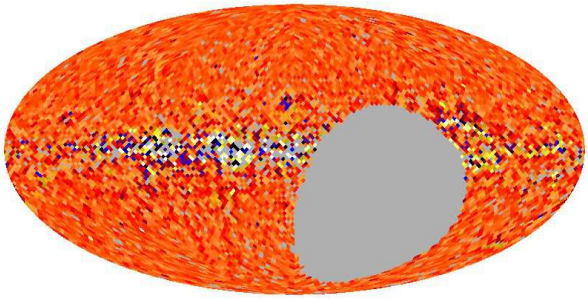

(f) RM data with GF removal in 3°

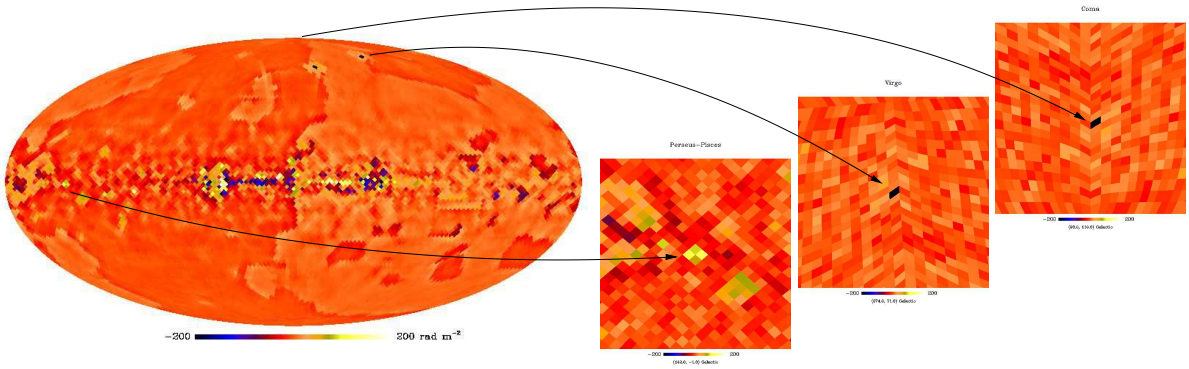

(g) CS+GF+N($\sigma = 1.0$ rad m^{-2}) with GF removal in 3°

Figure 4.8: Full sky maps in galactic coordinates for the total synthetic signal (left column) and for the observed RMs (right column). The first row shows the Galactic foreground (GF) map generated with the HAMMURABI code of Waelkens et al. (2009) including the cosmological signal (CS) from the *MHD Gal* simulation with a *magnetic depth* of $z = 1$ and an imprinted observational error (N) of $\sigma = 10$ rad m^{-2} compared with the plain RM data given by Taylor et al. (2009). The second row shows the same maps but smoothed by 8° (as in Fig. 4 of Taylor et al., 2009) and the third row shows the resulting residual maps when foreground removal is applied (within 3°). The lower left plot shows the former synthetic map where the noise was reduced to $\sigma = 1$ rad m^{-2}, as it is expected for future observations. In the lower right we show $40° \times 40°$ wide close-ups of three prominent clusters in the simulation (from left to right: Perseus-Pisces, Virgo and Coma).

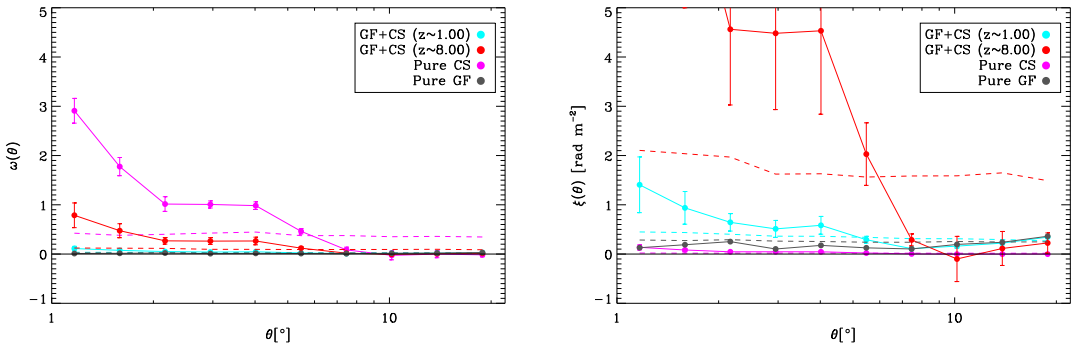

Figure 4.9: Angular cross-correlation function for the combined cosmological signal (CS) from the *MHD Gal* simulation and the Galactic foreground (GF), including the foreground removal in 3° as described in the text. Shown is the signal using both estimators as presented in the text (see Eqs. 4.2 and 4.3).

seen in Fig. 4.9, where the angular cross-correlation function of the combined maps for both estimators is shown. For comparison, we show the expected signal from the plain *MHD Gal* simulation (e.g. assuming a very small *magnetic depth* of $z = 0.03$), the GF signal alone, and the *MHD Gal* combined with the GF signal for a large *magnetic depth* (i.e. $z = 1.03$), as well as for a extreme *magnetic depth* corresponding to $z \approx 8$. In all cases we applied the foreground removal using a radius of 3°. Even for the extreme case of *magnetic depth*, despite the foreground removal applied, the normalized estimator ω_{RM} drops further by a factor of ~ 3 when adding the GF, and drops by a factor of ~ 30 for the most optimistic cosmological signal. On the contrary, the unnormalized estimator ξ_{RM} turns out to be quite insensitive to the foreground provided that the removal technique is applied. The combined signal still corresponds roughly to the original, cosmological one, as can be seen when comparing with Fig. 4.4.

We conclude, that although the normalized estimator ω_{RM} in principle contains a much more unbiased and reliable imprint of the cosmological magnetization, once GF and observational noise are added, the underlying cosmological signal is completely lost. In contrast, the unnormalized estimator ξ_{RM} is relatively insensitive to the GF and to the noise. However, as seen before, the interpretation of its amplitude and shape is extremely challenging, as it is quite biased by the underlying *magnetic depth* probed by the redshift distribution of the radio sources used in the RM measurements.

4.5 The simulated observational cross-correlations: an example

To study if it is possible to infer the underlying cosmological signal through an observational process which includes GF (and its removal technique) as well as measurement errors by cross-correlating the |RM| signal with the galaxy density we assume:

- An optimistic *magnetic depth* of the universe of $z = 1.03$;
- A GF according to the model presented in Section 4.4.3 together with the foreground subtraction technique presented in Section 4.4.1 using the mean value of the |RM| map within 3°;

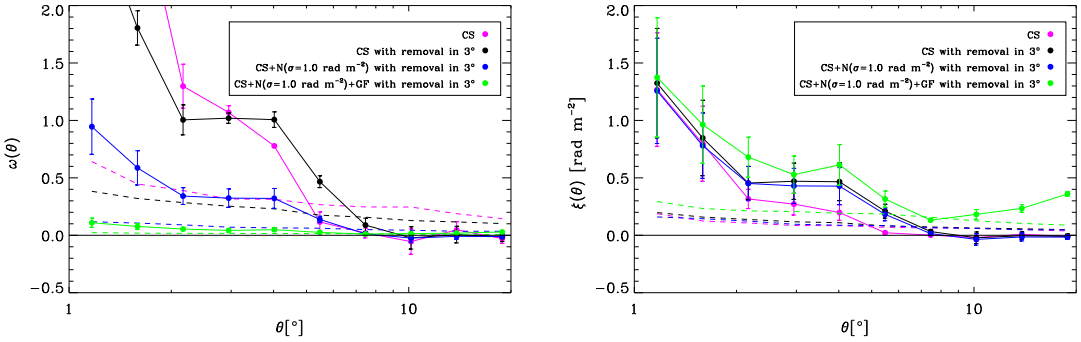

Figure 4.10: Changes in the cross-correlation functions for the two estimators ω_{RM} (left panel) and ξ_{RM} (right panel) when gradually including all described steps to the cosmological signal (CS) using the *MHD Gal* simulation with a*magnetic depth* of the universe of $z = 1.03$. GF and N stand for Galactic foreground and observational noise respectively.

- A measurement error distribution consistent with a Gaussian having $\sigma_{\rm RM} = 1$ rad m^{-2}, i.e. a dispersion similar to the magnitude of typical errors achievable by future instruments.

4.5.1 Signal pile-up

Fig. 4.10 shows how the resulting signal changes when gradually adding all effects described before, using the *MHD gal* model. As already seen in the individual steps above, the normalized estimator ω_{RM} gives a much more significant signal, but its amplitude and shape suffers dramatically from the inclusion of noise and addition of the GF (despite of the subtraction technique applied). On the other hand, the unnormalized estimator ξ_{RM} gives a much less significant signal only mildly changed by all the contributions to the total signal, mainly at larger distances.

4.5.2 Differentiating cosmic magnetization

Fig. 4.11 summarizes the results for such a combination of contributions to the total signal for our five different magnetic field models. The signal for the normalized estimator ω_{RM} (left panel) is reduced by a factor of ~ 50 and the shape does not represent the underlying magnetic field models as well as when applied to the cosmological signal itself (e.g. compare with Fig. 4.5). The amplitude of the unnormalized estimator ξ_{RM} corresponds to the underlying cosmological signal, but here the original ordering due to the magnetic field models is no longer present. In general, for both estimators, the significance of the total signal is only marginal and the differences between the different magnetic field models lie far inside the error bars. Note that if we would only consider the *null* signal and ignore the errors from the magnetic field realization both estimators would give highly significant detections. The errors coming from the magnetic field realizations are not accessible from the observations and, therefore, the observationally obtained significance of the signal can be misleading unless compared to detailed simulations. As well, both errors can be significantly reduced by using higher number of RMs. The results can also be improved by avoiding the Galactic region (e.g. cutting the region of the maps lying inside $\pm 10°$).

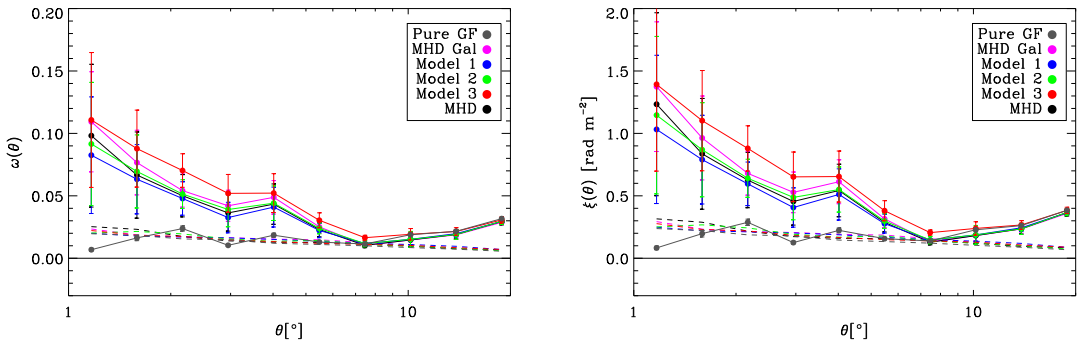

Figure 4.11: Cross-correlation functions for the different magnetic field models, using an optimistic *magnetic depth* for the cosmological signal (CS) (corresponding to a universe magnetized out to $z = 1.03$), taking into account the Galactic foreground (GF), assuming a Gaussian noise (N) with $\sigma_{\rm RM} = 1$ rad m^{-2} (as expected for the next generation of instruments) and applying the foreground subtraction in 3°. Left panel shows the result for normalized estimator ω_{RM} whereas the right panel shows the result for the unnormalized estimator ξ_{RM}.

In that case, the unnormalized estimator will strongly reduce the power excess seen at distances larger than 3°. Such a cut would also remove the artificial but significant signal seen for separations larger than 10° in both estimators.

4.6 Conclusions

Using cosmological MHD simulations of the magnetic field in galaxy clusters and filaments we evaluated the possibility to infer the magnetic field strength in filaments by measuring cross-correlation functions between RMs and the galaxy density field.

We find that the shape of the cross-correlation function using the normalized estimator ω_{RM} (in absence of any noise or foreground signal) nicely reflects the underlying distribution of magnetic field within the large scale structure. However, a very large number of lines of sight probed by RM measurements (much more than the 3072 used in this investigation) are needed to overcome the statistical noise induced by the particular magnetic field realization within the cosmic structures, in order to distinguish between the wide range of models we used here. In general, the RM signal is strongly dominated by the denser regions (e.g. those populated by galaxy clusters and groups) and not by the low density ones, like filaments. On this point, the magnetic field associated with filaments already changes by several orders of magnitudes within the different models used here.

Additionally, the normalized estimator ω_{RM} is extremely sensitive to measurement errors and to the presence of the GF (despite attempts to remove it by subtracting a smoothed map). It is fair to say that given the current measurement errors in the available RMs and our knowledge of the GF, present studies cannot determine the magnetization magnitude of the Universe based only on the cross-correlation ω_{RM}, whatever the significance of the measured signal is. On the contrary, the shape of the unnormalized estimator ξ_{RM} (the same as used by Lee et al. 2009) is relatively insensitive against the presence of measurement errors for the RMs and for the presence of the GF (as long as the described removal technique is used). Its amplitude, however, is quite strongly

affected by measurement uncertainties. Current measurement errors (as for example those inherited by the Taylor's published sample) suppress the signal by a significant amount in such a way that it is impossible to relate the amplitude of the cross-correlation function to the underlying magnetization of the the large scale structure. However, we expect that future radio telescopes will be able of reaching error magnitudes of order of 1 rad m^{-2} that could make the correction of the signal possible.

Unfortunately, this estimator does not nicely encode in its shape the details of the magnetization of the large scale structure and, especially, its amplitude is extremely sensitive to the *magnetic depth* of the Universe. Therefore, any interpretation of an observed signal is limited by our knowledge of the redshift distribution of the sources (towards the RM signals measured), as well as by our knowledge of the distribution and evolution of the cosmic universal magnetization. Future observational data will help to put better constraints on theoretical models for the origin of cosmological magnetic fields which, in return, can be implemented in next generation of MHD cosmological simulations in order to draw a self-consistent picture that can be compared against observations.

In summary, we conclude that current RM observations cannot constrain the amplitude and distribution of magnetic fields within the large scale structure. On the other hand, future data-sets, based on a larger number of observations with more accurate RMs, might be able to shed light on the magnetic field distribution and evolution within these structures. However, very detailed model predictions are needed in order to compare with any observed cross-correlation signal. It will be a quite demanding task for future cosmological simulations to provide detailed enough information of the large scale structure magnetization process within a large enough volume to produce useful templates of such correlation functions which can then be compared directly to the observations.

Part IV

Conclusions

Chapter 5

Summary and outlook

Some say that the universe is made so that when we are about to understand it, it changes into something even more incomprehensible. And then there are those who say that this has already happened.

The Hitchhikers guide to the galaxy - Douglas Addams (1952-2001)

Magnetic fields are found in almost every environment in the studied Universe. However, they are notoriously difficult to measure because of the lack of possible direct observations at large astrophysical distances. Nevertheless, progress has been made, and their presence in the inter-galactic medium and intra-cluster medium has been confirmed by observations of diffuse radio emission as well as *Faraday* rotation measurements towards polarized radio sources within or behind the magnetized medium (e.g. Govoni, 2006). Recent studies (Dolag et al., 2010) even show considerable *magnetic filling factors* in cosmological volumes, like those in filaments or voids.

Given the high non-linearity of many of the physical processes involved in astrophysical problems, the use of numerical codes has become a powerful technique and widespread approach for studies of structure formation. Astrophysical fluid dynamics usually involve changes on spacial, temporal and density scales over several orders of magnitude. Thus, adaptivity is essential to study these problems. An elegant solution to face this if offered by Smooth Particle Hydrodynamics (SPH). However, it was not until recently that it became possible to solve MHD equations using the SPH formalism. This unique tool can now be extensively used to constrain the interaction of magnetic fields with the baryon component of the Universe in several environments, from star forming regions to galaxy clusters, including galaxy evolution and cosmic ray propagation.

Cosmological MHD Simulations

We focused in novel implementations of MHD inside the well-known cosmological SPH code Gadget-3. Thereby, we were able to implement and study different MHD approximations and schemes, either building the field from potentials or evolving the magnetic field itself. The vector nature of magnetic fields translates into an extra level of complexity compared with known numerical problems already solved for scalar fields, like density or temperature fields. There are known issues related with SPH interpolants that can be problematic in the case of MHD. For instance, the constraint $\nabla \cdot \mathbf{B} = 0$ in the *Maxwell* equations is not ensured for the numerical implementation itself. This is not

only a problem from the physical point of view, but being not zero this divergence can grow instabilities by adding an artificial contribution to the *Lorentz* force and possibly drive artificial dynamo effects.

Such issues are now well understood and can be controlled (Dolag and Stasyszyn, 2009). The combination of many improvements in the underlying SPH algorithm with its generalization to the MHD case enhances the handling of magnetic fields in SPH significantly. We found that correcting the instability by explicitly subtracting the contribution of a numerical non-zero $\nabla \cdot \mathbf{B}$ to the *Lorenz* force from the *Maxwell* tensor, is useful in terms of stability [1]. Placing a limiter in this correction improves the performance and quality of the numerical scheme. This limiter is needed because in certain situations the $\nabla \cdot \mathbf{B}$ source term can be temporally high, thus driving instabilities if taken into account directly. This improvement is particularly efficient in three dimensional setups, where it seems to work much better than other suggestions in the literature.

We studied two regularization schemes: smoothing the magnetic field and including an artificial dissipation. The first scheme basically regularizes the magnetic field by smoothing it every desired time interval. The second scheme regularizes strong variations in the field by artificially introducing diffusivity terms in the induction equation. The schemes demonstrated to further minimize inter-particle noise and $\nabla \cdot \mathbf{B}$ errors. However, one has to carefully select the numerical parameters to avoid excessive smoothing of sharp features. In particular, the magnetic field smoothing succeeds in terms of stability, however, in general it tends to over-smooth features independent of the dynamics of the system. The artificial dissipation also increases the stability (behaving similarly to the magnetic field smoothing). Yet, in this case, the over-smoothed features come from the changes in the magnetic field morphology itself. Because there is no dependence in global time-steps and it depends on local gradients, this scheme turns out to be desirable for physical runs. However, there are cases in which those gradients are correct and the magnetic field configuration is over suppressed. From a physical point of view, both regularisation schemes mimic the effects of diffusion by numerical means.

We also implemented a $\nabla \cdot \mathbf{B}$ cleaning scheme (namely *Dedner*), which constructs and follows a scalar field build up from the $\nabla \cdot \mathbf{B}$ errors. From this field we correct the original magnetic field to the numerical threshold given by our resolution. The successful implementation of a multidimensional *Dender* cleaning method in SPH, does not significantly affect the shape of the front shocks while reducing the numerical $\nabla \cdot \mathbf{B}$ generated. The evolution of this correction is completely local within the Hsml and therefore only affected by the quality of SPH derivatives. The success of $\nabla \cdot \mathbf{B}$ cleaning brings our simulations closer to the "ideal" MHD state (Stasyszyn et al., 2011), with only fast reconnection happening inside the representative volume of each particle.

Finally we study the magnetic field evolved from the advection of two scalars, the so called *Euler* potentials, from which we construct the final magnetic field. The implemented potential approach has the benefits of fulfilling the constraint $\nabla \cdot \mathbf{B} = 0$ by construction, up to a numerical threshold. Hence, we are able to compare results between schemes, demonstrating that schemes using the induction equation reach similar error levels when measured in the tests. In the astrophysical cases, *Euler* potentials schemes have the drawback of being unable to change the topology of the field. Therefore no reconnection occurs, losing representativity of the astrophysical system. In those cases the magnetic

[1] Even when using *Euler* potentials to construct the magnetic field

field obtained by this method is the representation of the stochastic processes driven by the dynamics of the system. Therefore helping us to test different phenomenological approaches to drive the magnetic field evolution.

We studied the magnetic field evolution in the context of cosmological structure formation of galaxy clusters. Given the complexity inherent to MHD simulations, our studies were non-radiative, to focus on how magnetic fields can reproduce observations without any additional physics. We compare different numerical schemes leading us to the conclusion that the $\nabla \cdot \mathbf{B}$ terms are not important for the evolution or growth of the magnetic field in galaxy clusters. As found in the tests, the special care taken for the $\nabla \cdot \mathbf{B}$ terms demonstrated to be useful to lower inter particle scatter, improving the overall performance of the code. We conclude that the turbulent cascades are well modeled in the simulations, which is manifested in the growth of the magnetic field. This was concretely studied by the *Euler* potentials runs, where the reconstructed magnetic field is given by the final turbulent driven configuration. We observe that despite this facts, the $\nabla \cdot \mathbf{B}$ errors between schemes in our region of interest are similar, meaning that this turbulence is phenomenological and not numerically driven. Due to the lack of diffusion in these runs, the magnetic field accumulates in the center of the cluster and is not distributed to the outermost parts of the halo, especially in the case when we do not take into account the *Lorentz* force. From the magnetic field profiles we conclude that the magnetic field distribution in inner region of the cluster, depends strongly on the numerical dissipation of the underlaying scheme. However, the outer part agree with the *self-similar* model when compared between different schemes and resolutions. Furthermore, a non dissipative scheme allows for complex morphological structures as expected in galaxy cluster or even in galaxies. On the other hand, additional physics like *Ohmic* dissipation are expected to be important (Bonafede et al., 2010). Therefore, a numerical scheme like *Dedner*, with low numerical diffusion, is interesting for future studies of the interplay of physical diffusion and magnetic field morphology in the ICM.

We made synthetic rotation measure maps and study the reversals of the magnetic field in comparison with observations. The artificial dissipation and smoothing cases are extreme in this context. They present just a few big reversals zones on scales of ~ 100 Kpc. In the other runs, we resolve a larger number of reversals, with spacial scales of the order of ~ 10 Kpc, which is closer to the observed values. Additionally, in the case of *Euler* potentials with *Lorentz* force, we observe a synthetic map comparable with dissipative runs. This implies that a complete stochastic representation of MHD turbulence does not properly reproduce the observations in terms of reversals. We observe that, as we enhance the resolution the number of reversals increases, demonstrating a better resolution of the turbulent cascade.

With the synthetic maps we are able to build structure functions, which can be a quantitative comparison with observations. Additionally, simple isotropic turbulent theories make predictions on the shape of these structure functions. However, when comparing theory with observations, we are not able to distinguish between models because of the uncertainties in observations and the small difference in the scale dependence of the slopes. When studying the structure functions of the synthetic maps, we reproduce the overall behavior. We have not yet reached the resolution to reproduce all the features from observations. However, we see how the results tend to the observed ones at the highest resolution, which is a promising result. The comparison between observations and high resolution simulations suggests that the physics may be described

by a multi scale turbulence model. This means that the turbulent dynamo driven by the cosmological cluster formation process works effectively, reproducing basic observational properties, even to details shown in structure functions.

We clearly demonstrate that using advanced schemes together with high resolution allow to probe the properties of the ICM. Additional astrophysical effects (such as star formation, AGN feedback, etc.) will contribute to steer-up the inter-cluster medium, therefore helping to generate turbulence and power in the magnetic field structure function on different scales. Additionally, we show that the comparison of synthetic RM maps with observations can be used to assess which physics are relevant in the underlaying phenomena, contributing to the global picture of the galaxy cluster physics, as can be a multi-scale turbulence model.

In addition to the cosmological results, a stable numerical scheme is useful in several astrophysical problems. One major example is the first simulation of the collapse of protostellar cores including ideal-MHD following the *induction equation* with SPH (Bürzle et al., 2010), showing the effects of the magnetic fields in multiple star formation. Another example is given by the studies of galaxies (Kotarba et al., 2009, 2010a,b), which clearly demonstrates how the magnetic field reaches equipartition with the turbulent energy. These studies are a particularly exciting subject given the impressive quality of observational data which we can compare with (e.g Beck, 2009), and which provide important dynamo theory challenges.

Statistical studies

Having demonstrated that structure formation simulations are able to reproduce properties of magnetic fields in galaxy clusters, especially in the outer regions of haloes, we investigate the relation between the magnetic field and the structure in which it is embedded.

Recently new large observational data sets (e.g. Taylor et al., 2009) became available, requiring simulations of cosmological volumes with magnetic field to test their properties of cosmic volumes. These large amounts of data open the possibility for statistical studies of the distributions of baryons and magnetic field. We use a set of cosmological MHD simulations to evaluate the possibility of inferring the magnetic field strength by statistical means, particularly measuring cross-correlation functions between rotation measures and the galaxy density field.

To take into account the uncertainties in the possible dynamo implicated in our simulations, we study the effects of several models of scale-up the magnetic field with density. We use the same field in the center of the clusters (that is well constrained as shown before) and different field strengths in low density regions (like filaments and voids). The use of different magnetic field models associated to the cosmological structures, allows us to compare variations of several orders of magnitude in the magnetic values in large scales. Additionally, we compare with observational results, and try to mimic all the possible observational bias. Therefore, we build a synthetic foreground map of the galaxy and apply different estimators used in observations to suppress spurious effects. Finally, we also added noise expected from current instruments and made predictions for future instrumental facilities. Taking into account all the steps in the process separately allowed us to understand each of them and to find out which are most important.

In general, the observational rotation measure signal is strongly dominated by denser regions (e.g. those populated by galaxy clusters and groups), and the transition of the magnetic field to low density regions is unclear. We find that the shape of the cross-correlation function using a normalized estimator ω_{RM} (in absence of any noise or foreground signal) nicely reflects the underlying distribution of magnetic field within the large scale structure.

The normalized estimator ω_{RM} is extremely sensitive to measurement errors and to the presence of the galactic foreground (despite attempts to remove it by subtracting a smoothed map). It is fair to say that given the current measurement errors in the available observed rotation measurements and our knowledge of the galactic foreground, present studies cannot determine the magnetization magnitude of the Universe based only on the cross-correlation ω_{RM}, whatever the significance of the measured signal is. On the contrary, the shape of the unnormalized estimator ξ_{RM} is relatively insensitive against the presence of measurement errors dur to noise and for the presence of the rotation measurement foreground (as long as a removal technique is used). Its amplitude, however, is quite strongly affected by measurement uncertainties. Current measurement errors (as for example those inherited by the sample published by Taylor) suppress the signal by a significant amount in such a way that it is impossible to relate the amplitude of the cross-correlation function to the underlying magnetization of the large scale structure (Stasyszyn et al., 2010).

Future Prospects

It is known that clusters with high cooling rates seem to have stronger magnetic fields (Taylor et al., 1994). This leads us to a full set of predicted observables that can be constrained from numerical studies. helping to understand which effects are more important to prevent the catastrophic collapse of cooling clusters. However, this also means that the magnetic field in such regions can be dynamically important, and thus we need a stable numerical implementation, such as the one presented, to start to study those regimes. Additionally, even in regions where magnetic field are not dynamically important, we can use them as tracers to study turbulence and dissipative processes known to be part of the ICM, and in combination with *X-ray* measurements (Zhuravleva, 2011) trace their importance and effects.

Transport process inside clusters are sensitive to magnetic fields, and simulations help to construct recipes to a proper treatment of these processes (Donnert et al., 2011). Therefore, to continue exploring the effects of magnetic fields, we need to include its effects self-consistently in the *sub-grid* physical methods. Magnetic fields are expected to have important effects and can act as an additional energy depending on the environment properties. This has to be taken into account into the energy balance of the system and linked to other process. The use of a self-consistent implementation implies that energy will be redistributed, which is important in studies of cosmic ray propagation or cluster relics and cavities.

As we mentioned, the current measurements of magnetic field in different environments are not completely explained by primordial magnetic fields and their growth due to only gravitational collapse, signaling that additional dynamo actions should occur naturally in the Universe. Besides the magnetic field *seeding* there are possible dynamo actions

that include non-ideal MHD.Within the present development status of MHD in Gadget-3, possible numerical artifacts are well constrained. Therefore this numerical code is an ideal ground for implementations of theoretical dynamo models or additional *sub-grid* physics. How dynamo mechanism work is an important question that can be applied on different scales, from galaxy discs to collapsing clouds in star forming regions or AGN accretion disks.

Magnetic fields are known to play a supporting role in the formation and evolution of several astrophysical objects (e.g. stars). Even if true that magnetic fields are not essential for our understanding of the large-scale dynamics of the Universe, a total knowledge of structure formation process seems to be not possible without solving also the physics on smaller scales. Therefore, in our seek for understanding magnetic fields in the Universe, we can find answers to other astrophysical questions.

Part V

Appendices

Appendix A

Magnetohydrodynamics and Plasma Physics

Magnetohydrodynamics (MHD) and plasma physics describe the interaction between electromagnetic fields and non-viscous conducting fluids (see, for example, Jackson, 1975; Parker, 1979). Basic fluid properties are velocity $\mathbf{V}(\mathbf{x}, t)$, pressure $p(\mathbf{x}, t)$, and current density $\mathbf{J}(\mathbf{x}, t)$. In Gaussian units, the relevant Maxwell equations take the form

$$\nabla \times \mathbf{B} = \frac{4\pi}{c}\mathbf{J} \tag{A.1}$$

which is called *Ampère* Law. It was taken into account that moving charges generate a measurable Magnetic Field (this effect was also know in the case of constant current as *Biot-Savart* law).

Then there is a relation between the variation in the magnetic field fluxes and the electromotive energy.

$$\nabla \times \mathbf{E} + \frac{1}{c}\frac{\partial \mathbf{B}}{\partial t} = 0 \tag{A.2}$$

which is known as *Faraday* induction equation. Note that this equation is similar to Eq. (A.1), and even more interesting is the fact that the change in flux can be given by moving magnets either by electric fields. If we choose a special reference frame, these equations will lead to a relation between velocities that the magnetic field is moving and a force that will appear trying to satisfy the relation in Eq. (A.2).

$$\mathbf{F_{mag}} = \mathbf{J} \times \mathbf{B} \tag{A.3}$$

This is know as the *Lorentz* Force [1].

Another interesting fact in the magnetic field studies are the absence of monopole sources. All manifestations of magnetic fields comes in the form of dipoles or representations of higher order expansions. This is represented by

$$\nabla \cdot \mathbf{B} = 0 \tag{A.4}$$

This is supported by experiments, that have constrained their possible existence to almost *null* probability. But, let's suppose hypothetically that Eq. (A.4) is not valid, if so this

[1] The total energy will have another term referring to the electric field $\mathbf{F} = q\mathbf{E}$ that we neglect, because in our problem $\mathbf{E}$ is completely neglected.

will imply that these magnetic charges have similar properties as the electric charges. Then one can derive that electromagnetic waves should not exist. And the fact that we can use them in everyday life is one of the most important supporting facts to Eq. (A.4). For further insights about this subject I recommend to follow the discussions in Parker (2007).

Free charges moving are subject to be trapped by the medium. This is taken by Ohm's law

$$\mathbf{J} = \sigma \mathbf{E} \tag{A.5}$$

where σ is the conductivity in the rest frame of the fluid. Most astrophysical fluids are electrically neutral and non-relativistic so Eq. (A.5) becomes

$$\mathbf{J} = \sigma \left(\mathbf{E} + \frac{\mathbf{V} \times \mathbf{B}}{c} \right) \tag{A.6}$$

being the term with the cross product of the $\mathbf{B}$ times $\mathbf{V}$ the result from the *Lorentz* force. This can be combined with Eq. (A.2) and Eq. (A.1), to yield the ideal MHD equation:

$$\frac{\partial \mathbf{B}}{\partial t} = \nabla \times (\mathbf{V} \times \mathbf{B}) + \eta \nabla^2 \mathbf{B}. \tag{A.7}$$

To derive this equation, the molecular diffusion coefficient, $\eta \equiv c^2/4\pi\sigma$, is assumed to be constant in space.

To have a complete set of dynamical equations we must define a continuity equation for the fluid

$$\frac{d\rho}{dt} = -\rho \nabla \cdot \mathbf{V}, \tag{A.8}$$

which is important because relate the density of our fluid ρ with the pressure $\nabla \cdot \mathbf{V}$.

In the limit of infinite conductivity, magnetic diffusion is ignored and the induction equation becomes

$$\frac{\partial \mathbf{B}}{\partial t} = \nabla \times (\mathbf{V} \times \mathbf{B}) \tag{A.9}$$

or equivalently

$$\frac{d\mathbf{B}}{dt} = (\mathbf{B} \cdot \nabla)\, \mathbf{V} - \mathbf{B}\, (\nabla \cdot \mathbf{V}) \tag{A.10}$$

where $d/dt = \partial/\partial t + \mathbf{V} \cdot \nabla$ is the convective derivative, so-called *Lagrangian* and we use Eq. (A.4).

The first term in Eq. (A.10) describes the stretching of magnetic field lines that occurs in flows with shear and vorticity. As an illustrative example, consider an initial magnetic field $\mathbf{B} = B_0 \hat{\mathbf{x}}$ subject to a velocity field with $\partial V_y/\partial x =$ constant. Over a time t, $\mathbf{B}$ develops a component in the y-direction and its strength increases by a factor $\left(1 + (t\, \partial V_y/\partial x)^2\right)^{1/2}$.

The second term describes the adiabatic compression or expansion of magnetic field that occurs when $\nabla \cdot \mathbf{V} \neq 0$. Consider, for example, a region of uniform density ρ and volume $\mathcal{V}$ that is undergoing homogeneous collapse or expansion so that the first term is null and $\nabla \cdot \mathbf{V} = C$ where $C = C(t)$ is a function of time but not position. Using

the continuity equation and Eq. (A.10) one find that $B \propto \rho^{2/3} \propto \mathcal{V}^{-2/3}$. Thus, magnetic fields in a system that is undergoing gravitational collapse are amplified while cosmological fields in an expanding universe are diluted.

Combining Eq. (A.10) and Eq. (A.8) one can find the following alternative form

$$\frac{d}{dt}\left(\frac{\mathbf{B}}{\rho}\right) = \left(\frac{\mathbf{B}}{\rho}\cdot\nabla\right)\mathbf{V}. \tag{A.11}$$

The formal solution of this equation is

$$\frac{B_i\left(\mathbf{x},\, t\right)}{\rho\left(\mathbf{x},\, t\right)} \;=\; \frac{B_j\left(\xi,\, 0\right)}{\rho\left(\xi,\, 0\right)}\frac{\partial x_i}{\partial \xi_j} \tag{A.12}$$

where ξ is the Lagrangian coordinate for the fluid:

$$x_i(t) = \xi_i + \int_0^t V_i(s)ds\ . \tag{A.13}$$

It follows that if a "material curve" coincides with a magnetic field line at some initial time then, in the limit $\eta = 0$, it will coincide with the same field line for all subsequent times. Thus, the evolution of a magnetic field line can be determined by following the motion of a material curve (in practice, traced out by test particles) as it is carried along by the fluid. This is called that the field is *frozen-in* with the plasma.

The equation of motion for the fluid is given by

$$\frac{\partial \mathbf{V}}{\partial t} + \left(\mathbf{V}\cdot\nabla\right)\mathbf{V} = -\frac{1}{\rho}\nabla p - \nabla\Phi + \frac{1}{c\rho}\left(\mathbf{J}\times\mathbf{B}\right) + \nu\nabla^2\mathbf{V} \tag{A.14}$$

where ν is the hydrodynamic viscosity coefficient of the fluid and Φ the gravitational potential. In many astrophysical situations, the fields are weak and the *Lorentz* term in Eq. (A.14) can be ignored. This is the kinematic regime. In the limit that the pressure term is also negligible, the vorticity $\zeta \equiv \nabla\times\mathbf{V}$ obeys an equation that is similar, in form, to Eq. (A.7):

$$\frac{\partial \zeta}{\partial t} = \nabla\times\left(\mathbf{V}\times\zeta\right) + \nu\nabla^2\zeta. \tag{A.15}$$

Moreover, if viscosity is negligible, then ζ satisfies the Cauchy equation (Moffatt, 1978):

$$\frac{\zeta_i\left(\mathbf{x},\, t\right)}{\rho\left(\mathbf{x},\, t\right)} \;=\; \frac{\zeta_j\left(\xi,\, 0\right)}{\rho\left(\xi,\, 0\right)}\frac{\partial x_i}{\partial \xi_j}\ . \tag{A.16}$$

However, Eq. (A.16) is not a solution of the vorticity equation so much as a restatement of Eq. (A.15) since $\partial x/\partial\xi$ is determined from the velocity field which, in turn, depends on $\mathbf{x}$. By contrast, in the kinematic regime and in the absence of magnetic diffusion, Eq. (A.12) provides an explicit solution of Eq. (A.10).

The magnetic energy density associated with a field of strength $\mathbf{B}$ is $\epsilon_B = \mathbf{B}^2/8\pi$. For reference, we note that the energy density of a 1 G field is $\simeq 0.040\,\mathrm{erg\,cm^{-3}}$. A magnetic field that is in equipartition with turbulent energy of a fluid of density ρ and rms velocity v has a field strength $B \simeq \left(4\pi\rho v^2\right)^{1/2}$. In a fluid in which magnetic and kinetic energies are comparable, hydromagnetic waves either propagate parallel or perpendicular to the direction of the magnetic field. The first ones are the so-called

Alfvén waves and propagates at a characteristic speed $v_A \equiv (B^2/4\pi\rho)^{1/2}$. The second ones are called magnetosonic waves and have similar characteristics than sonic waves but with the contribution of the magnetic pressure.

It is often useful to isolate the contribution to the magnetic field associated with a particular length scale L. Following Rees and Reinhardt (1972) we write

$$\left\langle \frac{B^2}{8\pi} \right\rangle = \int_{\mathcal{V}} \frac{B(L)^2}{8\pi} \frac{dL}{L} \tag{A.17}$$

where $\langle B^2/8\pi \rangle$ is the magnetic field energy density averaged over some large volume $\mathcal{V}$. $B(L)$ is roughly the component of the field with characteristic scale between L and $2L$. Formally, $\mathbf{B}(L) = (k^3/2\pi^2\mathcal{V})^{1/2}\,\mathbf{B}_k$ where $\mathbf{B}_k \equiv \int d^3x \exp(i\mathbf{k}\cdot\mathbf{x})\mathbf{B}(\mathbf{x})$ is the Fourier component of $\mathbf{B}$ associated with the wave number $k = 2\pi/L$.

In the ideal MHD limit, magnetic fields are distorted and amplified (or diluted) but no net flux is created. A corollary of this statement is that if at any time $\mathbf{B}$ is zero everywhere, it must be zero at all times. This conclusion follows directly from the assumption that charge separation effects are negligible. When this assumption breaks down, currents driven by non-electromagnetic forces can create magnetic fields even if $\mathbf{B}$ is initially zero. Therefore, to have a dynamo effect working, we must apart from an ideally MHD.

Appendix B

Finding optimal numerical parameters

All the methods described in section 2.3, had their particular numerical parameters that modify how the schemes will behave. Those parameters are difficult to choose, because in some situation their effects are minimal, while in other cases can be counterproductive. To find the optimum numerical parameters, we performed 11 shock-tube tests with different settings for the parameters in the regularization methods and evaluated the quality of the result obtained with the SPH-MHD implementation, and confirmed them with a smaller span in the planar tests. To have a quantitative measure of the tests, we used two estimators. First, we have chosen the mean of all $\nabla \cdot \mathbf{B}$ errors within the simulation region, as defined by

$$\Delta_{\nabla\cdot\mathbf{B}} = \left\langle \nabla \cdot \mathbf{B} \frac{h}{|\mathbf{B}|} \right\rangle_x . \tag{B.1}$$

Second, we measured the discrepancy of the SPH-MHD result for the magnetic field relative to the results obtain by ATHENA. Therefore we calculate first

$$\delta_{B^i}(x) = \{\left(B^i_{\mathrm{SPH}}(x) - B^i_{\mathrm{Athena}}(x)\right)^2\}\mathrm{RMS}^2_{B^i}(x) \tag{B.2}$$

for each component i of the magnetic field $\mathbf{B}$ within each 3D slab corresponding to the smoothing length. The RMS of B^i reflects the noise of B_i within the chosen slab. We then calculate

$$\hat{\Delta}_{B^i} = \left(\sum_x \delta_{B^i}(x)\right)\left(\sum_x \mathrm{RMS}^2_{B^i}(x)\right), \tag{B.3}$$

for each component of the magnetic field. This includes both contributions, the deviation of the SPH-MHD from the ideal solution as well as the noise within each 3D slab of the SPH-MHD implementation. To judge the improvement of the regularisation methods we sum up all three components and further relate this measurement to the value obtained with the *basic SPH-MHD* implementation, e.g.

$$\Delta_B = \frac{\sum_i \hat{\Delta}_{B^i}}{\sum_i \hat{\Delta}^{\mathrm{std}}_{B^i}} - 1. \tag{B.4}$$

We will use these two error estimators, $\Delta_{\nabla\cdot\mathbf{B}}$ and Δ_B, to measure the quality of the individual SPH-MHD implementations.

B.1 Divergence threshold

There are no significant effects in the threshold used in normal tests. We only can test this effects in extreme situations and by using the threshold to avoid the $\nabla \cdot \mathbf{B}$ generate unstable interactions. Therefore for this parameter, that in principle is free, we observe that in simulations is enough to ask if the change that will be done is of the same order of the force (i.e. parameter $\sim$ 1). However, just to ensure that the correction is not dominating the dynamics we use a value of 2 as shown in Eq. (2.42). The $\nabla \cdot \mathbf{B}$ errors are usually a couple of orders of magnitude below the change, and when one approach to the level of given by the *Lorentz* force equation, the correction is dominant and breaking the MHD equations. Therefore when applied to test cases, it does not contribute in the performance. However, as it helps to stabilize the situations, it improved the numerical values ranges where some tests can be performed. As an example for the test *1A* was unstable with *Dedner* for $\pi < 2$, and now the are able to test it until 10. That's because this implementation uses the $\nabla \cdot \mathbf{B}$ as source for the correction, and this particular test has the stronger shock fronts.

B.2 Regularization by smoothing the magnetic field

Choosing the time interval between smoothing the magnetic field is a compromise between reducing the noise in the magnetic field components, as well as $\nabla \cdot \mathbf{B}$) (by smoothing more often) and preventing sharp features from being smeared out. Figure B.1 shows a summary of the results of the individual shock-tube test computed with different smoothing intervals. As expected, when using shorter smoothing intervals the error in $\nabla \cdot \mathbf{B}$ reduces. For the quality measure of the SPH-MHD implementation the situation changes. Short smoothing intervals generally increase the discrepancy, many of them even to larger values than the *basic SPH-MHD* run. Specifically *4B* and *4C* show strong deviations due to smearing of sharp features. Note that the non monotonic behavior shown in some tests usually relates to some residual resonances between the magnetic waves and the smoothing intervals in the noise. Some tests show a minimum in the differences at smoothing intervals around 20. The test *3A* seems to prefer even shorter smoothing intervals. In general, values around 20-30 seem to be a good choice.

B.3 Artificial dissipation

As before, choosing the value for the artificial magnetic dissipation constant α_B is a compromise between reducing the noise in the magnetic field components (as well as reducing $\nabla \cdot \mathbf{B}$) and preventing sharp features from smearing out due to the effect of the dissipation. Figure B.2 shows a summary of the results of the individual shock-tube tests computed with different values for the artificial magnetic dissipation. As expected, using larger values reduces the error in $\nabla \cdot \mathbf{B}$ significantly. Similar to before, using larger values also generally results in an increase of the discrepancy between the SPH MHD implementation and the true solution, again usually to even larger values than in the *basic SPH-MHD* run. As before, especially the shock-tube test *4B* and *4C* show strong deviations due to smearing of sharp features. Note that here less non-monotonic behavior is visible (except for test *4B*). The main reason is that dissipation is a continuous process,

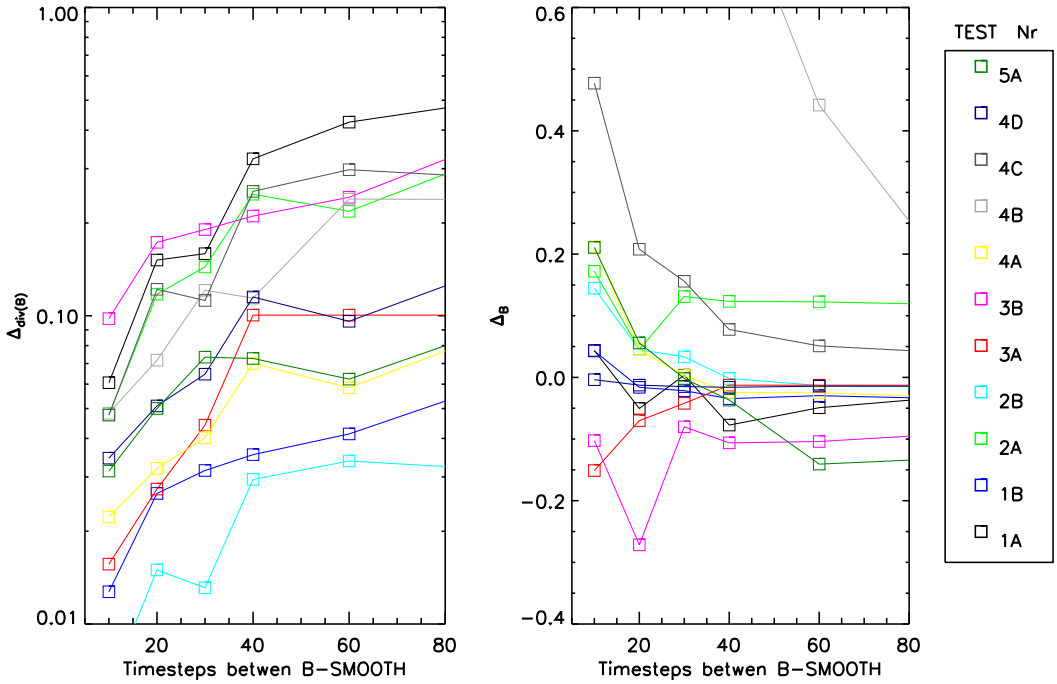

Figure B.1: Shown are the mean error in divergence (upper panel) and the measure of the quality (lower panel) as defined in equation (B.4) obtained by the SPH-MHD implementation for different values of the smoothing interval. The different lines are for the 11 different shock-tube tests as indicated by the labels.

so resonances between dissipation and the magnetic waves cannot be very pronounced. Taking all tests into account, a good choice for α_B seems to be around 0.1.

B.3.1 Time dependent artificial dissipation

One idea to reduce the effect of the artificial dissipation is to make the artificial magnetic dissipation constant α_B time dependent. The idea here is that, if the evolution of α_B is properly controlled, dissipation will happen only at the places where it is needed and it will be suppressed in all other parts of the simulation volume. The evolution of α_B is controlled by the two parameters S_0 (source term) and C (decay term) where we have chosen $\alpha_B^{\rm min}$ and $\alpha_B^{\rm max}$ as 0.01 and 0.5 respectively. Figure B.3 shows the result for varying these two parameters. As before, generally, the larger the dissipation is (e.g. large source term or small decay time) the smaller the noise and the error in $\nabla \cdot \mathbf{B}$ becomes. However, as soon as these parameters have values which drive α_B in the shocks to the maximum allowed value, there is marginally no gain in quality, although the values for α_B outside the shocks can still be quite small. Therefore, the time dependent method does not improve the results significantly, as the regions in which the artificial dissipation constant is suppressed do not significantly contribute to the smearing of sharp features.

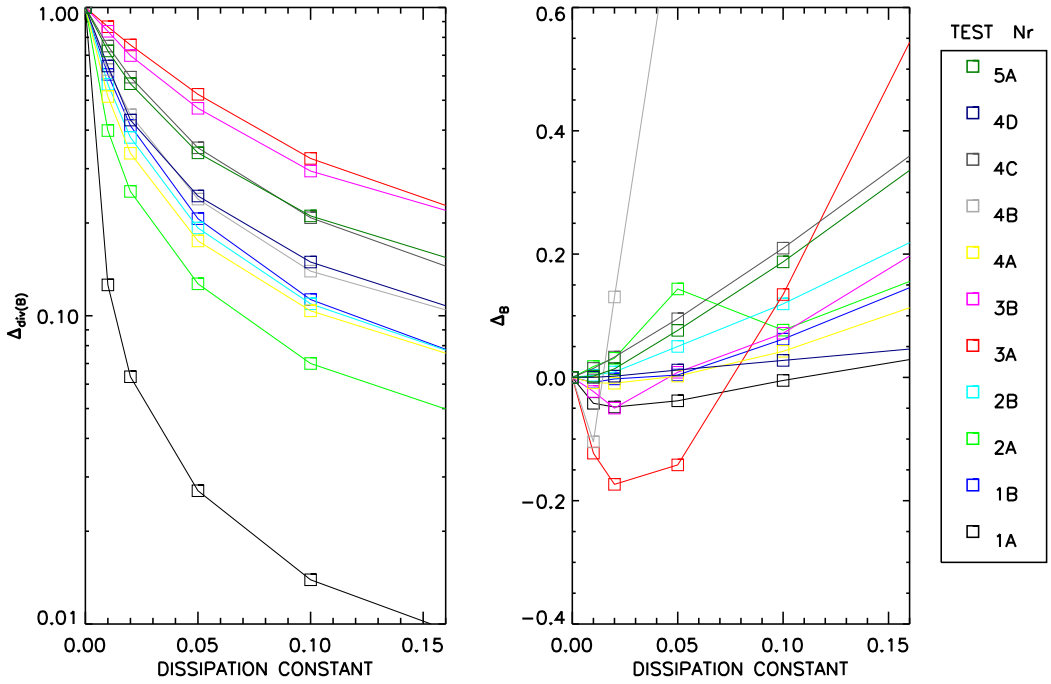

Figure B.2: Similar to figure B.1 but for different values of the artificial magnetic dissipation constant α_B.

B.4 Dedner Method

Basically in this scheme one has two major constant to be chosen. Namely c_h and c_p. c_h basically is the velocity in which the $\nabla \cdot \mathbf{B}$ errors will propagate away from the source. c_p is a dumping length in which we fade away the errors. Using Eq. (2.46) we can rewrite the equations in terms of the magnetic signal velocity and the smoothing length. In this scheme the first constant is σ that is related with the source (i.e. $\nabla \cdot \mathbf{B}$). If one let the errors propagate at the magnetic signal velocity seems to be a proper choice. Faster than that reduces the sensitivity of the scheme, and slower can make the errors to accumulate in some specific places. For the π case we needed to know how the different shocks were performing. In Fig. (B.4) we show the comparison for various π values, finding as optimum values $\pi \sim 2 - 3$. Note that it is not a clear trend, so the chosen value is not the best in all cases, but is a good compromise between all tests. Additionally to these constants, we added a threshold similar to the one used in the $\nabla \cdot \mathbf{B}$ subtraction. These study is also shown in Fig. (B.4). The best value corresponds to $Q = 0.5$, thus when the correction is the half of the change given by the induction equation, this correction is rescaled. Note that this studies were actually done in all the parameter space, but we just show the proper cuts to that parameter space in Fig. (B.4) at $Q = 0.5$ and $\pi = 3$. Again this values were ensured to be consistent in planar tests, were significantly enhanced the performance.

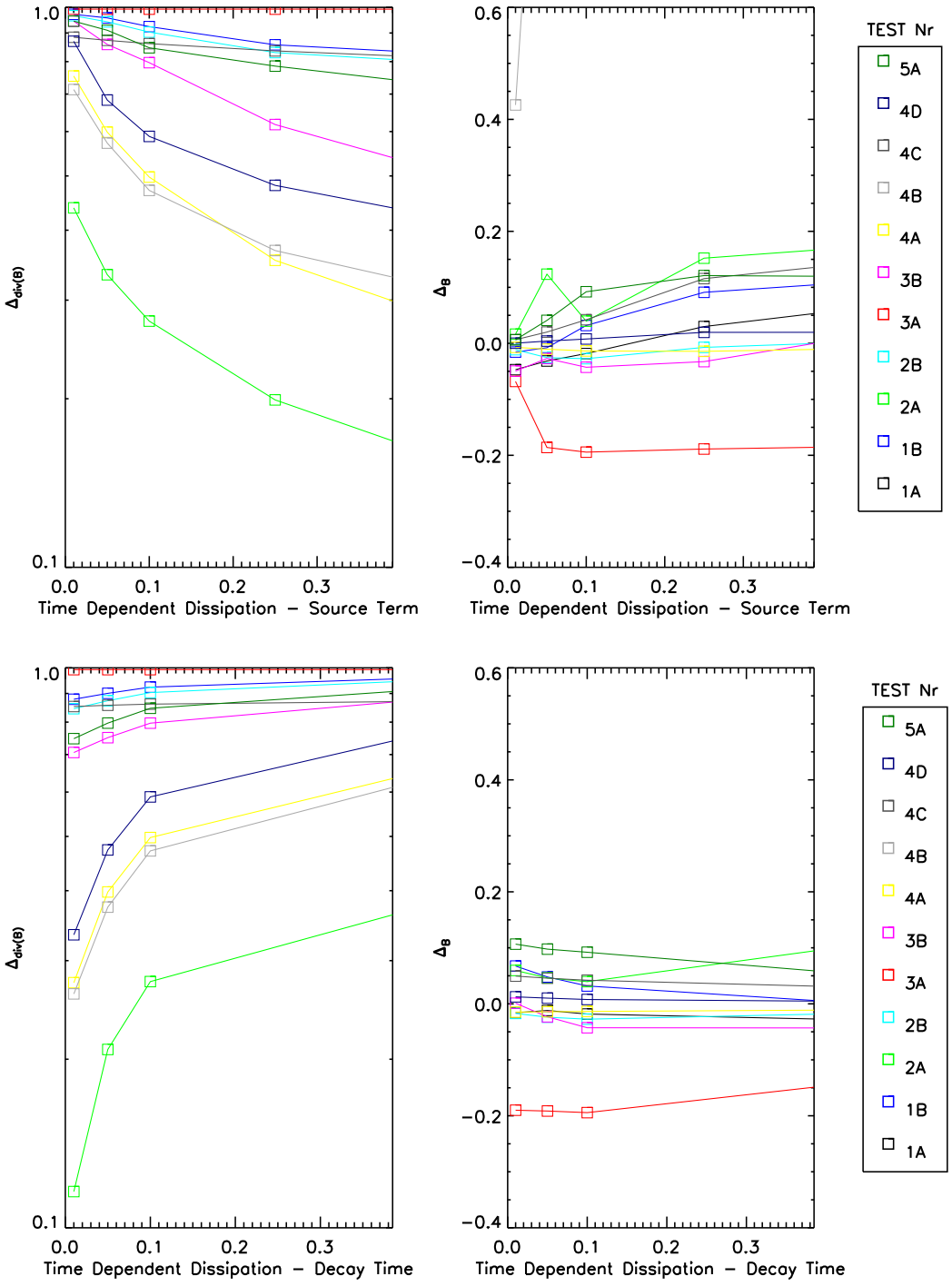

Figure B.3: Similar to figure B.1 but for different values of the source term S_0 (left panels) and the decay term C (right panel) of the time dependent, artificial magnetic dissipation.

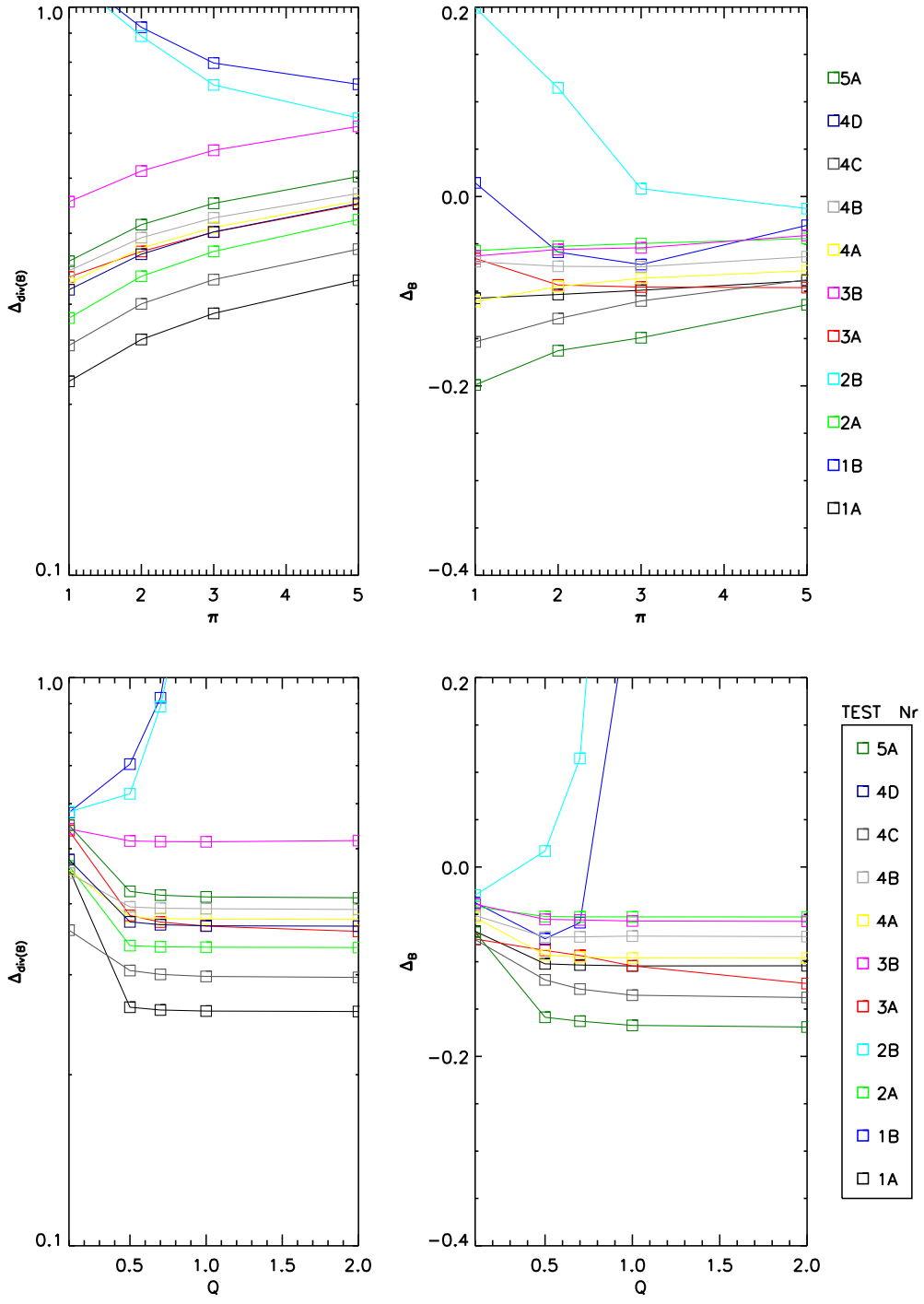

Figure B.4: Similar to figure B.1 but for different values of the dumping term π (left panels) and the threshold Q (right panel) of the *Dedner* scheme. When we vary π we have fixed $Q = 0.5$ and when varying Q we use

Appendix C

Resolution convergence tests

Numerical experiments are normally restricted by the resolution one can technically (in terms of computing/memory requirements) achieve. Therefore tests as presented in section 3 are usually at nominally better resolution than can be obtained in relevant (in this case cosmological) simulations. Never-the-less an interesting question is, how good do the numerical methods used converge if one further increase the resolution? Figure C.1 and C.2 show this for ATHENA and the *basic SPH-MHD* implementation respectively. We repeated the Orszang-Tang Vortex test problem with ATHENA on a 192^2, 400^2 and 800^2 grid. Figure C.1 shows a cut through the density of the *Orszang-Tang* Vortex, comparing with the result obtained with the AMR code Ramses (Teyssier, 2002). Clearly, the results obtained with ATHENA when increasing the resolution approaches the results obtained with Ramses. Figure C.2 shows the same for setups with $350^2 \times 5$, $700^2 \times 5$ and $1400^2 \times 5$ particles. The SPH-MHD implementation also converges towards the Ramses results with increasing resolution. However, although the central feature is better resolved in the SPH-MHD implementation than in the ATHENA run with comparable resolution, some other

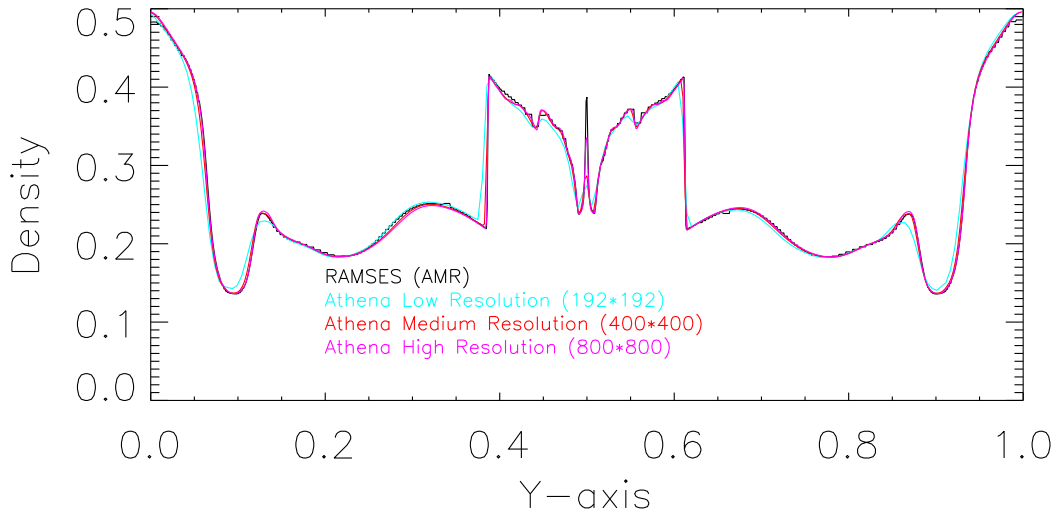

Figure C.1: A cut through the density for the Orszang-Tang Vortex test (see Figure 13/14). Shown in black is the result obtained with Ramses, compared to the results obtained with ATHENA using 3 different resolutions.

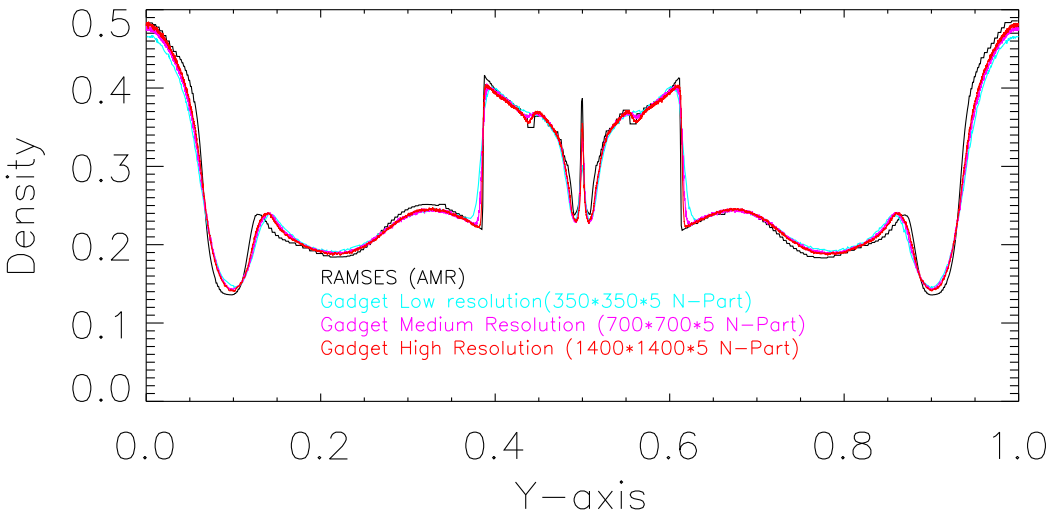

Figure C.2: Same than figure (C.1), but showing the results obtained with the *basic SPH-MHD* implementation at two different resolutions compared to the results obtained with Ramses.

features can be seen to converge slower in the SPH-MHD implementation when increasing the resolution. Specifically, in some very smoothed features there are small but systematic differences between the SPH and the true solution. Here the SPH results seem to converge only extremely slowly (if at all).

Appendix D

$\nabla \cdot \mathbf{B}$ distribution analysis

One of the major objections to MHD-SPH simulations comes from the $\nabla \cdot \mathbf{B}$ constrain, given the freedom inherent of particle schemes, this constrain can be subtle to be broken in regimes where the field is kinetically disturbed.

We analyze this in the framework of MHD tests in chapter 2. But cosmological simulations are not so easy to describe. The shocks and conditions that the implementation has to solve are countless, therefore we study statistically how this errors evolve.

In the left panel of Fig. (D.1) we can show the evolution of the $\nabla \cdot \mathbf{B}$ errors and magnetic energy in redshift. We plot the averaged quantities in the whole simulation in physical units. At early times, we observe how the magnetic field is diluted by the cosmological expansion of the universe until $z \sim 10$, when the structure formation process start to take place and the dilution is canceled and reverted. Additionally, we observe some merger events as bursts in the mean magnetic energy. At early times, the $\nabla \cdot \mathbf{B}$ errors are small, as the simulation evolves they grow following the disorder proper from the hydrodynamical motions. At redshift $z \sim 10$ we the structure formation process starts and now the magnetic field begin to try to drive the errors. At redshift $z < 4$ the errors arise to values $> 1E-2$ that epoch corresponds to the most agitated in the Universe history where the due to rapid structure formation and halo collapses. In those processes, that will continue during the rest of the simulation, the there are shocks from the accretion of matter in halos and there is a difference on the shape the magnetic profile and density. However, both magnetic field and $\nabla \cdot \mathbf{B}$ errors, reach a saturation level at $z < 0.5$ due to the equipartition between magnetic and turbulent energy.

This evolution dependence of the $\nabla \cdot \mathbf{B}$ errors can be originated from the difference in how hydrodynamical and magnetic forces scale with distance. As an example in in the right panel of Fig. (D.1), we show the final ($z = 0$) density profile of our cluster, superposing the magnetic field. One can observe a steeper slope for the magnetic field, mostly around ~ 0.8Mpc. In general this is not a problem per se, SPH should be able to deal with it. However, be observe certain situations where the induction equation can derive a wrong magnetic field, usually high.It will not affect overall evolution of the system because of the low numerical mixing of SPH, and unless it is corrected or advected to the high magnetic field regions, it will remain with high $\nabla \cdot \mathbf{B}$ with a slow decay until the end of the simulation.

In the first panel of Fig. (D.2) we show the distribution of the magnetic (black), kinetic (blue) and thermal (green) energy densities. We can see how in general the thermal and

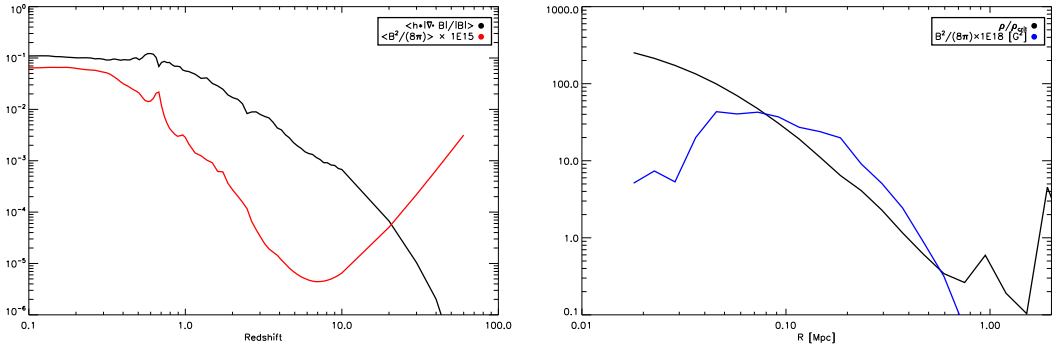

Figure D.1: In the left panel we shown the evolution of the mean numerical $\nabla \cdot \mathbf{B}$ errors (black) and magnetic field energy (red) in the whole cosmological simulation. When first structures collapse ($z < 10$)the numerical errors arise. In the right panel we shown a comparison between density and magnetic profiles. The magnetic field is multiplied by a factor of 10^{-20} to show the shape change between them. One can observe that the magnetic field is steeper at $\sim$ 1Mpc.

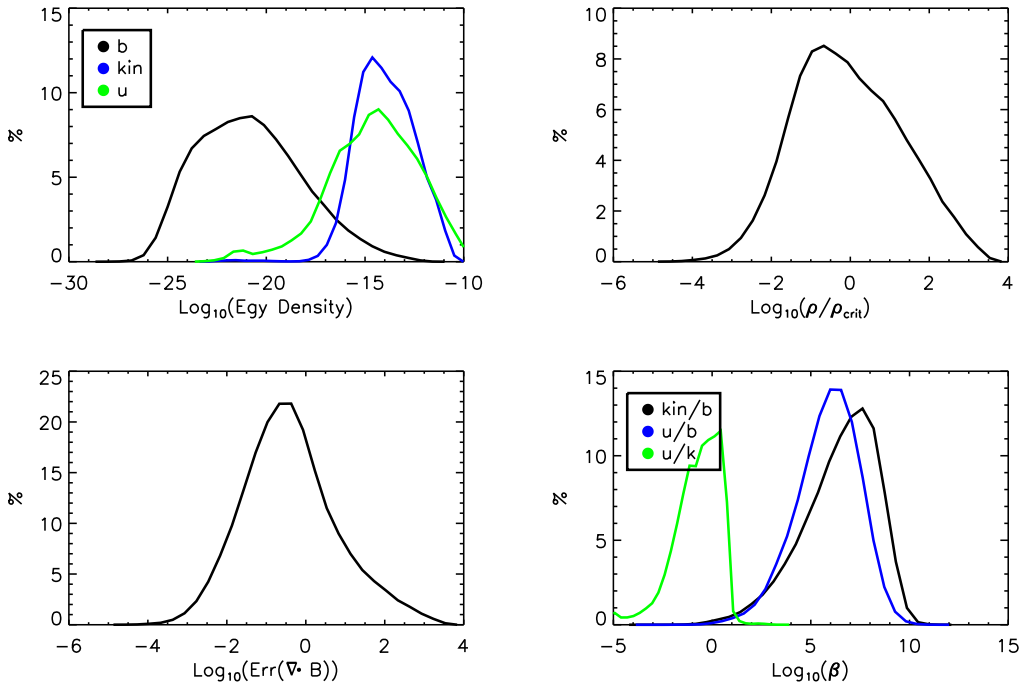

Figure D.2: In the first panel we show the distribution of the magnetic (black), kinetic (blue) and thermal (green) energy densities. We can see how in general the thermal and kinetic energy densities are several orders of magnitude higher. The upper right panel shows the density over density-critical ratio histogram seen the huge dynamical range that SPH allow us to cover, and magnetic fields are distributed in. In the bottom left corner we show the distribution of the $\nabla \cdot \mathbf{B}$ errors. The average and most of the particles have low than one error, arising the question where are those particles located. Finally we show a distribution of the different energy ratios β.

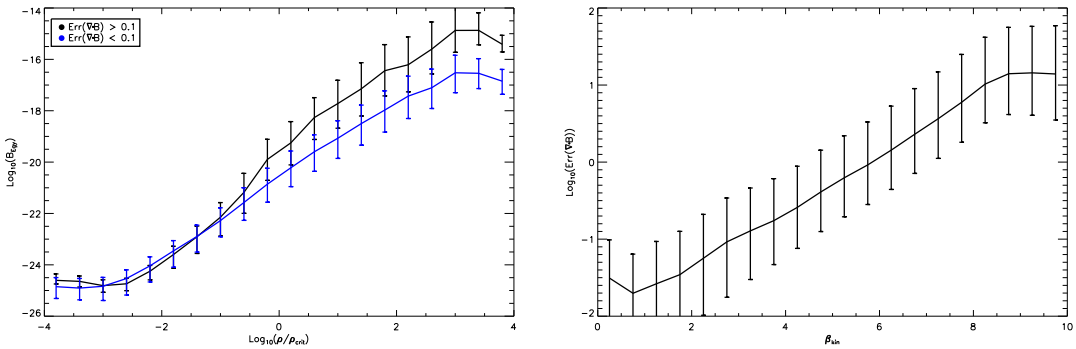

Figure D.3: In the left panel we show magnetic field as function of density for the particles slitted in samples of $\nabla \cdot \mathbf{B}$ higher and lower than 0.1. In general we see that the high $\nabla \cdot \mathbf{B}$ particles are the ones with less magnetic energy at a given density. Note that for ρ/ρ_{crit} arround 10^{-2} both samples have the same values. In the right panel we show $\nabla \cdot \mathbf{B}$ errors as function of the β_{kin}, showing a clear correlation to higher ratios.

kinetic energy densities are several orders of magnitude higher, however there is a energy region where all of them overlaps. In the bottom left corner we show the distribution of the $\nabla \cdot \mathbf{B}$ errors. The average and most of the particles have below unity. However, the slopes for higher or lower errors are different, arising the question where are those particles located. Finally we show a distribution of the different energy ratios β, in the bottom right panel of Fig. (D.2). We can see that in general either kinetic or thermal energy ratios are higher, and in terms of thermal-kinetic ratio, the kinetic energy densities are higher.

In general the $\nabla \cdot \mathbf{B}$ errors don't seem to correlate with other variables. However there is a slight tendency to correlate with the strength of the magnetic field (Bürzle et al., 2010; Kotarba et al., 2010a). To continue the analysis we separate the particles in two samples, in terms of high and low $\nabla \cdot \mathbf{B}$ error, we use $\nabla \cdot \mathbf{B} = 0.1$ as the threshold. In the left panel of Fig. (D.3) we shown how particles with high $\nabla \cdot \mathbf{B}$ errors use to have lower magnetic fields for a given density. This fact give us the hint that the final force that they suffer will be not magnetic dominated [1] compared with the low $\nabla \cdot \mathbf{B}$ case. Note that both samples have the same magnetic field average at densities of $\rho/\rho_{crit} \sim 10^{-2}$ which is the characteristic density at $r \sim 0.5 - 0.8$Mpc. Interestingly if we analyze the relation between these energies we saw again a correlation.

To confirm this, we study the $\nabla \cdot \mathbf{B}$ errors against their kinetic/thermal to magnetic energy density ratio (also called β in the literature) for the set including all the particles. These plot is shown in the right panel of Fig. (D.3), where a strong correlation is found. Historically, instabilities happened in the opposite case (Phillips and Monaghan, 1985) Meaning that the high beta are particles dominated by kinetic motions, therefore the magnetic field configuration is more difficult to be restored. Note that when we talk about low and high in the β samples is relative to the whole sample. Statistically most of the particles have high β (see Fig. (D.2)).

Finally we also plot in Fig. (D.4) the $\nabla \cdot \mathbf{B}$ errors in density bins for two β samples, larger and smaller than 10^7. Surprisingly we don't find any correlation of the effect with

[1] However, he magnetic energy are always a couple or orders of magnitude bellow the thermal and kinetic

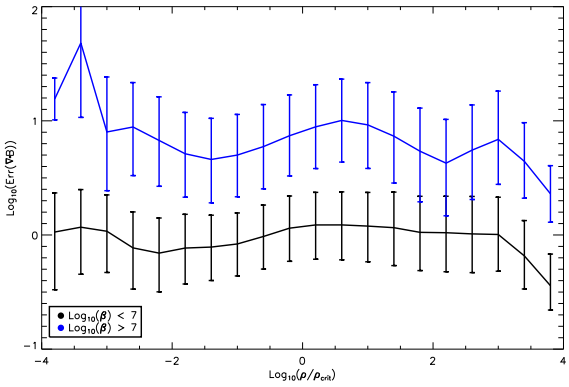

Figure D.4: $\nabla \cdot \mathbf{B}$ errors as function of density, separated in two samples of β_{kin} larger or smaller than 7. Clearly there is a correlation between the higher ratio and lower $\nabla \cdot \mathbf{B}$ errors, and surprisingly there is no trend with density, meaning that possibly this is a drawback from the scheme itself.

density. This means that the effect is not caused by strong hydrodynamic shocks in the center of halos, leading to the open question which kind of shocks generate this $\nabla \cdot \mathbf{B}$. On the other hand explains why the use of threshold in our schemes is so useful, the changes in the stress tensor given by $\nabla \cdot \mathbf{B}$ terms can be driven by completely hydrodynamical effects, not related with real numerical artifacts, therefore the correction is not needed.

Part VI

Acknowledgments

Acknowledgments

I want to thank, specially, my wife, **Michi**, because she join me in this journey to the unknown, called life. My family, for all the continuous support thought space and time. Klaus, to take a chance with me. Hanna, Julius and Florian to the support in the writing and reading, and to MHD considerations. Fer, Leo, Sebas, Ceci, Paula, Jesús, Eva, José, Tom and Damian (the most acknowledged boy of the world), and all the friends that I've done in Germany, for the supportive true friendship build thought the years. Dante, Nelson, Yami, for being myself in south America. The Peralta brothers, for the friendship and reading. My friends in Argentina (Facu, Mario, Negro, Dani, GuilleK, Leo, Jose) to build what I am. My office mates (Umberto, Mona, Qi, Andre) and people from the MPA for the warm welcomed. *Galileo-mobile* project, to teach us, that plenty of projects can be done, while working together.

Part VII

Bibliography

Bibliography

Adelman-McCarthy, J. K., Agüeros, M. A., Allam, S. S., Allende Prieto, C., Anderson, K. S. J., Anderson, S. F., Annis, J., Bahcall, N. A., Bailer-Jones, C. A. L., and Zucker, D. B. (2008). The Sixth Data Release of the Sloan Digital Sky Survey. *ApJS*, 175:297–313.

Agertz, O., Moore, B., Stadel, J., Potter, D., Miniati, F., Read, J., Mayer, L., Gawryszczak, A., Kravtsov, A., Nordlund, Å., Pearce, F., Quilis, V., Rudd, D., Springel, V., Stone, J., Tasker, E., Teyssier, R., Wadsley, J., and Walder, R. (2007). Fundamental differences between SPH and grid methods. *MNRAS*, 380:963–978.

Alfvén, H. (1949). On the Solar Origin of Cosmic Radiation. *Physical Review*, 75:1732–1735.

Athreya, R. M., Kapahi, V. K., McCarthy, P. J., and van Breugel, W. (1998). Large rotation measures in radio galaxies at Z greater than 2. *A&A*, 329:809–820.

Balsara, D. S. and Spicer, D. S. (1999). A Staggered Mesh Algorithm Using High Order Godunov Fluxes to Ensure Solenoidal Magnetic Fields in Magnetohydrodynamic Simulations. *Journal of Computational Physics*, 149:270–292.

Beck, R. (2009). Galactic and extragalactic magnetic fields - a concise review. *Astrophysics and Space Sciences Transactions*, 5:43–47.

Beck, R., Brandenburg, A., Moss, D., Shukurov, A., and Sokoloff, D. (1996). Galactic Magnetism: Recent Developments and Perspectives. *ARA&A*, 34:155–206.

Beck, R. and Gaensler, B. M. (2004). Observations of magnetic fields in the Milky Way and in nearby galaxies with a Square Kilometre Array. *New Astronomy Review*, 48:1289–1304.

Beck, R., Shoutenkov, V., Ehle, M., Harnett, J. I., Haynes, R. F., Shukurov, A., Sokoloff, D. D., and Thierbach, M. (2002). Magnetic fields in barred galaxies. I. The atlas. *A&A*, 391:83–102.

Blasi, P., Burles, S., and Olinto, A. V. (1999). Cosmological Magnetic Field Limits in an Inhomogeneous Universe. *ApJL*, 514:L79–L82.

Bonafede, A., Feretti, L., Murgia, M., Govoni, F., Giovannini, G., Dallacasa, D., Dolag, K., and Taylor, G. B. (2010). The Coma cluster magnetic field from Faraday rotation measures. *A&A*, 513:A30+.

Borgani, S. and Kravtsov, A. (2009). Cosmological simulations of galaxy clusters. *ArXiv e-prints*.

Børve, S., Omang, M., and Trulsen, J. (2001). Regularized Smoothed Particle Hydrodynamics: A New Approach to Simulating Magnetohydrodynamic Shocks. *ApJ*, 561:82–93.

Børve, S., Omang, M., and Trulsen, J. (2004). Two-dimensional MHD Smoothed Particle Hydrodynamics Stability Analysis. *ApJS*, 153:447–462.

Børve, S., Omang, M., and Trulsen, J. (2006). Multidimensional MHD Shock Tests of Regularized Smoothed Particle Hydrodynamics. *ApJ*, 652:1306–1317.

Brackbill, J. U. and Barnes, D. C. (1980). The effect of nonzero product of magnetic gradient and B on the numerical solution of the magnetohydrodynamic equations. *Journal of Computational Physics*, 35:426–430.

Brandenburg, A. (2010). Magnetic field evolution in simulations with Euler potentials. *MNRAS*, 401:347–354.

Brandenburg, A., Candelaresi, S., and Chatterjee, P. (2009). Small-scale magnetic helicity losses from a mean-field dynamo. *MNRAS*, 398:1414–1422.

Brio, M. and Wu, C. C. (1988). An upwind differencing scheme for the equations of ideal magnetohydrodynamics. *Journal of Computational Physics*, 75:400–422.

Brüggen, M. and Hoeft, M. (2006). Simulations of magnetic fields in the cosmos. *Astronomische Nachrichten*, 327:587–+.

Brüggen, M., Ruszkowski, M., Simionescu, A., Hoeft, M., and Dalla Vecchia, C. (2005). Simulations of Magnetic Fields in Filaments. *ApJL*, 631:L21–L24.

Brunetti, G. and Lazarian, A. (2007). Compressible turbulence in galaxy clusters: physics and stochastic particle re-acceleration. *MNRAS*, 378:245–275.

Brunetti, G., Setti, G., Feretti, L., and Giovannini, G. (2001). Particle reacceleration in the Coma cluster: radio properties and hard X-ray emission. *MNRAS*, 320:365–378.

Burbidge, G. R. (1959). Estimates of the Total Energy in Particles and Magnetic Field in the Non-Thermal Radio Sources. *ApJ*, 129:849–+.

Bürzle, F., Clark, P. C., Stasyszyn, F., Greif, T., Dolag, K., Klessen, R. S., and Nielaba, P. (2010). Protostellar collapse and fragmentation using an MHD GADGET. *ArXiv e-prints*.

Carilli, C. L. and Taylor, G. B. (2002). Cluster Magnetic Fields. *ARA&A*, 40:319–348.

Cavaliere, A. and Fusco-Femiano, R. (1976). X-rays from hot plasma in clusters of galaxies. *A&A*, 49:137–144.

Dai, W. and Woodward, P. R. (1994). Extension of the Piecewise Parabolic Method to Multidimensional Ideal Magnetohydrodynamics. *Journal of Computational Physics*, 115:485–514.

Davis, Jr., L. and Greenstein, J. L. (1951). The Polarization of Starlight by Aligned Dust Grains. *ApJ*, 114:206–+.

Dedner, A., Kemm, F., Kröner, D., Munz, C.-D., Schnitzer, T., and Wesenberg, M. (2002). Hyperbolic Divergence Cleaning for the MHD Equations. *Journal of Computational Physics*, 175:645–673.

Dolag, K., Bartelmann, M., and Lesch, H. (1999). SPH simulations of magnetic fields in galaxy clusters. *A&A*, 348:351–363.

Dolag, K., Bartelmann, M., and Lesch, H. (2002). Evolution and structure of magnetic fields in simulated galaxy clusters. *A&A*, 387:383–395.

Dolag, K., Evrard, A., and Bartelmann, M. (2001a). The temperature-mass relation in magnetized galaxy clusters. *A&A*, 369:36–41.

Dolag, K., Grasso, D., Springel, V., and Tkachev, I. (2004a). Mapping Deflections of Ultrahigh Energy Cosmic Rays in Constrained Simulations of Extraglactic Magnetic Fields. *Soviet Journal of Experimental and Theoretical Physics Letters*, 79:583–587.

Dolag, K., Grasso, D., Springel, V., and Tkachev, I. (2005a). Constrained simulations of the magnetic field in the local Universe and the propagation of ultrahigh energy cosmic rays. *Journal of Cosmology and Astro-Particle Physics*, 1:9–+.

Dolag, K., Hansen, F. K., Roncarelli, M., and Moscardini, L. (2005b). The imprints of local superclusters on the Sunyaev-Zel'dovich signals and their detectability with Planck. *MNRAS*, 363:29–39.

Dolag, K., Jubelgas, M., Springel, V., Borgani, S., and Rasia, E. (2004b). Thermal Conduction in Simulated Galaxy Clusters. *ApJL*, 606:L97–L100.

Dolag, K., Kachelriess, M., Ostapchenko, S., and Tomas, R. (2010). Lower limit on the strength and filling factor of extragalactic magnetic fields. *ArXiv e-prints*.

Dolag, K. and Schindler, S. (2000). The effect of magnetic fields on the mass determination of clusters of galaxies. *A&A*, 364:491–496.

Dolag, K., Schindler, S., Govoni, F., and Feretti, L. (2001b). Correlation of the magnetic field and the intra-cluster gas density in galaxy clusters. *A&A*, 378:777–786.

Dolag, K. and Stasyszyn, F. (2009). An MHD GADGET for cosmological simulations. *MNRAS*, 398:1678–1697.

Donnert, J., Dolag, K., Brunetti, G., Cassano, R., and Bonafede, A. (2010). Radio haloes from simulations and hadronic models - I. The Coma cluster. *MNRAS*, 401:47–54.

Donnert, J., Dolag, K., and et al (2011). In prep. *ArXiv e-prints*.

Donnert, J., Dolag, K., Lesch, H., and Müller, E. (2009). Cluster magnetic fields from galactic outflows. *MNRAS*, 392:1008–1021.

Dreher, J. W., Carilli, C. L., and Perley, R. A. (1987). The Faraday rotation of Cygnus A - Magnetic fields in cluster gas. *ApJ*, 316:611–625.

Dubois, Y. and Teyssier, R. (2008). Cosmological MHD simulation of a cooling flow cluster. *A&A*, 482:L13–L16.

Eilek, J., Owen, F., and Marković, T. (2006). Radio haloes in galaxy clusters: what do they tell us about the cluster's magnetic field? *Astronomische Nachrichten*, 327:567–568.

Eilek, J. A. and Owen, F. N. (2002). Magnetic Fields in Cluster Cores: Faraday Rotation in A400 and A2634. *ApJ*, 567:202–220.

Elstner, D., Otmianowska-Mazur, K., von Linden, S., and Urbanik, M. (2000). Galactic magnetic fields and spiral arms. 3D dynamo simulations. *A&A*, 357:129–138.

Ensslin, T. A., Biermann, P. L., Klein, U., and Kohle, S. (1998). Cluster radio relics as a tracer of shock waves of the large-scale structure formation. *A&A*, 332:395–409.

Enßlin, T. A. and Gopal-Krishna (2001). Reviving fossil radio plasma in clusters of galaxies by adiabatic compression in environmental shock waves. *A&A*, 366:26–34.

Enßlin, T. A., Pfrommer, C., Springel, V., and Jubelgas, M. (2007). Cosmic ray physics in calculations of cosmological structure formation. *A&A*, 473:41–57.

Fabian, A. C. (1994). Cooling Flows in Clusters of Galaxies. *ARA&A*, 32:277–318.

Fabian, A. C., Nulsen, P. E. J., and Canizares, C. R. (1984). Cooling flows in clusters of galaxies. *Nature*, 310:733–740.

Feretti, L., Dallacasa, D., Giovannini, G., and Tagliani, A. (1995). The magnetic field in the Coma cluster. *A&A*, 302:680–+.

Feretti, L., Dallacasa, D., Govoni, F., Giovannini, G., Taylor, G. B., and Klein, U. (1999a). The radio galaxies and the magnetic field in Abell 119. *A&A*, 344:472–482.

Feretti, L., Perley, R., Giovannini, G., and Andernach, H. (1999b). VLA observations of the giant radio galaxy 3C 449. *A&A*, 341:29–43.

Gingold, R. A. and Monaghan, J. J. (1977). Smoothed particle hydrodynamics - Theory and application to non-spherical stars. *MNRAS*, 181:375–389.

Ginzburg, V. L. and Syrovatskii, S. I. (1969). Developments in the Theory of Synchrotron Radiation and its Reabsorption. *ARA&A*, 7:375–+.

Giovannini, G. and Feretti, L. (2000). Halo and relic sources in clusters of galaxies. *New A.*, 5:335–347.

Giovannini, G., Feretti, L., Venturi, T., Kim, K., and Kronberg, P. P. (1993). The halo radio source Coma C and the origin of halo sources. *ApJ*, 406:399–406.

Gonzalez, A. H., Zaritsky, D., and Zabludoff, A. I. (2007). A Census of Baryons in Galaxy Clusters and Groups. *ApJ*, 666:147–155.

Górski, K. M., Hivon, E., Banday, A. J., Wandelt, B. D., Hansen, F. K., Reinecke, M., and Bartelmann, M. (2005). HEALPix: A Framework for High-Resolution Discretization and Fast Analysis of Data Distributed on the Sphere. *ApJ*, 622:759–771.

Govoni, F. (2006). Observations of magnetic fields in regular and irregular clusters. *Astronomische Nachrichten*, 327:539–+.

Govoni, F., Enßlin, T. A., Feretti, L., and Giovannini, G. (2001). A comparison of radio and X-ray morphologies of four clusters of galaxies containing radio halos. *A&A*, 369:441–449.

Govoni, F. and Feretti, L. (2004). Magnetic Fields in Clusters of Galaxies. *International Journal of Modern Physics D*, 13:1549–1594.

Hale, G. E. (1908). On the Probable Existence of a Magnetic Field in Sun-Spots. *ApJ*, 28:315–+.

Han, J. L., Ferriere, K., and Manchester, R. N. (2004). The Spatial Energy Spectrum of Magnetic Fields in Our Galaxy. *ApJ*, 610:820–826.

Han, J. L., Manchester, R. N., Lyne, A. G., Qiao, G. J., and van Straten, W. (2006). Pulsar Rotation Measures and the Large-Scale Structure of the Galactic Magnetic Field. *ApJ*, 642:868–881.

Hardcastle, M. J., Worrall, D. M., and Birkinshaw, M. (1998). Dynamics of the radio galaxy 3C449. *MNRAS*, 296:1098–1104.

Hiltner, W. A. (1949). Polarization of Radiation from Distant Stars by the Interstellar Medium. *Nature*, 163:283–+.

Hoffman, Y. and Ribak, E. (1991). Constrained realizations of Gaussian fields - A simple algorithm. *ApJL*, 380:L5–L8.

Jackson, J. D. (1975). *Classical electrodynamics*.

Jansson, R., Farrar, G. R., Waelkens, A. H., and et al. (2008). Large scale magnetic field of the Milky Way from WMAP3 data. In *International Cosmic Ray Conference*, volume 2 of *International Cosmic Ray Conference*, pages 223–226.

Jubelgas, M., Springel, V., and Dolag, K. (2004). Thermal conduction in cosmological SPH simulations. *MNRAS*, 351:423–435.

Kaiser, N. (1986). Evolution and clustering of rich clusters. *MNRAS*, 222:323–345.

Katz, N. and White, S. D. M. (1993a). Hierarchical galaxy formation - Overmerging and the formation of an X-ray cluster. *ApJ*, 412:455–478.

Katz, N. and White, S. D. M. (1993b). Hierarchical galaxy formation - Overmerging and the formation of an X-ray cluster. *ApJ*, 412:455–478.

Kolatt, T. (1998). Determination of the Primordial Magnetic Field Power Spectrum by Faraday Rotation Correlations. *ApJ*, 495:564–+.

Komatsu, E., Dunkley, J., Nolta, M. R., Bennett, C. L., Gold, B., Hinshaw, G., Jarosik, N., Larson, D., Limon, M., Page, L., Spergel, D. N., Halpern, M., Hill, R. S., Kogut, A., Meyer, S. S., Tucker, G. S., Weiland, J. L., Wollack, E., and Wright, E. L. (2009). Five-Year Wilkinson Microwave Anisotropy Probe Observations: Cosmological Interpretation. *ApJS*, 180:330–376.

Kotarba, H., Karl, S. J., Naab, T., Johansson, P. H., Dolag, K., Lesch, H., and Stasyszyn, F. A. (2010a). Simulating Magnetic Fields in the Antennae Galaxies. *ApJ*, 716:1438–1452.

Kotarba, H., Lesch, H., Dolag, K., Naab, T., Johansson, P. H., Donnert, J., and Stasyszyn, F. A. (2010b). Galactic ménage a trois: Simulating magnetic fields in colliding galaxies. *ArXiv e-prints*.

Kotarba, H., Lesch, H., Dolag, K., Naab, T., Johansson, P. H., and Stasyszyn, F. A. (2009). Magnetic field structure due to the global velocity field in spiral galaxies. *MNRAS*, 397:733–747.

Kraichnan, R. H. (1965). Inertial-Range Spectrum of Hydromagnetic Turbulence. *Physics of Fluids*, 8:1385–1387.

Kravtsov, A. V., Klypin, A., and Hoffman, Y. (2002). Constrained Simulations of the Real Universe. II. Observational Signatures of Intergalactic Gas in the Local Supercluster Region. *ApJ*, 571:563–575.

Kronberg, P. P. (1994). Extragalactic magnetic fields. *Reports on Progress in Physics*, 57:325–382.

Kronberg, P. P. (1996). Intergalactic Magnetic Fields, and Some Connections with Cosmic Rays. *S.S.R.*, 75:387–399.

Kronberg, P. P. and Perry, J. J. (1982). Absorption lines, Faraday rotation, and magnetic field estimates for QSO absorption-line clouds. *ApJ*, 263:518–532.

Kronberg, P. P. and Simard-Normandin, M. (1976). New evidence on the origin of rotation measures in extragalactic radio sources. *Nature*, 263:653–656.

Kulsrud, R. M., Cen, R., Ostriker, J. P., and Ryu, D. (1997). The Protogalactic Origin for Cosmic Magnetic Fields. *ApJ*, 480:481–+.

Large, M. I., Mathewson, D. S., and Haslam, C. G. T. (1959). A High-Resolution Survey of the Coma Cluster of Galaxies at 408 Mc./s. *Nature*, 183:1663–1664.

Lee, J., Pen, U., Taylor, A. R., Stil, J. M., and Sunstrum, C. (2009). Detection of Large-Scale Cosmic Magnetic Fields. *arXiv:0906.1631*.

Li, H., Xu, H., and Liu, W. (2008a). Magnetic Fields and Turbulence in the Intra-cluster Medium of Galaxy Clusters. *APS Meeting Abstracts*, pages 6021P–+.

Li, S., Li, H., and Cen, R. (2008b). CosmoMHD: A Cosmological Magnetohydrodynamics Code. *ApJS*, 174:1–12.

Loken, C., Norman, M. L., Nelson, E., Burns, J., Bryan, G. L., and Motl, P. (2002). A Universal Temperature Profile for Galaxy Clusters. *ApJ*, 579:571–576.

Londrillo, P. and Del Zanna, L. (2000). High-Order Upwind Schemes for Multidimensional Magnetohydrodynamics. *ApJ*, 530:508–524.

Lucy, L. B. (1977). A numerical approach to the testing of the fission hypothesis. *AJ*, 82:1013–1024.

Markevitch, M., Gonzalez, A. H., David, L., Vikhlinin, A., Murray, S., Forman, W., Jones, C., and Tucker, W. (2002). A Textbook Example of a Bow Shock in the Merging Galaxy Cluster 1E 0657-56. *ApJ*, 567:L27–L31.

Mason, J., Cattaneo, F., and Boldyrev, S. (2008). Numerical measurements of the spectrum in magnetohydrodynamic turbulence. *Physics Reviews*, 77(3):036403–+.

Mathis, H., Lemson, G., Springel, V., Kauffmann, G., White, S. D. M., Eldar, A., and Dekel, A. (2002). Simulating the formation of the local galaxy population. *MNRAS*, 333:739–762.

Miley, G. (1980). The structure of extended extragalactic radio sources. *ARA&A*, 18:165–218.

Moffatt, H. K. (1978). *Magnetic field generation in electrically conducting fluids*.

Monaghan, J. J. (1992). Smoothed particle hydrodynamics. *ARA&A*, 30:543–574.

Monaghan, J. J. (1997). SPH and Riemann Solvers. *Journal of Computational Physics*, 136:298–307.

Monaghan, J. J. (2005). Smoothed particle hydrodynamics. *Reports on Progress in Physics*, 68(8):1703.

Monaghan, J. J. and Lattanzio, J. C. (1985). A refined particle method for astrophysical problems. *A&A*, 149:135–143.

Morris, J. P. and Monaghan, J. J. (1997). A Switch to Reduce SPH Viscosity. *Journal of Computational Physics*, 136:41–50.

Moss, D. and Shukurov, A. (1996). Turbulence and magnetic fields in elliptical galaxies. *MNRAS*, 279:229–239.

Nagai, D., Kravtsov, A. V., and Vikhlinin, A. (2007). Effects of Galaxy Formation on Thermodynamics of the Intracluster Medium. *ApJ*, 668:1–14.

Navarro, J. F., Frenk, C. S., and White, S. D. M. (1995). Simulations of X-ray clusters. *MNRAS*, 275:720–740.

Nuza, S. E., Dolag, K., and Saro, A. (2010). Photometric and clustering properties of hydrodynamical galaxies in a cosmological volume: results at z = 0. *MNRAS*, 407:1376–1386.

Omang, M., Børve, S., and Trulsen, J. (2006). SPH in spherical and cylindrical coordinates. *Journal of Computational Physics*, 213:391–412.

Orszag, S. A. and Tang, C. (1979). Small-scale structure of two-dimensional magnetohydrodynamic turbulence. *Journal of Fluid Mechanics*, 90:129–143.

Page, L., Hinshaw, G., Komatsu, E., Nolta, M. R., Spergel, D. N., Bennett, C. L., Barnes, C., Bean, R., Doré, O., Dunkley, J., Halpern, M., Hill, R. S., and et al. (2007). Three-Year Wilkinson Microwave Anisotropy Probe (WMAP) Observations: Polarization Analysis. *ApJS*, 170:335–376.

Parker, E. N. (1979). *Cosmical magnetic fields: Their origin and their activity*.

Parker, E. N. (2007). *Conversations on Electric and Magnetic Fields in the Cosmos*. Princeton University Press.

Pedrosa, S., Tissera, P. B., and Scannapieco, C. (2010). The joint evolution of baryons and dark matter haloes. *MNRAS*, 402:776–788.

Peebles, P. J. E. (1980). *The large-scale structure of the universe*. Research supported by the National Science Foundation. Princeton, N.J., Princeton University Press, 1980. 435 p.

Peterson, J. R. and Fabian, A. C. (2006). X-ray spectroscopy of cooling clusters. *Phys. Rep.*, 427:1–39.

Pfrommer, C., Enßlin, T. A., Springel, V., Jubelgas, M., and Dolag, K. (2007). Simulating cosmic rays in clusters of galaxies - I. Effects on the Sunyaev-Zel'dovich effect and the X-ray emission. *MNRAS*, 378:385–408.

Phillips, G. J. and Monaghan, J. J. (1985). A numerical method for three-dimensional simulations of collapsing, isothermal, magnetic gas clouds. *MNRAS*, 216:883–895.

Picone, J. M. and Dahlburg, R. B. (1991). Evolution of the Orszag-Tang vortex system in a compressible medium. II - Supersonic flow. *Physics of Fluids B*, 3:29–44.

Price, D. J. and Monaghan, J. J. (2004a). Smoothed Particle Magnetohydrodynamics - I. Algorithm and tests in one dimension. *MNRAS*, 348:123–138.

Price, D. J. and Monaghan, J. J. (2004b). Smoothed Particle Magnetohydrodynamics - II. Variational principles and variable smoothing-length terms. *MNRAS*, 348:139–152.

Price, D. J. and Monaghan, J. J. (2005). Smoothed Particle Magnetohydrodynamics - III. Multidimensional tests and the ∇.B= 0 constraint. *MNRAS*, 364:384–406.

Quinn, T., Katz, N., Stadel, J., and Lake, G. (1997). Time stepping N-body simulations. *ArXiv Astrophysics e-prints*.

Rebusco, P., Churazov, E., Böhringer, H., and Forman, W. (2005). Impact of stochastic gas motions on galaxy cluster abundance profiles. *MNRAS*, 359:1041–1048.

Rees, M. J. and Reinhardt, M. (1972). Some Remarks on Intergalactic Magnetic Fields. *A&A*, 19:189–+.

Reid, M. J. and Silverstein, E. M. (1990). OH masers and the Galactic magnetic field. *ApJ*, 361:483–486.

Robishaw, T., Quataert, E., and Heiles, C. (2008). Extragalactic Zeeman Detections in OH Megamasers. *ApJ*, 680:981–998.

Rordorf, C., Grasso, D., and Dolag, K. (2004). Diffusion of ultra-high energy protons in galaxy clusters and secondary X- and gamma-ray emissions. *Astroparticle Physics*, 22:167–181.

Rosswog, S. and Price, D. (2007). MAGMA: a three-dimensional, Lagrangian magnetohydrodynamics code for merger applications. *MNRAS*, 379:915–931.

Ruzmaikin, A. A. and Sokolov, D. D. and Shukurov A.M., editor (1988). *Magnetic fields of galaxies*, volume 133 of *Astrophysics and Space Science Library*.

Ryu, D. and Jones, T. W. (1995). Numerical magetohydrodynamics in astrophysics: Algorithm and tests for one-dimensional flow'. *ApJ*, 442:228–258.

Ryu, D., Kang, H., and Biermann, P. L. (1998). Cosmic magnetic fields in large scale filaments and sheets. *A&A*, 335:19–25.

Ryu, D., Kang, H., Cho, J., and Das, S. (2008). Turbulence and Magnetic Fields in the Large-Scale Structure of the Universe. *Science*, 320:909–.

Sarazin, C. L. (1986). A simple cooling flow model for X-ray coronae around elliptical galaxies. *Gaseous halos of galaxies : proceedings of a workshop held at the National Radio Astronomy Observatory, Green Bank, West Virginia on May 30, 31 and June 1, 1985 / edited by Joel N. Bregman and Felix J. Lockman. NRAO Workshop, No. 12, p. 223 - 230*, 12:223–230.

Sarazin, C. L. (1988). *X-ray emission from clusters of galaxies*.

Sigl, G., Miniati, F., and Enssßlin, T. A. (2004). Ultrahigh energy cosmic ray probes of large scale structure and magnetic fields. *Phys. Rev. D*, 70(4):043007.

Sijacki, D. and Springel, V. (2006). Physical viscosity in smoothed particle hydrodynamics simulations of galaxy clusters. *MNRAS*, 371:1025–1046.

Spergel, D. N., Bean, R., Doré, O., Nolta, M. R., Bennett, C. L., Dunkley, J., Hinshaw, G., Jarosik, N., Komatsu, E., Page, L., Peiris, H. V., Verde, L., and et al. (2007). Three-Year Wilkinson Microwave Anisotropy Probe (WMAP) Observations: Implications for Cosmology. *ApJS*, 170:377–408.

Springel, V. (2005). The cosmological simulation code GADGET-2. *MNRAS*, 364:1105–1134.

Springel, V. (2010). E pur si muove: Galilean-invariant cosmological hydrodynamical simulations on a moving mesh. *MNRAS*, 401:791–851.

Springel, V. and Hernquist, L. (2002). Cosmological smoothed particle hydrodynamics simulations: the entropy equation. *MNRAS*, 333:649–664.

Springel, V. and Hernquist, L. (2003). Cosmological smoothed particle hydrodynamics simulations: a hybrid multiphase model for star formation. *MNRAS*, 339:289–311.

Springel, V., White, M., and Hernquist, L. (2001). Hydrodynamic Simulations of the Sunyaev-Zeldovich Effect(s). *ApJ*, 549:681–687.

Stasyszyn, F., Dolag, K., and et al (2011). In prep. *ArXiv e-prints*.

Stasyszyn, F., Nuza, S. E., Dolag, K., Beck, R., and Donnert, J. (2010). Measuring cosmic magnetic fields by rotation measure-galaxy cross-correlations in cosmological simulations. *MNRAS*, 408:684–694.

Stone, J. M., Gardiner, T. A., Teuben, P., Hawley, J. F., and Simon, J. B. (2008). Athena: A New Code for Astrophysical MHD. *ArXiv e-prints*, 804.

Subramanian, K., Shukurov, A., and Haugen, N. E. L. (2006). Evolving turbulence and magnetic fields in galaxy clusters. *MNRAS*, 366:1437–1454.

Sun, X. H. and Reich, W. (2009). Simulated square kilometre array maps from Galactic 3D-emission models. *A&A*, 507:1087–1105.

Sun, X. H., Reich, W., Waelkens, A., and Enßlin, T. A. (2008). Radio observational constraints on Galactic 3D-emission models. *A&A*, 477:573–592.

Taylor, A. R., Stil, J. M., and Sunstrum, C. (2009). A Rotation Measure Image of the Sky. *ApJ*, 702:1230–1236.

Taylor, G. B., Barton, E. J., and Ge, J. (1994). Searching for cluster magnetic fields in the cooling flows of 0745-191, A2029, and A4059. *AJ*, 107:1942–1952.

Taylor, G. B., Fabian, A. C., and Allen, S. W. (2002). Magnetic fields in the Centaurus cluster. *MNRAS*, 334:769–776.

Teyssier, R. (2002). Cosmological hydrodynamics with adaptive mesh refinement. A new high resolution code called RAMSES. *A&A*, 385:337–364.

Tormen, G., Bouchet, F. R., and White, S. D. M. (1997). The structure and dynamical evolution of dark matter haloes. *MNRAS*, 286:865–884.

Tornatore, L., Borgani, S., Dolag, K., and Matteucci, F. (2007). Chemical enrichment of galaxy clusters from hydrodynamical simulations. *MNRAS*, 382:1050–1072.

Tornatore, L., Borgani, S., Matteucci, F., Recchi, S., and Tozzi, P. (2004). Simulating the metal enrichment of the intracluster medium. *MNRAS*, 349:L19–L24.

Toth, G. (2000). The $\nabla \cdot B = 0$ Constraint in Shock-Capturing Magnetohydrodynamics Codes. *Journal of Computational Physics*, 161:605–652.

Waelkens, A., Jaffe, T., Reinecke, M., Kitaura, F. S., and Enßlin, T. A. (2009). Simulating polarized Galactic synchrotron emission at all frequencies. The Hammurabi code. *A&A*, 495:697–706.

White, S. D. M. (1976). The dynamics of rich clusters of galaxies. *MNRAS*, 177:717–733.

White, S. D. M. (1996). Formation and Evolution of Galaxies. In Schaeffer, R., Silk, J., Spiro, M., and Zinn-Justin, J., editors, *Cosmology and Large Scale Structure*, pages 349–+.

Widrow, L. M. (2002). Origin of galactic and extragalactic magnetic fields. *Reviews of Modern Physics*, 74:775–823.

Willson, M. A. G. (1970). Radio observations of the cluster of galaxies in Coma Berenices - the 5C4 survey. *MNRAS*, 151:1–44.

Wolfe, A. M., Jorgenson, R. A., Robishaw, T., Heiles, C., and Prochaska, J. X. (2008). An 84-μG magnetic field in a galaxy at redshift z = 0.692. *Nature*, 455:638–640.

Xu, H., Li, H., Collins, D. C., Li, S., and Norman, M. L. (2009). Turbulence and Dynamo in Galaxy Cluster Medium: Implications on the Origin of Cluster Magnetic Fields. *ApJL*, 698:L14–L17.

Zhuravleva, I. (2011). Gas Turbulent Motions in Galaxy Clusters. *ArXiv e-prints*.